ΕΘΝΙΚΟ ΜΕΤΣΟΒΙΟ
ΠΟΛΥΤΕΧΝΕΙΟ

ΣΧΟΛΗ ΕΦΑΡΜΟΣΜΕΝΩΝ
ΜΑΘΗΜΑΤΙΚΩΝ
ΚΑΙ ΦΥΣΙΚΩΝ ΕΠΙΣΤΗΜΩΝ

ΣΧΟΛΗ ΜΗΧΑΝΟΛΟΓΩΝ
ΜΗΧΑΝΙΚΩΝ

ΕΚΕΦΕ «ΔΗΜΟΚΡΙΤΟΣ»

ΙΝΣΤΙΤΟΥΤΟ ΝΑΝΟΕΠΙΣΤΗΜΗΣ
ΚΑΙ ΝΑΝΟΤΕΧΝΟΛΟΓΙΑΣ

ΙΝΣΤΙΤΟΥΤΟ ΠΥΡΗΝΙΚΗΣ ΚΑΙ
ΣΩΜΑΤΙΔΙΑΚΗΣ ΦΥΣΙΚΗΣ

Διατμηματικό Πρόγραμμα Μεταπτυχιακών Σπουδών

«Φυσική και Τεχνολογικές Εφαρμογές»

Μελέτη Δισδιάστατων Ανιχνευτών Micromegas

ΜΕΤΑΠΤΥΧΙΑΚΗ ΔΙΠΛΩΜΑΤΙΚΗ ΕΡΓΑΣΙΑ

του Μάριου Νάτσιου

Επιβλέπων: Θεόδωρος Αλεξόπουλος

Αθήνα, Ιούνιος, 2017

ΕΘΝΙΚΟ ΜΕΤΣΟΒΙΟ ΠΟΛΥΤΕΧΝΕΙΟ
ΣΧΟΛΗ ΕΦΑΡΜΟΣΜΕΝΩΝ ΜΑΘΗΜΑΤΙΚΩΝ ΚΑΙ ΦΥΣΙΚΩΝ ΕΦΑΡΜΟΓΩΝ
ΤΟΜΕΑΣ ΦΥΣΙΚΗΣ
ΕΡΓΑΣΤΗΡΙΟ ΠΕΙΡΑΜΑΤΙΚΗΣ ΦΥΣΙΚΗΣ ΥΨΗΛΩΝ ΕΝΕΡΓΕΙΩΝ

Μελέτη Δισδιάστατων Ανιχνευτών Micromegas

ΜΕΤΑΠΤΥΧΙΑΚΗ ΔΙΠΛΩΜΑΤΙΚΗ ΕΡΓΑΣΙΑ
Δ.Π.Μ.Σ Φυσική και Τεχνολογικές Εφαρμογές

του

Μάριου Νάτσιου

Επιβλέπων: Θεόδωρος Αλεξόπουλος
Καθηγητής Ε.Μ.Π

Εγκρίθηκε από την τριμελή εξεταστική επιτροπή την 20/6/2017

....	....	....
Θεόδωρος Αλεξόπουλος	Σταύρος Μαλτέζος	Ευάγγελος Γαζής
Καθηγητής Ε.Μ.Π	Αν. Καθηγητής Ε.Μ.Π	Καθηγητής Ε.Μ.Π

....

Μάριος Ε. Νάτσιος

NATIONAL TECHNICAL UNIVERSITY OF ATHENS
SCHOOL OF APPLIED MATHEMATICAL AND PHYSICAL SCIENCES
DEPARTMENT OF PHYSICS
HIGH ENERGY PHYSICS LABORATORY

Study of 2D Micromegas Detectors

A dissertation presented by

Marios E. Natsios

to

The Department of Physics
for the degree of
Master of Science
in the subject of

Physics

Advisor: Theodoros Alexopoulos
Professor, N.T.U.A

National Technical University of Athens
June 2017

....
Marios E. Natsios

Στους δικούς μου ανθρώπους...

Ευχαριστίες

Αρχικά θα ήθελα να ευχαριστήσω τον επιβλέποντα καθηγητή μου κ.Θεόδωρο Αλεξόπουλο για την πρόταση του θέματος και όσα μου έμαθε κατά την διάρκεια της εκπόνησης αυτής της εργασίας. Θα ήθελα επίσης να ευχαριστήσω τον Αν. Καθηγητή κ.Σταύρο Μαλτέζο για την στήριξη του και της διορθώσεις που μου πρότεινε όπως επίσης και τον Δρ. Κωνσταντίνο Ντέκα για την πολύτιμη βοήθεια που μου παρείχε. Ευχαριστώ επίσης τους συμφοιτητές και φίλους μου Ανδρέα Βγενόπουλο, Δημήτρη Τζανετάτο, Χρήστο Παρασκεύοπουλο και Παναγιώτη Ασσιούρα για την υποστήριξη τους και τις όμορφες στιγμές που είχαμε όλο αυτό το διάστημα. Ένα μεγάλο ευχαριστώ χρωστάω στην οικογένεια μου και στους στενούς μου φίλους καθώς χωρίς την ανιδιοτελή αγάπη και στήριξη τους η παρούσα διπλωματική εργασία δεν θα είχε πραγματοποιηθεί.

Περίληψη

Ο Μεγάλος Επιταχυντής Αδρονίων (LHC) θα υποστεί έναν αριθμό αναβαθμίσεων σε διάφορες φάσεις που θα οδηγήσουν σε μία τιμή φωτεινότητας της τάξεως των $\mathcal{L} = 7 \times 10^{34}$ $cm^{-2}s^{-1}$ μεγιστοποιώντας έτσι τις δυνατότητες επιστημονικής ανακάλυψης. Για τον ανιχνευτή ATLAS (A Toroid LHC ApparatuS), μια τέτοια αύξηση φωτεινότητας σημαίνει υψηλότερες ροές σωματιδίων. Για να διατηρήσει την τρέχουσα άριστη απόδοση του και να αντιμετωπίσει την αντίστοιχη αύξηση του ρυθμού σωματιδίων που αναμένεται, ο ανιχνευτής ATLAS θα αναβαθμιστεί. Η αναβάθμιση θα πραγματοποιηθεί σε δύο βήματα: την περίοδο Phase-1 στο κλείσιμο του LHC το 2019/2020 και στη Phase-2 το 2024-26.

Το μεγαλύτερο μέρος των αναβαθμίσεων του ATLAS στη Phase-1 επικεντρώνεται στην εσωτερική περιοχή των end-caps του φασματόμετρου μιονίων που ονομάζεται Small Wheel (SW). Η υψηλή ακτινοβολία υποβάθρου που αναμένεται μετά την αναβάθμιση στη περίοδο Phase-1 και κυρίως η αυξημένη φωτεινότητα στον αναβαθμισμένο HL-LHC μετά τη περίοδο του Phase-2 καθιστά απαραίτητη την αναβάθμιση του μιονικού συστήματος. Τα ανιχνευτικά συστήματα που απαρτίζουν τον SW (CSC,MDT,TGC) δεν θα είναι ικανά να διαχειριστούν τον αυξημένο ρυθμό σωματιδίων αποτελεσματικά καθώς η φωτεινότητα θα ξεπεράσει κατά πολύ την τιμή στην οποία έχουν σχεδιαστεί να λειτουργούν. Επίσης εξαιτίας σωματιδίων υποβάθρου χαμηλής ενέργειας, τα μιονικά trigger στη περιοχή των end-cap κυριαρχούνται από εσφαλμένα χτυπήματα ($> 90\%$). Για τους παραπάνω λόγους ο υπάρχον SW θα αντικατασταθεί με ένα νέο σύστημα (NSW) το οποίο θα αποτελείται από τις ανιχνευτικές τεχνολογίες των resistive-strip Micromegas (MM) και των small-strip Thin Gap Chambers (sTGC), όπου και οι δύο ανιχνευτές ανήκουν στη κατηγορία των ανιχνευτών αερίου.

Στη παρούσα διπλωματική εργασία μελετώνται οι resistive-strips Micromegas με δισδιάστατο σύστημα ανάγνωσης (MM τύπου Tmm) χρησιμοποιώντας δεδομένα από τη δοκιμαστική δέσμη Νοεμβρίου 2015 στο SPS/H6 στο CERN. Συγκεκριμένα εξετάζουμε κατά πόσο η πληροφορία του χρόνου του strip μπορεί να χρησιμοποιηθεί για την ακριβή ανακατασκευή της θέσης χτυπήματος στη περίπτωση κάθετων στο επίπεδο των ανιχνευτών τροχιών. Για τον λόγο αυτό αναπτύχθηκε μία μέθοδος προσαρμογής η οποία επιτρέπει τον προσδιορισμό της θέσης ελαχίστου χρόνου στους χρονικούς clusters των stips στο Υ επίπεδο ανάγνωσης, ενώ στη συνέχεια οι θέσεις αυτές χρησιμοποιούνται για την εκτίμηση της χωρικής ανάλυσης του ανιχνευτή. Το αποτέλεσμα αυτό συγκρίνεται με το αντίστοιχο που εξάγεται από τη μέθοδο του κέντρου βάρους για το ίδιο επίπεδο ανάγνωσης. Χρησιμοποιώντας τη προηγούμενη μέθοδο προσαρμογής, πραγματοποιούμε μία εκτίμηση της ταχύτητας διάδοσης σήματος στα resistive stips ενώ εξετάζουμε επίσης την ομοιομορφία αυτής της διάδοσης. Επιπλέον, αναπτύχθηκε ένας αλγόριθμος Monte Carlo για την περαιτέρω μελέτη των προηγούμενων αποτελεσμάτων. Στο τελευταίο μέρος αυτής της εργασίας παρουσιάζεται η ανάλυση δεδομένων από πειραματική διάταξη εγκατεστημένη στο Ε.Μ.Π που αποτελείται από ανιχνευτές MM με δισδιάστατο σύστημα ανάγνωσης, οι οποίοι πραγματοποίησαν μετρήσεις κοσμικής ακτινοβολίας.

Abstract

The Large Hadron Collider (LHC) will undergo a number of upgrades in several phases which will lead to a luminosity of the order of $\mathcal{L} = 7 \times 10^{34}\ cm^{-2}s^{-1}$, thus increasing its scientific discovery potential. For the ATLAS detector (A Toroidal LHC Apparatus), such a luminosity increase means higher particle rates. In order to maintain its current excellent performance and cope with the corresponding rate increase, the ATLAS detector will be upgraded. The upgrade will proceed in two steps: Phase-1 in the LHC shutdown 2019/2020 and Phase-2 in 2024-26.

The largest of the ATLAS Phase-1 upgrades focuses on the inner end-cap region of the muon spectrometer, named Small Wheel (SW). The high background radiation expected after the Phase-1 period and especially the increased luminosity after the Phase-2 period, makes the upgrade of the muon system necessary. The detection systems composing the SW (CSC,MDT,TGC) will not be able to handle the increased particle rate as the luminosity will far exceed the value at which they are designed to operate. Also due to low energy background particles, the end-cap muon triggers are dominated by fake hits ($> 90\%$). For the above reasons the current SW will be replaced by a new system which will comprise the detector technologies of resistive-strip Micromegas (MM) and small-strip Thin Gap Chambers (sTGC), with both detectors belonging to the category of gas detectors.

In this thesis we study the resistive-strips Micromegas detectors with two-dimensional readout system (Tmm-type MM) using data acquired from the test beam of November 2015 at H6/SPS, at CERN. More specifically, we examine whether the strip time information can be used for the precise reconstruction of hit position in the case of tracks perpendicular to the detector plane. For this purpose, a fitting method was developed which allows for the estimation of the minimum time position in a cluster of strips in the Y readout layer, and then we use these positions for the estimation of the detector's spatial resolution. This result is compared with that obtained using the charge centroid method for the same readout layer. By using the previous fitting method, we achieved an estimation of the signal propagation speed in the resistive strips, while we also examined the uniformity of this propagation. Furthermore, a Monte Carlo algorithm was developed for the further studying of the previous results. In the last part of this work, we present an analysis using data from the experimental setup installed in NTUA, which consists of Tmm-type MM chambers performing cosmic ray measurements.

Contents

List of Figures

List of Tables

Chapter 1

The Large Hadron Collider and the ATLAS Experiment

1.1 The Large Hadron Collider

The Large Hadron Collider (LHC) [8] which is located at CERN (European Organization for Nuclear Research), is the largest and most powerful particle accelerator in the world. It first started up on 10 September 2008 and remains the latest addition to CERN's accelerator complex. LHC is a two-ring superconducting hadron accelerator and collider installed in a 27 km long circular tunnel at a depth ranging from 50 to 175 meters running along the boarder between France and Switzerland, near the city of Geneva. The tunnel was originally constructed between 1984 and 1989 for the CERN LEP machine (Large Electron-Positron Collider) [9] which was in operation until the end of 2000.

Inside the accelerator, two high-energy particle beams travel across to the speed of light before they are made to collide. The beams travel in opposite directions in separate beam pipes, two tubes kept at ultrahigh vacuum. They are guided around the accelerator ring by a strong magnetic field maintained by superconducting electromagnets. The electromagnets are build from coils of special electric cable that operates in a superconducting state conducting electricity without resistance or loss of energy. This requires chilling the magnets to -271.3 °C , a temperature colder than the outer space. For this reason much of the accelerator is connected to a distribution system of liquid helium, which cools the magnets, as well as to other supply services.

The LHC is mainly operated with proton-proton beams and it has two high-luminosity general purpose experiments, ATLAS [10] and CMS [11], both with peak design luminosity of $\mathcal{L} = 10^{34} cm^{-2} s^{-1}$. It also has two low luminosity experiments, LHCb [12] for B-physics with peak design luminosity of $\mathcal{L} = 10^{32} cm^{-2} s^{-1}$ and TOTEM [13], for the detection of protons from elastic scattering at small angles, having a peak design luminosity of $\mathcal{L} = 2 \times 10^{29} cm^{-2} s^{-1}$. In addition to proton-proton beams , LHC is also operated with Pb-Pb ion beams and p-Pb beams. With ion beams LHC has a dedicated experiment called ALICE [14], with peak design luminosity of $\mathcal{L} = 10^{27} cm^{-2} s^{-1}$.

1.1.1 The Accelerator Complex

The acceleration complex at CERN is a succession of machines that accelerates particles at increasingly higher energies. Each machine boosts the energy of a beam of particles, before injecting the beam into the next machine in the sequence. In the LHC, the last element of this chain, particle beams are accelerated up to the energy of 6.5 TeV per beam. Most of the other accelerators in the chain have their own experimental halls where beams are used for experiments at lower energies. An overview of the accelerator complex at CERN is shown in Figure 1.1.

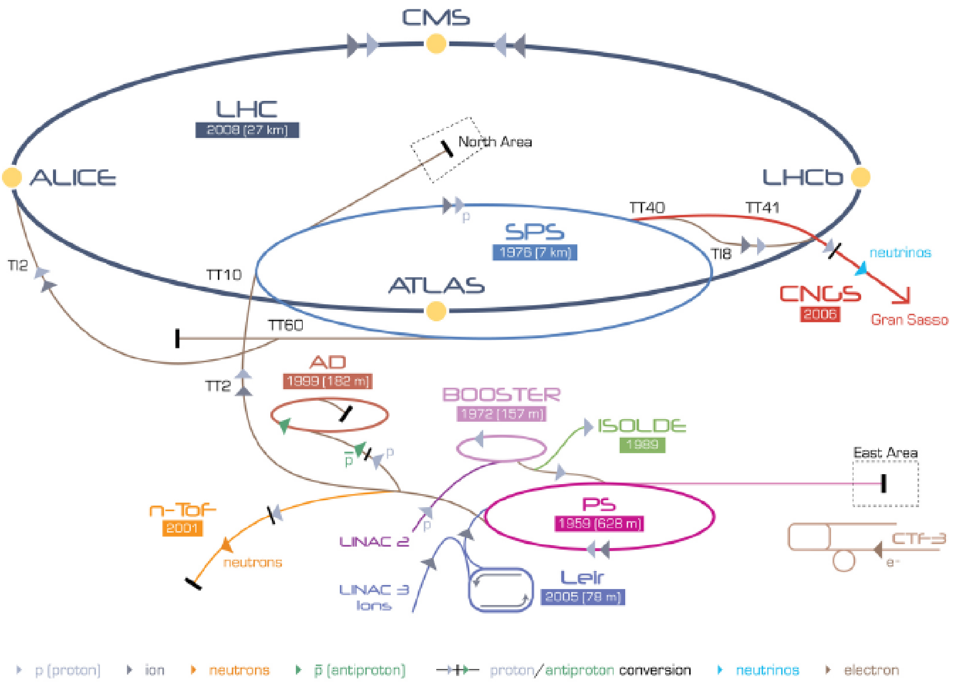

Figure 1.1: Schematic representation of the LHC accelerator complex.

The proton source is simply a bottle filled with compressed hydrogen gas. Hydrogen atoms from this gas cylinder are fed at a precisely controlled rate into the source chamber of a linear accelerator, CERN's LINAC 2 (LINear ACcelerator 2), the first accelerator in the chain, where there electrons are stripped off to leave hydrogen nuclei. These are positive charged protons, able to accelerate under the influence of an electric field. This initial acceleration performed by the LINAC 2 accelerates the protons at an energy of 50 GeV. The beam is then injected into the Proton Synchrotron Booster (PSB), which accelerates the protons to 1.4 GeV, followed by the Proton Synchrotron (PS), which pushes the beam to 25 GeV. Protons are then sent to the Super Proton Synchrotron (SPS) where they are accelerated to 450 GeV.

The protons are finally transferred to the two beam pipes of the LHC. The beam in one pipe circulates clockwise while the beam in the other circulates anticlockwise. It takes 4 minutes and 20 seconds to fill each LHC ring, and 20 minutes for the protons to reach their maximum energy of 6.5 TeV. Beams circulate for many hours inside the LHC beam pipes under normal operating conditions. The two beams are brought into collision inside the four above mentioned detectors, ALICE, ATLAS, CMS and LHCb, where the total energy at the collision point is equal to 13 TeV.

Thousands of magnets of different varieties and sizes are used to direct the beams around the accelerator. These include 1232 dipole magnets 15 meters in length which bend the beams, and 392 quadrupole magnets, each 5–7 meters long, which focus the beams. Just prior to collision, another type of magnet is used to "squeeze" the particles closer together to increase the chances of collisions. The main dipoles generate powerful 8.3 tesla magnetic fields at a current of around 11.7kA with the magnet having two apertures, one for each of the counter-rotating beams. This extremely high field is achieved by magnets made of superconducting Niobium-Titanium (NbTi) coils which are cooled at 1.9K by a closed liquid-helium circuit. The cryogenic equipment needed to produce the 100 tons of super-fluid helium is unprecedented in scale and complexity for the whole LHC. A drawing of of an LHC dipole magnet cross section is shown in Figure 1.2.

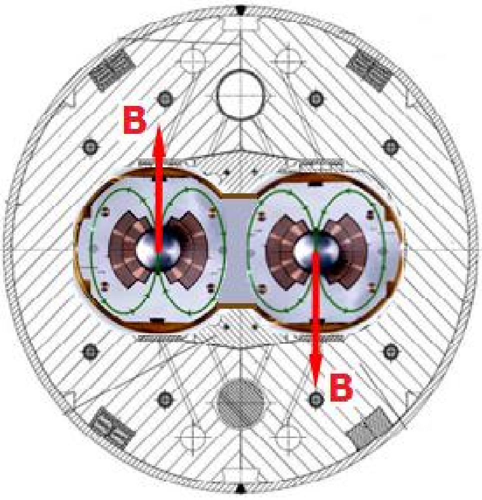

Figure 1.2: Graphical representation of an LHC dipole magnet cross section.

1.1.2 High Luminosity LHC (HL-LHC)

The Large Hadron Collider was successfully commissioned in 2010 for proton-proton collisions with a 7 TeV center-of-mass-energy. It delivered 8 TeV center-of-mass-energy proton collisions from April 2012 until the end of Run-1 in 2013. During Run-1 the LHC was able to deliver a total of 28.26 fb^{-1} of p-p collision data leading to a major physics program and remarkable physics results from the experiments. Following the first long shut down (LS1) in 2013-2014, in which the accelerator complex, as well as the experiments, underwent a series of upgrades and maintenance activities, it operated with 13 TeV center-of-mass proton collisions and a smaller bunch crossing (BC) of 25 ns (resulting a luminosity of about $\mathcal{L} \simeq 1.7 \times 10^{34} cm^{-2}s^{-1}$), during Run-2 from 2015 onwards.

To enhance its discovery potential, the LHC will need a major upgrade in the 2020s to extend its operability by another decade and to increase its luminosity, by a factor of five beyond its design value. More specifically the current LHC schedule foresees two additional long shutdown periods, LS2 (2019) and LS3 (2024). The upgrades during LS2 concerning the injector chain and the LHC, will eventually lead to a further increased luminosity of $\mathcal{L} = 2 \times 10^{34} cm^{-2}s^{-1}$ or slightly beyond. During LS3 the LHC will be upgraded to HL-LHC aiming to a peak luminosity for ATLAS and CMS of $5 \times 10^{34} cm^{-2}s^{-1}$, sustained over several hours using luminosity leveling techniques compatibly with a maximum average pile-up (the number of events per bunch crossing) with a limit of 140 events/bunch crossing defined by the experiments, and an average integrated luminosity of of 250 fb^{-1} per year with the goal of of 3000 fb^{-1} in about a dozen years after the upgrade.

1.2 The Atlas Experiment

The ATLAS[1] detector, an abbreviation for **A** **T**oroidal **L**HC **A**pparatu**S**, is one of the two general purpose detectors, along with CMS that have been build for studying p-p and Pb-Pb or p-Pb collisions in the LHC. ATLAS is a cylindrical device 44 m long, 25 m in diameter and weights about 7,000 tonnes. It can be divided into four major subsystems:

- The inner detector
- The calorimeters
- The magnet system
- The muon spectrometer

An overview of the detector layout is shown in Figure 1.3

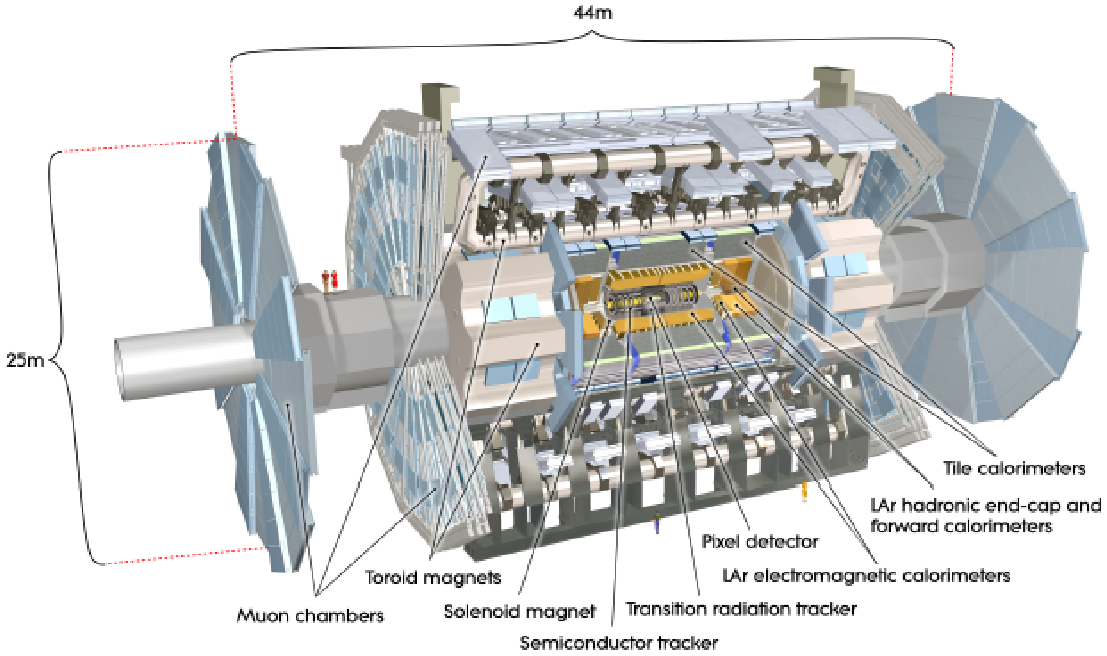

Figure 1.3: An overview of the ATLAS detector. The dimensions of the detector is 25 m in height and 44 n in length. The overall weight of the detector is 7000 tonnes.

Each sub-system is made of multiple multilayers that are complementary to each other. The design of the detector is mainly driven by the need to satisfy a set of general requirement for the LHC detectors:

- Fast, radiation-hard electronics and sensor elements to handle the particle fluxes ans to reduce the influence of overlapping events.
- Large acceptance in pseudorapidity with almost full azimuthal angle coverage.
- Good charged-particle momentum resolution and reconstruction efficiency in the inner tracker.

---

[1] A fully detailed description of the experiment and its design characteristics can be found in [10]

- Very good electromagnetic (EM) calorimetry for electron/photon identification and measurements, complemented by full coverage hadronic calorimetry.
- Good muon identification and momentum resolution over a wide range of momenta.
- Highly efficient triggering on low pT objects with sufficient background rejection to reduce the trigger rate to acceptable levels.

The nominal interaction point is defined as the origin of the coordinate system, while the beam direction is define the z- axis and the x-y plane is transverse to the beam direction. The positive x-axis is defined as pointing from the interaction point to the center of the LHC ring and positive y-axis is defined as pointing upwards. The side-A of the detector is defined as that with positive z and side-C is that with negative z. The azimuthal angle ϕ is measured as usual around the beam axis, and the polar angle θ is the angle from the beam axis. The pseudorapidity is defined as $\eta = ln\ tan(\theta/2)$. The transverse momentum p_T of a particle is defined in the $x - y$ plane unless stated otherwise. Using the notations of the ATLAS coordinate system, the distance ΔR in the pseudorapidity-azimuthal angle is defined as $\Delta R = \sqrt{\Delta\eta^2 + \Delta\varphi^2}$.

1.2.1 Inner Detector

The ATLAS Inner Detector (ID) [15] is designed to provide hermetic and robust pattern recognition, excellent momentum resolution and both primary and secondary vertex measurements for charged tracks above a given p_T threshold and within the pseudorapidity range $|\eta| < 2.5$. It also provides electron identification over $|\eta| < 2.0$ and a wide range of energies (between 0.5 GeV and 150 GeV).

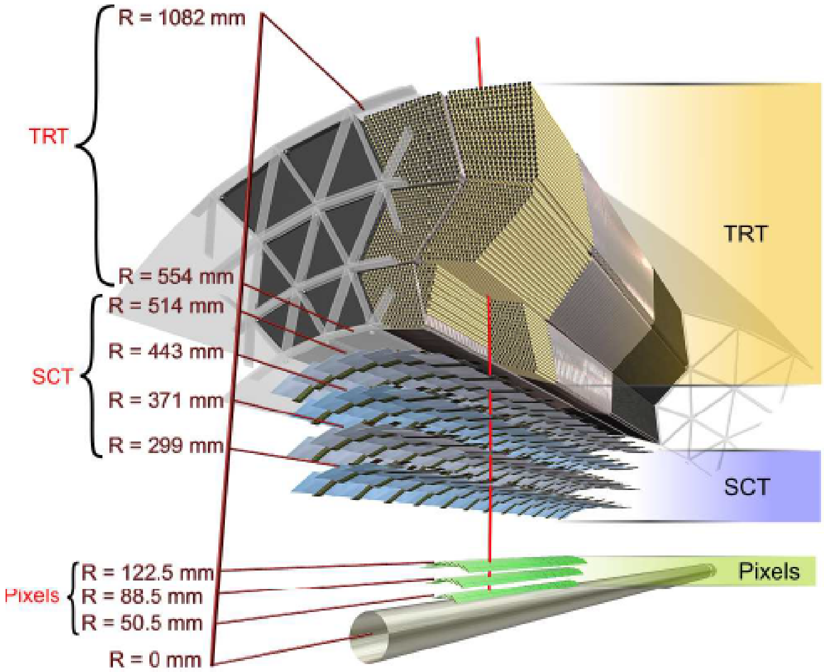

Figure 1.4: A graphical representation of the different parts composing the ID of the ATLAS experiment.

The ID, shown in Figure 1.4, is contained within a cylindrical envelope of length ±3512 mm and of radius of 1150 mm, within a solenoid magnetic field of 2 T. It consists of three independent but complementary sub-detectors. At inner radii, high-resolution pattern capabilities are available using discrete space-points from silicon pixel layers and stereo pairs of silicon microstrip (SCT) layers. The pixel system is mainly in charge of the accurate measurement of vertices whereas the SCT primary functionality is the precise measurement of the particle momenta with the two technologies providing at least three and four particle track reference points respectively. At larger redii, the transition radiation tracker (TRT) comprises many elements of gaseous straw tube elements interleaved with transition radiation material. With an average of 36 hits per track, it provides continuous tracking to enhance the pattern recognition and improve the momentum resolution over $|\eta| < 2.0$ and electron identification, via the detection of transition radiation photons in the straw tubes, complementary to that of the calorimeter over a wide range of energies.

Hits recorded in the individual ID elements are combined to reconstruct the charged particle trajectories inside the tracker and ultimately to measure their kinematic parameters. The accuracy of the reconstruction is limited by a combination of uncertainty contributions including the finite resolutions of the detector elements, the knowledge of the magnetic field, the relative locations of the detector elements and finally the amount of material in the detector. The intrinsic resolution of each pixel detector element, with a size of 50×400 μm^2, can be as good as 10 µm in the measurement of the precision coordinate (115 µm for the perpendicular to the precision one). The slightly coarser (80 µm) SCT elements limit the SCT hit reconstruction uncertainty to 17 µm while the 4mm diameter TRT straws provide a hit position measurement with a resolution of 130 µm. Misalignments or geometrical distortions of the active detector elements deteriorate the resolution of the reconstructed track and may lead to systematic biases on the reconstructed track parameters, thus several trackbased alignment algorithms are employed to optimize the performance of the ID reconstruction.

1.2.2 Calorimeters

The purpose of the ATLAS calorimeters [16] is to accurately measure the energy, position and direction of electrons and photons or jets, and also to evaluate their missing p_T. They are capable of particle identification and contribute in the muon momentum reconstruction. The ATLAS calorimeters consist of a number of sampling detectors with full ϕ-symmetry and coverage around the beam axis. The calorimeters closest to the beam-line are housed in three cryostats, one barrel and two end-caps. The barrel cryostat contains the electromagnetic barrel calorimeter, whereas the two end-cap cryostats each contain an electromagnetic end-cap calorimeter (EMEC), a hadrodnic end-cap calorimeter (HEC), located behind the EMEC, and a forward calorimeter (FCal) to cover the region closest to the beam. All these calorimeters use liquid argon as the active detector medium. Liquid argon has been chosen for its intrinsic linear behavior, its stability of response over time and its intrinsic radiation-hardness.

The precision electromagnetic calorimeters are lead-liquid argon detectors with accordion-shape absorbers and electrodes. This geometry allows calorimeters to have several active layers in depth, three in the precision-measurement region ($0 < |\eta| < 2.5|$) and two in the high-η region ($2.5 < |\eta| < 3.2$) and in the overlap region between the barrel and the EMEC. In the precision-measurement region, an accurate position measurement is obtained by finely segmenting the first layer in η. The η direction of photons is determined by the position of the photon cluster in the first and second layers.

The calorimeter system also has electromagnetic coverage at higher η ($3.1 < |\eta| < 4.9$) provided by the FCal. Furthermore in the region ($0 < |\eta| < 1.8$) the electromagnetic calorimeters are complemented by presamplers, an instrumented argon layer, which provides a measurement of the energy lost in front of the electromagnetic calorimeters.

For the outer hadronic calorimeter, the sampling medium consists of scintillator tiles and the absorber medium is steel. The tile calorimeter is composed of three parts, one central barrel and two extended barrels. The choice of this technology provides maximum radial depth for the least cost for ATLAS. The tile calorimeter covers the range $0 < |\eta| < 1.7$ (central barrel and extended barrels). The hadronic calorimetry is extended to larger pseudorapidities by the HEC, copper/liquid-argon detector, and the FCal, copper-tungsten/liquid-argon detector. The hadronic calorimetry thus reaches one of its main design goals, namely coverage of $|\eta| < 4.9$. A graphical representation of the ATLAS calorimeters is presented in Figure 1.5.

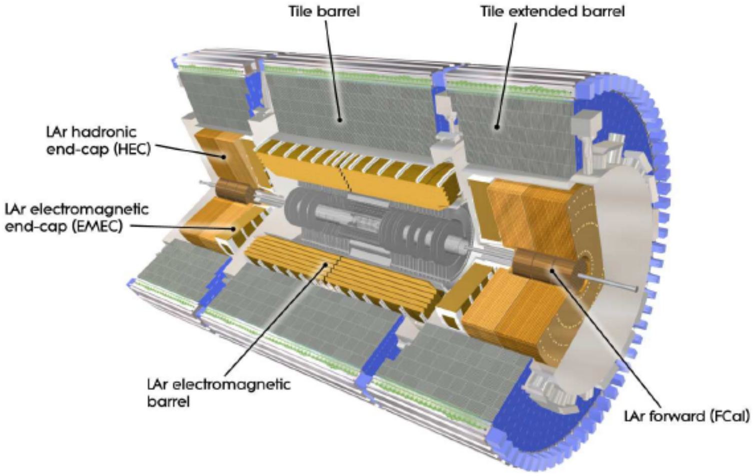

Figure 1.5: A graphical representation of the ATLAS calorimeter cross-section.

1.2.3 Magnet System

ATLAS features a unique hybrid system of four large super conducting magnets, in order to measure the momenta of the charged particles produced during the collisions. This magnetic system [17] is 22 m in diameter and 26 m in length, with a stored energy of 1.6 GJ. Figure 1.3 shows the general layout, the four main layers of detectors and the four superconducting magnets which provide the magnetic field over a volume of approximately 12.000 m^3 (defined as the region in which the field exceeds 50 mT). The spatial arrangement of the coil windings is shown in Figure 1.6. The ATLAS magnet system consists of:

- a solenoid which is aligned on the beam axis and provides a 2 T axial magnetic field for the inner detector, while minimizing the radiative thickness in front of the barrel electromagnetic calorimeter.
- a barrel toroid and two-end cap toroids, which produce a toroidal magnetic field of approximately 0.5 T and 1 T for the muon detectors in the central and end-gap regions, respectively.

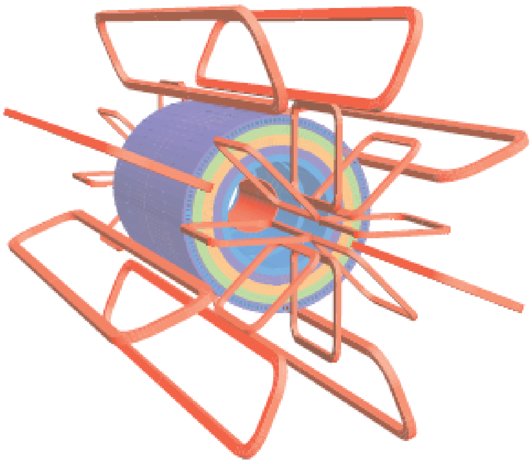

Figure 1.6: Geometry of magnet windings and tile calorimeter steel. The eight barrel toroid coils, with the end-cap coils interleaved are visible.

The superconducting ATLAS magnet system is cooled by liquid helium at 4.8 K. In terms of power, the toroids are electrically connected in series and likewise operated at a current of 20 kA while the central solenoid operates at a lower nominal current 7.6 kA.

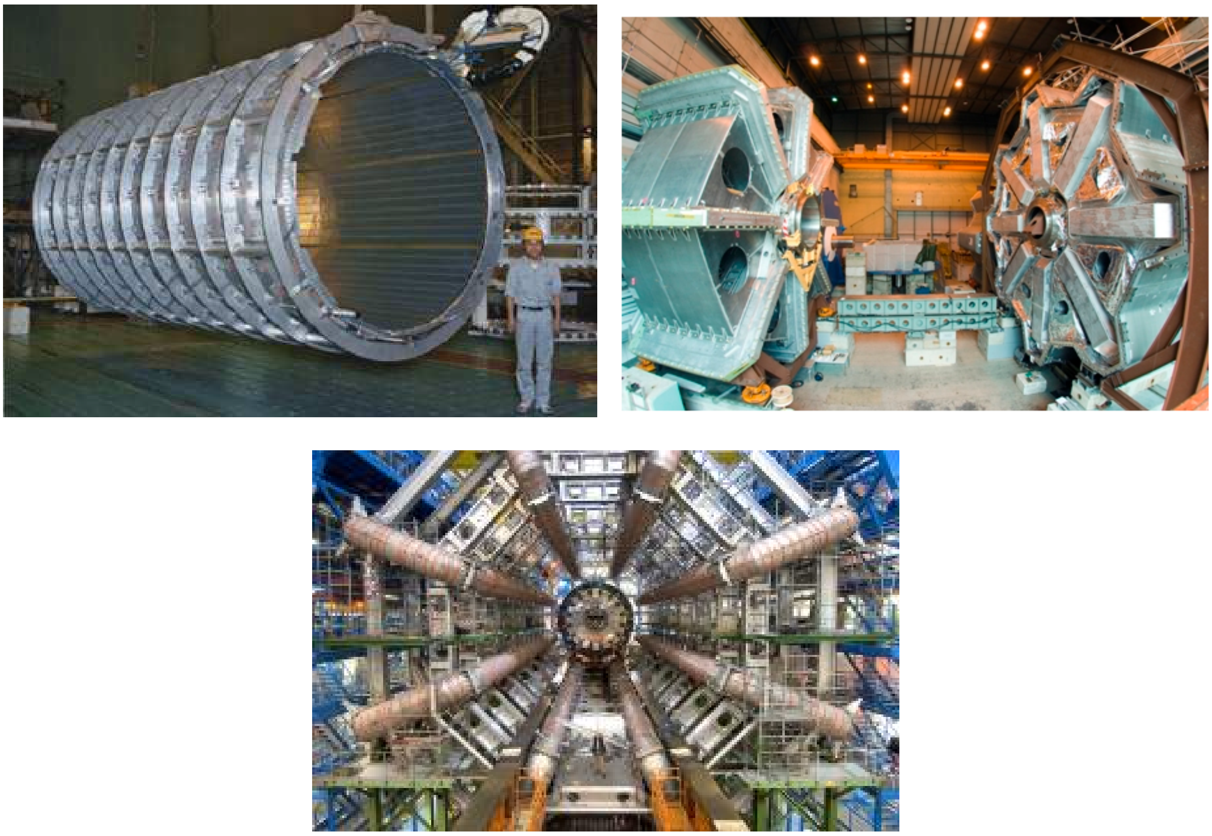

Figure 1.7: Photos of the different parts of the ATLAS magnet system during their assembly and installation in the ATLAS cavern.

In figure 1.7 the different parts of the magnet system can be observed. In the upper left picture the bare central solenoid in the factory after completion of the coil winding is shown. In the upper right picture we can see the preparation of the end-cap toroids.

Finally a view of the eight barrel toroid coils installed in the ATLAS cavern is presented in the bottom picture.

1.2.4 The ATLAS Muon Spectrometer

The muon spectrometer [18] forms the outer part of the ATLAS detector and is designed to detect charged particles exiting the barrel and end-cap calorimeters and to measure their momentum in the pseudorapidity range of $|\eta| = 2.7$. It is also designed to trigger on these particles in the region $|\eta| < 2.4$. Its principle of operation is based on the magnetic deflection of muon tracks by a system of three large superconducting air-core toroid magnets providing high resolution muon momentum measurement.

Precision-tracking chambers in the barrel region are located between and on the eight coils of the superconducting barrel toroid magnet, while the end-cap chambers are in front and behind the two end-cap toroid magnets. The ϕ symmetry of the toroids is reflected in the symmetric structure of the muon chamber system, consisting of eight octants. Each octant is subdivided in the azimuthal direction in two sectors with slightly different lateral extensions, a large and a small sector, leading to a region of overlap ϕ. This overlap of the chamber boundaries minimizes gaps in detector coverage and also allows for the relative alignment of adjacent sectors using tracks recorded by both a large and a small chamber.

The chambers im the barrel are arranged in three concentric cylindrical shells around the beam axis at radii of approximately 5 m, 7.5 m and 10 m. In the two end-cap regions, muon chambers form large wheels, perpendicular to the z-axis and located at distances of $|z| \approx$7.4m, 10.8 m, 14 m and 21 m from the interaction point. Figure 1.8 gives cross sections in the planes transverse to, and containing, the beam axis while Figure 1.9 shows the overall layout of the muon system.

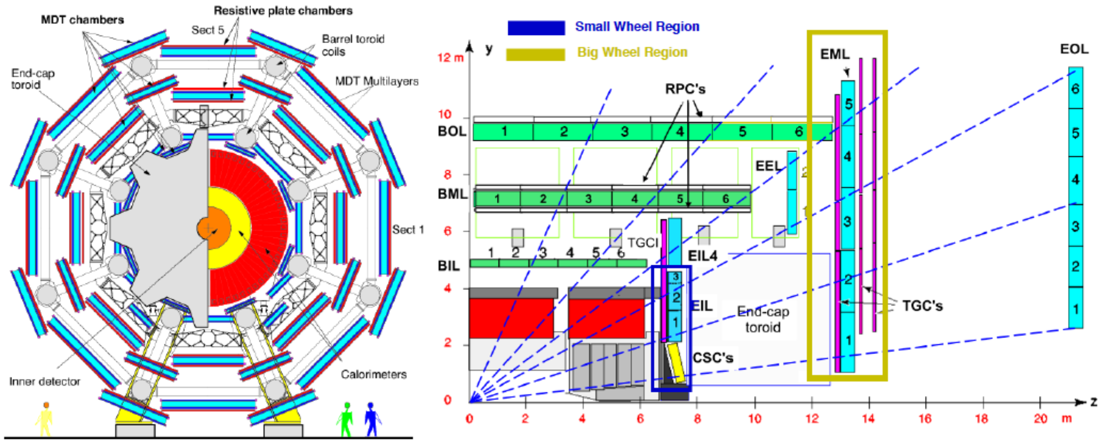

Figure 1.8: Left: Cross-section of the barrel muon system perpendicular to the beam axis (non-bending plane), showing three concentric cylindrical layers of eight large and eight small chambers. The outer diameter is about 20 m. Right: Cross-section of the muon system in a plane containing the beam axis (bending plane). Infinite-momentum muons would propagate along straight trajectories which are illustrated by the dashed lines and typically traverse three muon stations.

The four technologies chosen to equip the muon spectrometer are:

- Cathode Strip Chambers (CSC)
- Monitored Drift Tubes (MDT)
- Resistive Plate Chambers (RPC)
- Thin Gap Chambers (TGC)

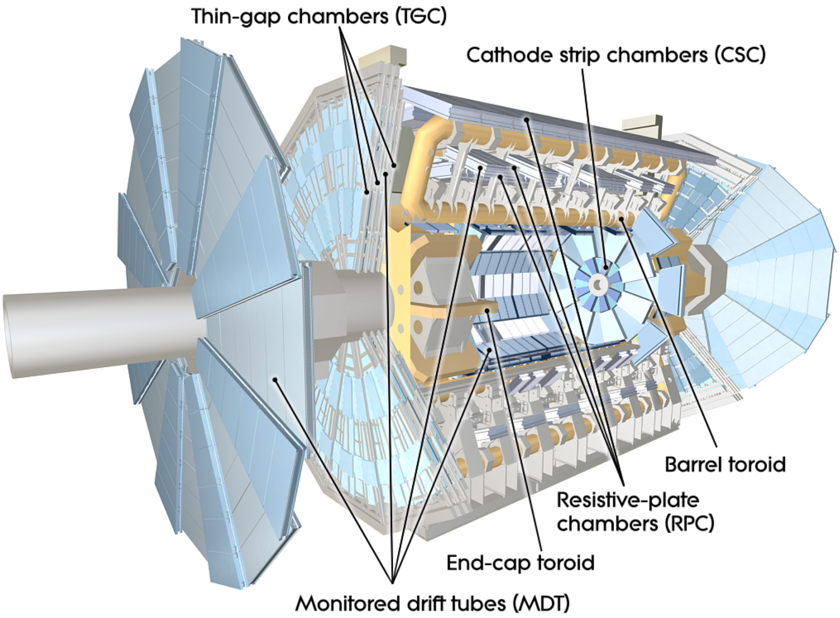

Figure 1.9: Cut-away view of the ATLAS muon system.

Cathod Strip Chambers

The CSC are multiwire proportional chambers with cathode strip readout and symmetric shell in which the anode-cathode spacing is equal to the anode wire pitch. Its layout as well as the detector internal structure is shown in Figure 1.10.

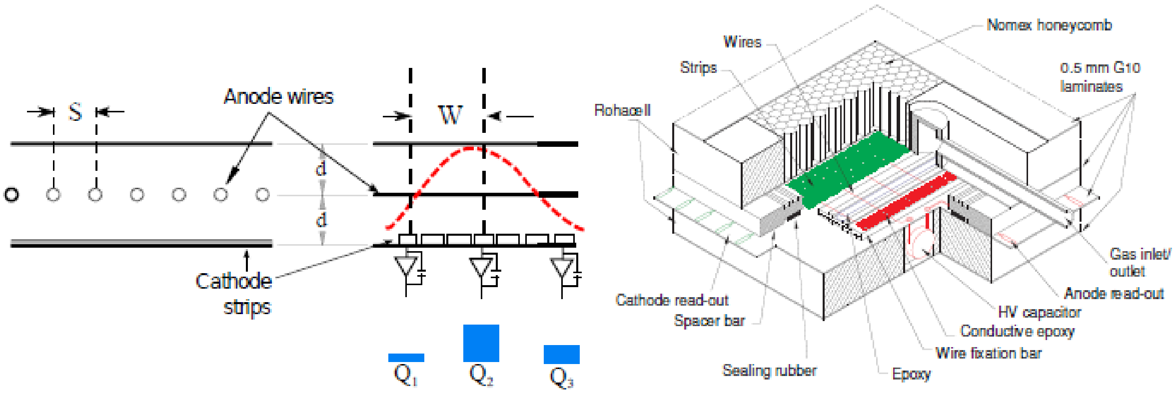

Figure 1.10: Left: Schematic layout of a CSC detector working principle. Right: CSC internal structure.

The precision coordinate is obtained by measuring the charge induced on the segmented cathode strips by the avalanche formed on the anode wire. The cathode strips are oriented orthogonal to the anode wire.

They are located in the two innermost end caps, the so called ”Small Wheels (SW)”, covering the largest rapidity region $2 \leq |\eta| \leq 2.7$ that is characterized by the highest particle flux among the muon spectrometer stations. CSC are arranged in four layers equipping only the small wheel in a segmentation of 16 sectors per wheel. They are operated with a gas mixture of Ar+20%CO_2 at atmospheric pressure.

Monitored Drift Tubes

The MDT cover almost the full rapidity region of the ATLAS Muon Spectrometer $|\eta| \leq 2.7$ apart of the high rapidity region of the SW where CSC are used. The basic element of the monitored drift tube chambers is a pressurized drift tube with a diameter of 29.970 mm, operating with Ar+7%CO_2 at 3 bar. The electrons resulting from ionization are collected at the central tungsten-rhenium wire with a diameter of 50 μm. The tube lengths varies from 70 cm up to 630 cm. They are arranged in multilayer of three or four tube layers on either side of a support structure. Each drift tube is readout at one end. Figure 1.11 shows a schematic view of a MDT chamber (left) and a cross-section of a MDT tube (right).

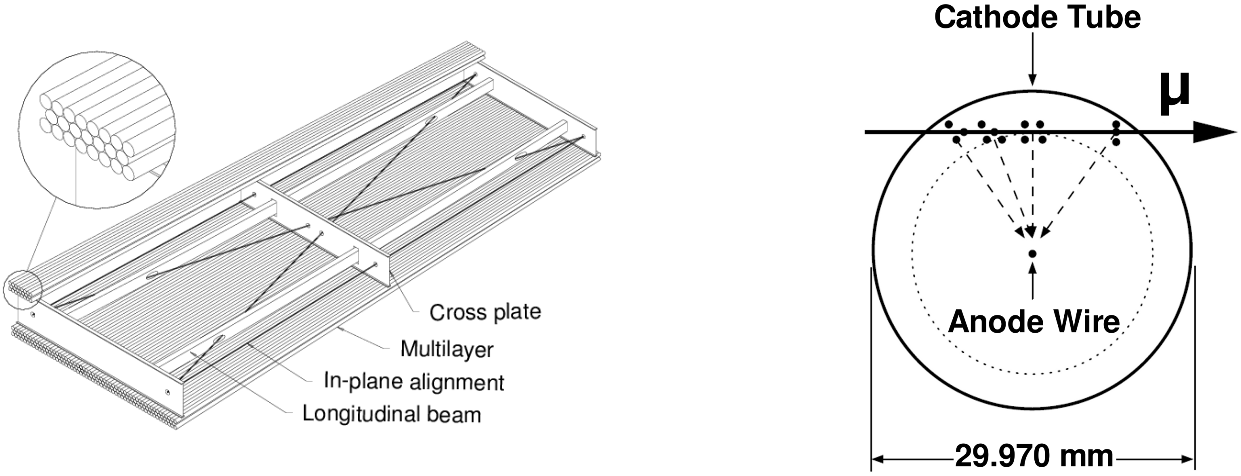

Figure 1.11: Left: Schematic view of a MDT chamber. Right: Cross-section of a MDT tube.

Resistive Plate Chambers

The RPC system is located at the barrel region ($|\eta| < 1.05$) and is responsible to provide trigger signals. The RPC chamber is a electrode-plate (no wire) detector. Two resistive plates made of phenolic-melaminic plastic laminate, are kept parallel to each other at a distance of 2 mm by insulating spacers. The electric field between the plates of about 4.9 kV/mm allows avalanches to form along the ionizing tracks towards the anode. The signal is read out via capacitive coupling to metallic strips, which are mounted on the outer faces of the resistive plates. The gas used is a mixture of $C_2H_2F_4$:4.5%i-C_4H_10:0.3%SF_6 which combines relatively low operating voltage (due to the low F_6 concentration), no flammability and low cost, while providing a comfortable plateau for safe avalanche operation. The RPC chamber is able to provide a timing measurement with an accuracy of the order of 1ns fulfilling the requirements of the ATLAS trigger system. Moreover, being a fast detector technology the RPC are also characterized by BC identification capability. Additionally, their fast and coarse tracking can be used for identifying the hits of the precision chambers that are related to the detected muon track.

The RPC system layout, optimum for the barrel trigger performance, consists of three stations with each one comprising two detection layers. The two middle stations, installed with a lever arm of 50 cm in between are located near the center of the magnetic field region and provide the low p_T muon trigger while the third station, at the outer radius of the magnet, allows for a more relaxed p_T threshold, thus providing the high p_T muon trigger. The structure of a RPC chamber is shown in Figure 1.12.

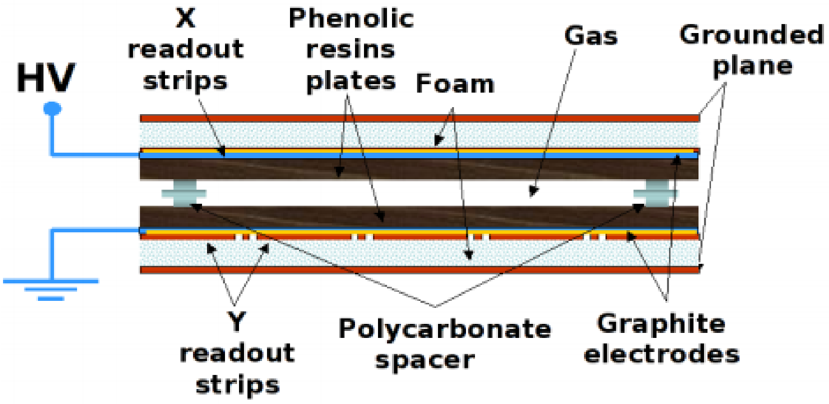

Figure 1.12: Structure of a Resistive Plate Chamber of the ATLAS experiment.

1.3 The ATLAS New Small Wheel Upgrade Project

Already, after the end of the first long shutdown (LS1) the accelerator's energy was increased at the design value of 7 TeV which corresponds to a luminosity of the order of $\mathcal{L} = 10^{34} cm^{-2} s^{-1}$. After the second long shutdown (LS2) in 2018, the accelerator luminosity will be increased to 2-3 $\times 10^{34}$ $cm^{-2}s^{-1}$, allowing ATLAS to collect approximately 100 fb^{-1}/year. A subsequent upgrade is planned which will make significant changes to the interaction point (IP) region in addition to improvements to the other parts of the accelerator complex. These improvements will result in the luminosity increasing to 5 $\times 10^{34}$ $cm^{-2}s^{-1}$ (with luminosity leveling). The integrated luminosity with this ultimate upgrade will be 3000 fb^{-1} after about ten years of operation.

The ATLAS experiment was designed for a broad physics program, including the capability of discovering the Higgs boson over a wide mass range and performing searches for the production of heavy particles that would indicate physics beyond the standard model, such as SUSY particles, as well as searches for other massive objects. In order to maintain its current excellent performance and to cope with the corresponding increase in the particle rate that is expected, the ATLAS detector must be upgraded to have better performance at higher luminosity, following the same schedule as the LHC upgrade. Figure 1.13 shows the current LHC and ATLAS upgrade schedule.

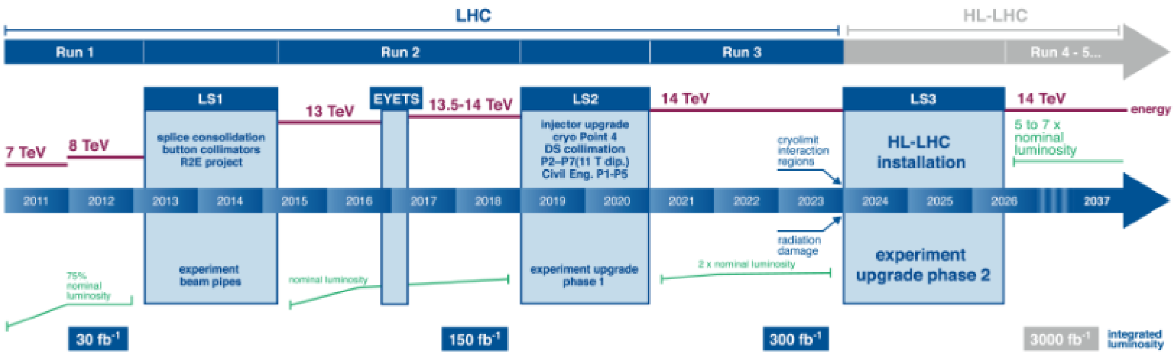

Figure 1.13: The LHC baseline schedule as of 22.02.2016 [1]

1.3.1 Upgrade of the muon spectrometer-New Small Wheels

The Phase-I upgrade[2] of the ATLAS muon spectrometer focuses on the end-cap region, the so called Small Wheel (SW) that is composed of CSC, MDT and TGC detectors. Figure 1.8 (right) shows a cross section of one quarter of the ATLAS detector in zy plane. The area of interest, marked with a blue square, is located in the region 6-8 m in z and 1-5 m in y. The barrel system covers the η of $|\eta| < 1.0$ whereas the end-cap system covers the $1.0 < |\eta| < 2.7$ for muon tracking and $1.0 < |\eta| < 2.4$ for Level-1 trigger. The barrel and end-cap systems consist of three stations each, measuring the muon momentum based on the curvature in the ATLAS toroid magnets.
At high luminosity the following two points are of particular importance:

- The performance of the muon tracking chambers (MDT and CSC): mainly in the end-cap region, there is a significant degrade of performance both in terms of efficiency and resolution with the expected increase of the cavern background rate.

- The Level-1 muon trigger in the end-cap region:a significant part of the muon trigger-rate in the end-caps is background leading to trigger rate of eight to nine times higher than that in the barrel region.

Both of these two issues represent a serious limitation on the ATLAS performance beyond design luminosity: reduced acceptance of good muon tracking, and an unacceptable rate of fake high p_T Level-1 muon triggers coming from the forward direction.

Efficiency and Tracking Performance

The luminosity increase will result in higher particle rates. More specifically, in the Small Wheel region at pseudorapidity $\eta = \pm 2.7$, rates up to 15 kHz/cm^2 are expected. The current SW detectors (MDT, TGC, CSC) will be unable to handle efficiently the increased rate. This aspect can be seen in Figure 1.14 where the single tube hit efficiency and the segment finding efficiency of the MDT is illustrated. It can be clearly observed that the efficiency decreases linearly with increasing hit rate. At a hit rate of 300 kHz (the maximum rate expected for a luminosity of $1 \times 10^{34} cm^{-2} s^{-1}$) it already reaches hit inefficiencies of about 35%. The segment finding efficiency is higher since only a subset of all available hits is required but for rates above 300 kHz it also decreases dramatically. With tube rates above 300 kHz, the segment inefficiency becomes sizable and results in a degradation of spectrometer performance. High background rate also causes degradation

---

[2] A comprehensive description of the New Small Wheel upgrade principles can be found in [19] and [20].

of the position resolution due to space charge effects. Hence a big fraction of the current Small Wheel MDT system suffers from substantial single hit and segment inefficiency.

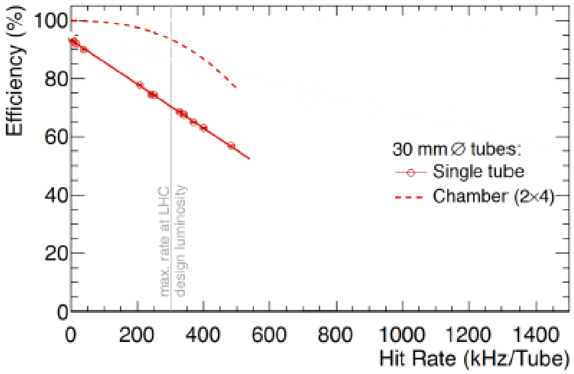

Figure 1.14: MDT tube hit (solid line) and track segment efficiency (dashed line, referring to a MDT chamber with 2 × 4 tube layers) as a function of tube rate estimated with test-beam data at the designed luminosity of $10^{34} cm^{-2} s^{-1}$. The plot is taken from [2].

End-cap Muon Trigger

The Level-1 muon trigger in the end-cap region is based on track segments in the TGC chambers of the middle muon station (End-cap Muon Detector, EM) located after the end-cap toroid magnet. The transverse momentum, p_T, is determined by the angle of the segment with respect to the direction pointing to the interaction point. A significant part of the muon-trigger rate in the end-caps is background. Low energy particles,mainly protons, generated in the material between the Small Wheel and the EM station, produce fake triggers by hitting the end-cap trigger chambers at an angle similar to that of high p_T muons. This situation is illustrated in Figure 1.15.

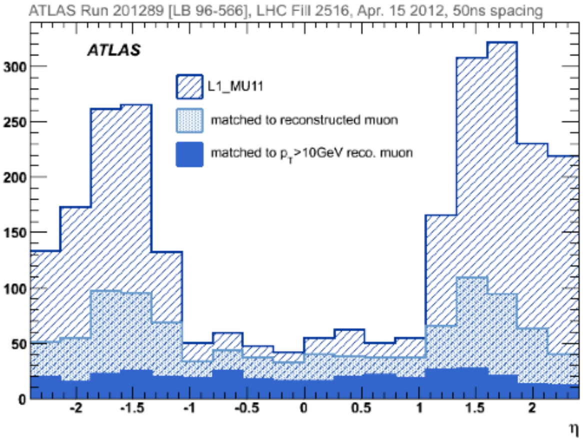

Figure 1.15: The η distribution of Level-1 trigger rate at three levels. The dashed distribution shows the trigger rate of the muon system while the distribution in light blue those triggers matched with a muon segment in the inner detector. The solid blue distribution shows the reconstructed muons with p_T larger than 10 GeV/c. The plot is taken from [2].

The dashed histogram represents the η distribution of ATLAS Level-1 muon trigger candidates. The distribution of the trigger candidates that match offline reconstructed muon tracks is also shown before and after a selection cut of $p_T > 10$ GeV. A big fraction of the reconstructed muons cannot be matched to a candidate from the inner detector. These fake triggers are approximately 90% of the total triggers.

1.3.2 The main elements of the upgrade

In order to deal with these two issues, the degraded muon track reconstruction performance and the increased muon trigger rates, the SW will be replaced by the New Small Wheel (NSW). The NSW consists of a set of precision tracking detectors that are fast, capable to perform bunch crossing identifications at rates up to 15 kHz/cm^2 and have spatial resolution of less then 100 µm per detection plane. The NSW detectors can therefore provide the muon trigger system with reconstructed track segments of good angular resolution, greater than 1 mrad, that can clearly indicate whether the triggered muons originated from the collision point or not. An illustration of the tracking principle is illustrated in Figure 1.16. The existing ATLAS Big Wheel trigger accepts all three tracks shown. The fake tacks, B and C, can be rejected in the trigger by the addition of the New Small Wheel.

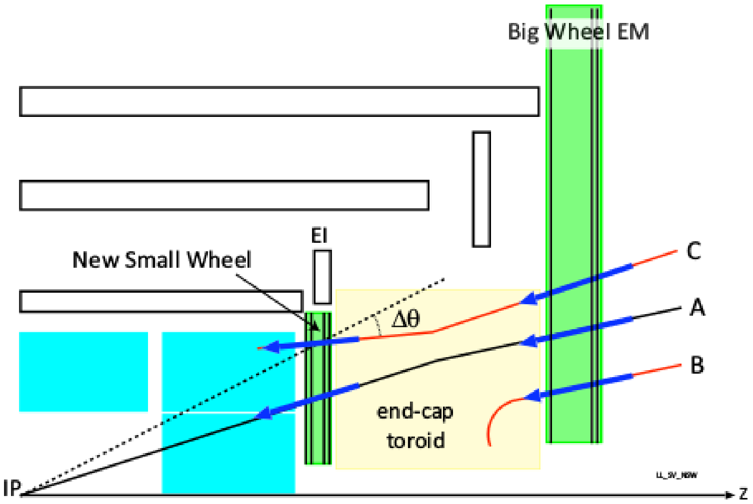

Figure 1.16: Schematic of the ATLAS muon trigger. The existing Big Wheel trigger accepts all three tracks shown. The fake tracks (B and C) can be rejected in the trigger by the addition of the New Small Wheel. The plot is taken from [2].

1.3.3 Detector Technologies and Layout

The New Small Wheel will consist of two detector technologies both coming from the family of gaseous detectors: small-strip Thin Gap Chambers (sTGC) as the primary trigger and Micromegas (MM) as the primary precision tracker.

sTGC Technology

The sTGC whose concept developed in 1984 will be the primary trigger detector featuring BC identification capability and angular resolution for online reconstructed segments better than 1 mrad. The basic structure of sTGC is shown in Figure 1.17. It consists of a grid of 50 µm gold plated tungsten wires at a potential of 2.9 kV, with a 1.8 mm pitch, sandwiched between two cathode planes at a distance of 1.4 mm from the wire plane. The cathode planes are made of a graphite-epoxy mixture with a typical surface resistivity of 100 kΩ/□ sprayed on a 100 μm thick G-10 plane, behind which there are on one side precision strips (that run perpendicular to the wires) and on the other pads (covering large rectangular surfaces), on 1.6 mm thick printed circuit board (PCB) with the shielding ground on the opposite side. The strips have have a 3.2 mm pitch, mush smaller than the strip pitch of the ATLAS TGC, hence the name ”small-strip TGC” for this technology. The pads are used to through a 3-out-of-4 coincidence to identify muon tracks roughly pointing to the interaction point. They are also used to define which strips need to be readout to obtain a precise measurement in the bending coordinate (region of interest), for the online event selection. The azimuthal coordinate is obtained from the wires. The operational gas is mixture of 55% CO_2 and 45% n-pentane.

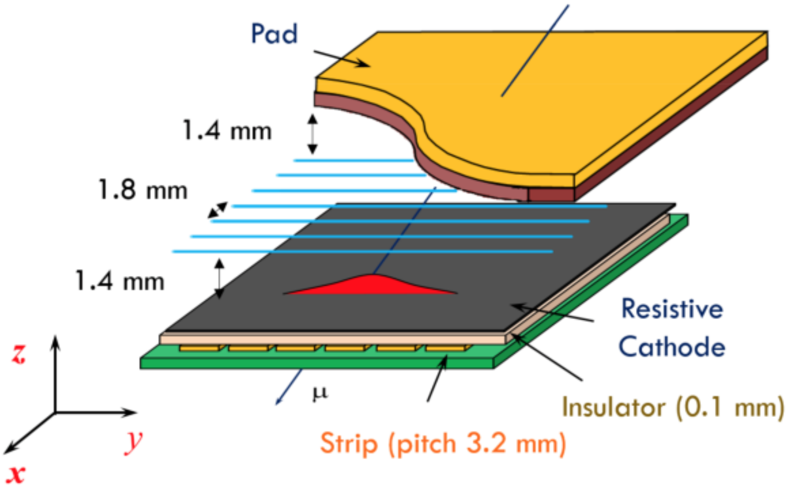

Figure 1.17: Schematic view of sTGC internal structure.

Micromegas

Given its excellent spatial resolution performance ($\sigma \leq 100\ \mu m$) and good track separation due to the fine readout granularity, the MM main role will be mainly in the tracking sector. The main characteristics of this technology will be described later in detail in the next chapters as it is the main subject of this thesis.

Detector Layout

The NSW will comprise two detector technologies: small-strip Thin Gap Chambers (sTGC) as the primary trigger and Micromegas (MM) as the primary precision tracker. The NSW consists of 16 detector planes arranged in two multilayers separated by a spacer frame of 50 mm. Each multilayer utilizes four sTGC and four MM detector planes. An arrangement where the inner part of the wedge is occupied by micromegas detectors while the outer part is occupied by sTGC detectors is used in order to maximize the distance between the two sTGCs multilayers for improved track segment angular resolution at the tracking level. In Figure 1.18 a drawing of the NSW is illustrated. It consists of 16 sectors, 8 large and 8 small.

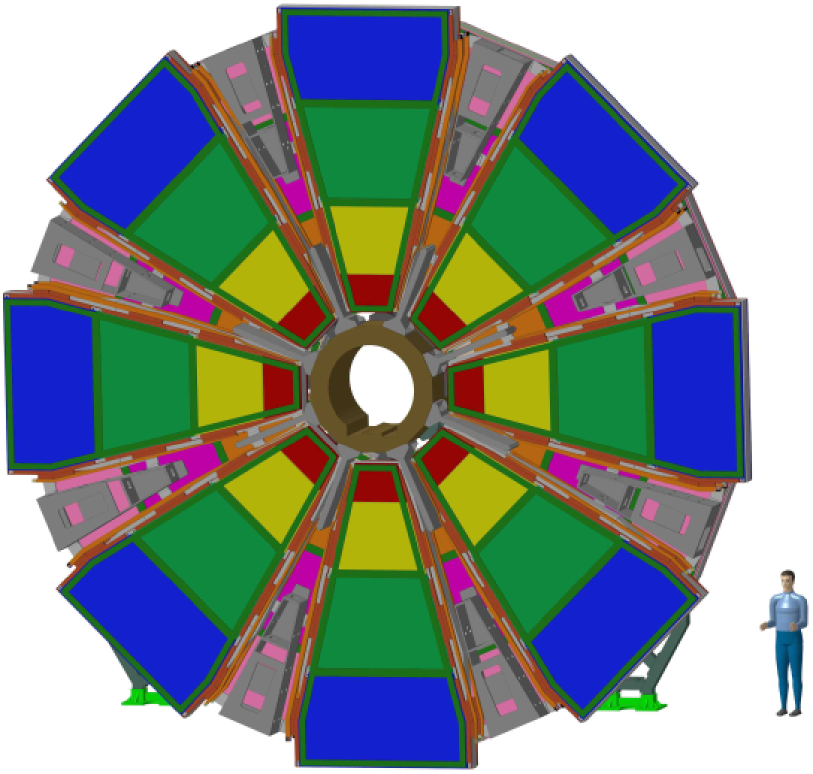

Figure 1.18: Schematic of the New Small Wheel detector.

Chapter 2

Interaction of Charged Particles with Matter

2.1 Interactions of Charged Particles and Energy Loss

The operation principal of a any particle detector is based on the interactions between the incoming charge particles and the detection medium. Then the products of these interactions are collected and transformed into a readable signal. Here the main mechanisms that rule these interactions are presented in a concise way.

When a charged particle crosses a material, it is subjected to the coulombic forces from the electrons and nuclei present in the material. In the case where the charged particle is a hadron (for example an alpha particle or a proton), it can also undergo a nuclear interaction, a possibility that we will ignore. The particle senses the electromagnetic fields of the electrons and nuclei and collides elastically with them transferring a small amount of its initial energy. Using non-relativistic kinematics and energy-momentum conservation, it can be derived that the maximum energy transfer of a heavy charged particle m with a nucleus of mass M is given by:

$$\Delta E_{max} = \frac{1}{2} m v^2 \left(\frac{4mM}{(m+M)^2} \right) \tag{2.1}$$

In the case that mass m is much smaller than mass M we will have:

$$\Delta E_{max} \approx \frac{1}{2} m v^2 \left(4\frac{m}{M} \right) \qquad (m \ll M) \tag{2.2}$$

During its collision with the much heavier nuclei the particle, for example a proton, loses little amount of energy but its direction can be shifted dramatically. In the other hand in collisions with electrons a large amount of the particle's energy can be transferred to the electrons but the direction undergoes only a small alteration. As a result most of the energy loss of the heavy charged particle is due to the collisions with the electrons and most of the change of direction is due to the collisions with the nuclei.

The loss of kinetic energy by charged particles traveling through a material can be broken into two components depending on the mechanism of energy transfer, either collisional or radiative energy loss. The total *stopping power* is:

$$\frac{dE}{dx} = \left(\frac{dE}{dx}\right)_{col} + \left(\frac{dE}{dx}\right)_{rad} \tag{2.3}$$

where $(dE/dx)_{col}$ is the electronic energy loss due to Coulomb interactions (ionization and excitation), and $(dE/dx)_{rad}$ is the nuclear energy loss (for example due to Bremmsstrahlung emission or Cerenkov radiation and nuclear interactions).

Excitation raises an electron to a higher energy shell, whereas *ionization* completely removes the electron from the atom. During ionization an *ion pair* is created, which consists of the newly freed electron and the positively charged atom from which the electron was removed. Some of these free electrons acquire sufficient energy to travel macroscopic distances in matter and they are able to cause further ionization in the material. These high-energetic electrons are sometimes called δ-electrons (or *delta rays*). As a result any charged particle penetrating the matter leaves behind a trail of excited atoms and free electrons that have acquired some energy in the collision.

In the previous expression the term $(dE/dx)_{col}$ is also called *Linear Energy Transfer* (LET), which is the linear rate of energy loss of a charged particle due to ionization and excitation:

$$LET = \frac{dE}{dx} \tag{2.4}$$

The mean rate of energy loss per unit length for high-energy charged particles is given by *Bethe-Bloch equation*:

$$\left\langle -\frac{dE}{dx} \right\rangle = Kz^2 \frac{Z}{A} \frac{1}{\beta^2} \left[\frac{1}{2} \ln \frac{2m_e c^2 \beta^2 \gamma^2 E_{max}}{I^2} - \beta^2 - \frac{\delta(\beta\gamma)}{2} \right] \tag{2.5}$$

where the symbols used in the above equation are defined below:

dE/dx: energy loss of particle per unit length
K: $4\pi N_A r_e^2 m_e c^2$ $(0.307075\ MeV mol^{-1} cm^2)$
N_A: Avogadro's number $(6.02214129(27) \times 10^{23}\ mol^{-1})$
r_e: classical electron radius ($e^2/4\pi\epsilon_0 m_e c^2$ (2.8179403267(27) fm))
$m_e c^2$: electron mass$\times c^2$ (0.510998928(11) MeV)
z: charge number of incident particle
Z: atomic number of absorber
A: atomic mass of absorber $(gmol^{-1})$
β: $\frac{v}{c}$ where v is the velocity of the incident particle
I: mean excitation energy (eV)
E_{max}: maximum energy transfer (to the electron) possible in a single collision
$\delta(\beta)$: density effect correction to ionization energy loss (for gases under normal pressure this term can be neglected)

The previous equation is valid only if the velocity of the incident particle is much larger than the velocity of the electrons in atoms. For slow particles with velocities that are comparable to those of the atomic electrons or slower, the energy loss increases with the energy (the energy loss is actually proportional to β) and reaches a maximum when the particle velocity is equal with the typical electron velocity (the velocity of electrons in atomic orbits is of the order of 1% of the velocity of light). After these maximum the energy loss decreases following the Bethe-Bloch formula.

Given this condition, the energy loss decreases rapidly like $1/\beta^2$ as the $\beta\gamma$ increases. The energy loss curve reaches a broad minimum near $\beta\gamma \approx 4$. Relativistic particles, with velocity that approaches the speed of light and $\beta \approx 1$, which have an energy loss corresponding to this minimum, are called *minimum ionizing particles* (MIP's). For these particles the energy loss due to ionization ranges, for almost all materials, between 1 and 2 Mev/(g/cm^3).

In Figure 2.1 we can see the energy loss versus the kinetic energy of different charge particles in the air. For all particles the energy loss decreases with increasing energy and eventually reaches a constant energy-independent value which is the same for almost all particles of unit charge.

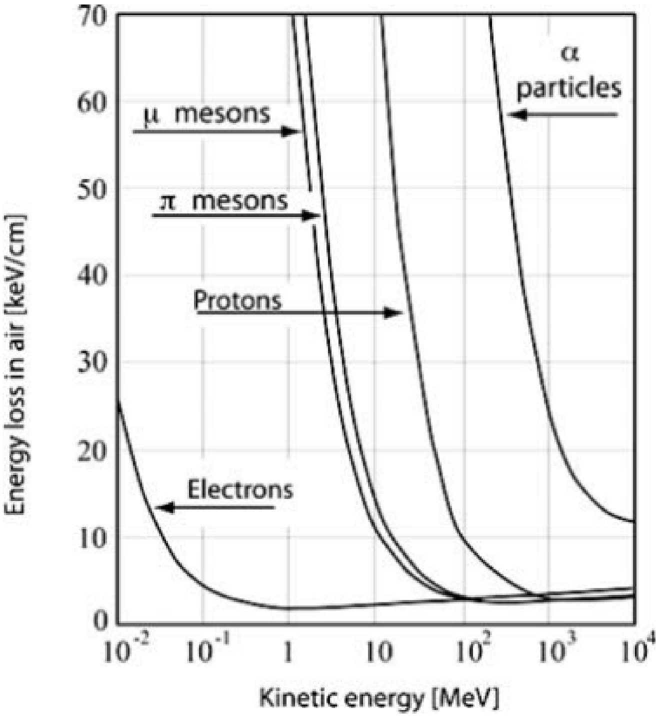

Figure 2.1: Energy loss in air vs the kinetic energy for some charged particles. The plot is taken from [3].

As the energy increases more ($\beta\gamma > 4$) the energy loss raises again because of the increasing contribution of the logarithmic term in the brackets of (2.5). This behavior is called *logarithmic rise* or *relativistic rise* of the energy. A considerable amount of the relativistic rise comes from the large energy transfer to few electrons in the medium, the so called δ *rays*.

For further energy increase, the logarithmic rise is depreciated due to the contribution of the $\delta(\beta\gamma)/2$ which is the last term in (2.5). This correction represents the so called *density effect*, which is related to the screening of the incident's particle electric field from the polarization of the atoms close to the particle's trajectory. Due to this effect the energy loss curve reaches a constant value, the *Fermi plateu.* At even higher energies radiative effects take place whose contribution to the energy loss is more important than the ionization. The δ term which is a function of the material density, in the case of gases with normal pressure, can be neglected.

2.2 Particle Range and Bragg Peak

As we saw in the previous section, a charged particle loses energy when traveling in a material. Eventually it will lose all of its initial kinetic energy and will come at rest. The total distance traveled by the particle until it is stopped is called its *range*. The range of muons, pions and protons in different materials is illustrated in Figure 2.2

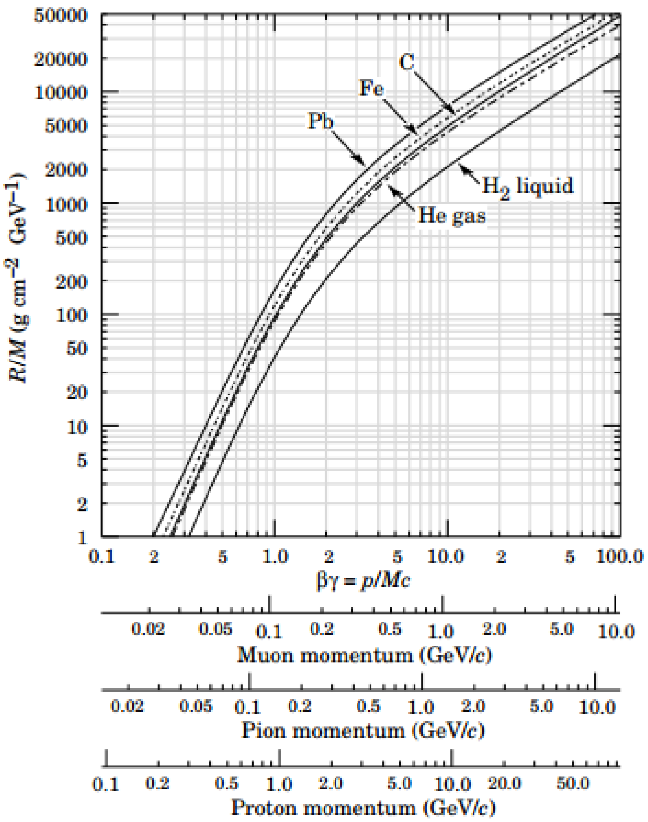

Figure 2.2: Range of muons, pions and protons for a variety of materials. The plot is taken from [4].

As the particle penetrates in the material its energy loss per unit length will change. The energy loss of a particle as a function of its distance of penetration is illustrated in Figure 2.3. This curve demonstrates at its most part a rising behavior with the decreasing of the particles kinetic energy. The energy loss close to the end of the range reaches a maximum and then suddenly drops to zero. This maximum of the energy loss of charged particles close to the end of their range is referred to as the *Bragg peak*. The drop of the curve is due the fact that at low energies the charge exchange between the incident particle and the absorber becomes dominant leading to the minimization of the particle's charge.

The statistical nature of energy loss process inherits a variance to the range values of a particle for a given absorber. This fluctuation of a particle's range is called *range straggling* and suggests that, due to statistical reasons, particles in the same medium have varying path lengths between the same initial and final energies.

Let us consider a monoenergetic beam of heavy charged particles penetrating a material, the thickness of which can be changed at will, and a detector positioned at the end of the layout to measure the particles exiting the material. Considering that the trajectory of the particles remain constant and that the detector is able to detect all the particles independently of their energy, the number of particles coming through the material of thickness d, follows the diagram which is illustrated in Figure 2.4.

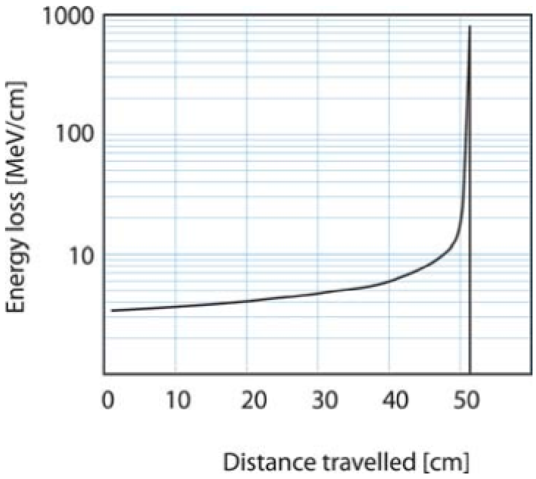

Figure 2.3: Energy loss of a proton of 300 MeV along its trajectory in water. The plot is taken from [3].

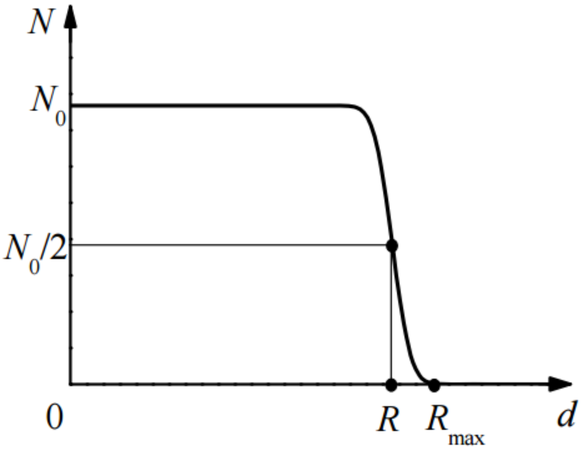

Figure 2.4: Number of heavy charged particles which travel through a medium of thickness d. The tail of the distribution represents the range straggling.

For small thickness values of the absorber, the particles penetrate the material losing just a fraction of their initial energy and without undergoing any change in their direction or motion. Thus the observed number of particles coming through the material is constant. This situation is changed when thickness of the material approaches the particle's range. Then some particles lose all their energy and do not reach the detector, so the count rate drops abruptly. The thickness value for which the number of particles detected is one-half of the original value is called *mean range* (R point), while the thickness value at which no particles are detected, is called *expected range*.

2.3 Energy Fluctuations

The Bethe-Bloch equation gives only the average energy loss of charged particles by ionization and excitation. For detectors of moderate thickness, strong fluctuations around the mean value of energy loss appear due to high energetic δ-electrons. This behavior can be parameterized by a *Landau distribution.* The *most probable energy loss* is given by:

$$\Delta_p = \xi \left[\ln \frac{2mc^2\beta^2\gamma^2}{I} + \ln \frac{\xi}{I} + j - \beta^2 - \delta(\beta\gamma) \right] \tag{2.6}$$

where $\xi = (K/2) < Z/A > (x/\beta^2)$ MeV for a detector of thickness x in $g\ cm^{-2}$ and j=0.200. The density correction $\delta(\beta\gamma)$, for high energies ($\beta\gamma \gtrsim 100$), leads the most probably energy loss to a Fermi plateau. In Figure 2.5 we can see the straggling functions for 500 meV pions in silicon for different values of thickness.

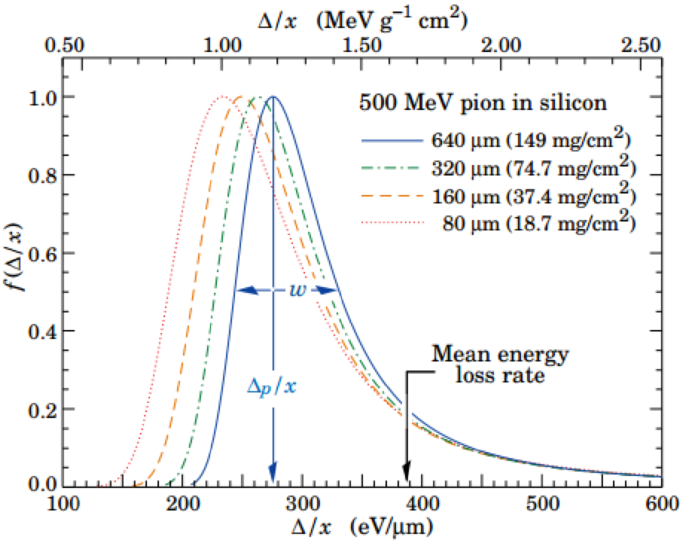

Figure 2.5: Straggling functions for 500 meV pions in silicon. The plot is taken from [4].

The large weight of rare collision events in which we encounter large energy deposits, drives the mean into the tail of the distribution. Thus the mean value of energy loss undergoes intense fluctuations. In the previous figure it is clearly visible that the most probable energy loss is only a fraction of the mean energy loss. For very thick absorbers the distribution is less skewed but never approaches a Gaussian.

For thin absorbers (like gas detectors) the Landau distribution fails to describe energy loss. Detectors are only measure the energy which is actually deposited in their active volume. Thus the energy loss detected by the detector may not be the same with the actual energy loss of the incident particle. An important factor in this phenomenon is the big range of δ-electrons which have sufficient energy to leave the sensitive volume of the detector.

In these situations it is of more practical interest to consider only that part of the energy loss with energy transfers E smaller than a given cut value E_{cut}. The Bethe-Bloch equation, representing here this *truncated energy loss*, takes the form:

$$-\left.\frac{dE}{dx}\right|_{E<E_{cut}} = Kz^2\frac{Z}{A}\frac{1}{\beta^2}\left[\frac{1}{2}\ln\frac{2m_ec^2\beta^2\gamma^2E_{cut}}{I^2} - \frac{\beta^2}{2}\left[1+\frac{E_{cut}}{E_{max}}\right] - \frac{\delta}{2}\right] \tag{2.7}$$

The above form as $E_{cut} \rightarrow E_{max}$ approaches the the normal Bethe-Bloch formula. Again here the density correction term δ controls the increase of $\beta\gamma$ and the $-dE/dx|_{E<E_{cut}}$ reaches the constant Fermi plateau.

2.4 Ionization yield

During its transition into a material, a charged particle undergoes energy loss through excitation and ionization, creating a number of ion-electron pairs on its path. These free electrons produced from this collision process, are called *primary electrons*. As mentioned in the previous sections, some of these electrons can get sufficient energy to produce an independent further ionization. The electrons coming from this *secondary ionization* are called *secondary electrons*. The free two previous ionization processes, when combined, give us the *total ionization*. The number of ion-electron pairs produced from the total ionization per unit length is given by:

$$n_T = \frac{\Delta E}{W} \tag{2.8}$$

where ΔE is the energy transfered to the detector material, W is the average energy required to produce one ion-electron pair and n_T is the total ionization. The above formula is valid only if the transferred energy is completely deposited in the sensitive volume of the detector.

Gas	Z	A	$\varrho\ [g/cm^3]$	$I_0\ [eV]$	$W\ [eV]$	n_p	n_T	$-dE/dx\ [keV\ cm^{-1}]$
H_2	2	2	8.99×10^{-55}	15.4	37	5.2	9.2	0.34
O_2	16	32	1.43×10^{-3}	12.2	31	22	73	2.26
He	2	2	1.178×10^{-4}	24.6	41	5.9	7.8	0.32
Ar	18	40	1.78×10^{-3}	15.8	26	29	94	2.44
Ne	10	20.2	9.00×10^{-4}	21.6	36	12	39	1.56
Xe	54	131.3	5.89×10^{-3}	21.1	22	44	307	6.76
CO_2	22	44	1.98×10^{-3}	13.7	33	34	91	3.01
CH_4	10	16	7.17×10^{-4}	13.1	28	16	53	1.48

Table 2.1: Properties of some gases at standard pressure and temperature for minimum-ionizing particles. Here presented is the atomic number Z, the mass number A, the density ϱ, the average effective ionization potential per electron I_0 , the average energy required to produce one ion-electron pair W,the energy loss $-dE/dx$, the the number of primary, n_p, and total, n_T, ionization produced electron-ion pairs per *cm*.

The ionization that it is caused by the charged particle is a clearly random process. The number of ionizing interactions for a given distance L, can be described by *Poisson distribution*:

$$P(L/\lambda, k) = \frac{(L/\lambda)^k}{k!} e^{-L/\lambda} \tag{2.9}$$

where k is the number of ionizing collisions and λ is the mean free path between two ionizing interactions given by:

$$\lambda = \frac{1}{N\sigma_1} \tag{2.10}$$

where σ_1 is the ionization cross-section per electron and N is the electron density.

2.5 Further Electromagnetic Interactions of Charged Particles

2.5.1 Multiple Scattering

Upon entering a medium the charged particle can be scattered by the Coulomb potentials of nuclei and electrons. As mentioned earlier, the collision between a charged particle and the nucleus will lead to a significant change of the charge particle's direction. Such radical shifts in the direction of a particle along its trajectory is called *multiple scattering* (or *direction straggling*). For small scattering angles, this change in angle is normally distributed around the average $\Theta = 0$. The root mean square (rms) of the scattering-angle distribution, of particle traversing a thickness L of material, is given by:

$$\sqrt{\langle\Theta^2\rangle} = \frac{Z}{Pc\beta}(20MeV)\sqrt{\frac{L}{X_0}} \tag{2.11}$$

where X_0 represents the radiation length. We have:

$$\frac{1}{X_0} \approx 4\alpha r_0^2 \frac{\rho N_A}{A_r} Z_{nucl}(1 + Z_{nucl}) \ln\left(\frac{183}{\sqrt[3]{Z_{nucl}}}\right) \tag{2.12}$$

The definitions of the symbols used in the previous two equations are listed below:

Θ: scattering angle relative to the incoming particle in radians
P: momentum of the incoming particle
X_0: radiation length of the material
N_A: Avogadro's number
α: fine structure constant ($\approx 1/137$)
r_0: classical electron radius ($2.82\ 10^{-15}$ m)

2.5.2 Bremsstrahlung

The acceleration of any charged particle is always followed by emission of electromagnetic radiation. More specifically, a high energetic charged particle will experience strong deviations from its trajectory, due to elastic collisions with the Coulomb potential of a nucleus. This collision is surely accompanied by emission of electromagnetic radiation (*bremsstrahlung*).

The energy loss through this precess can be described by [22]:

$$-\frac{dE}{dx} \approx 4\alpha N_A \frac{Z^2}{A} z^2 \left(\frac{1}{4\pi\epsilon_0} \cdot \frac{e^2}{mc^2}\right)^2 E\ \ln\frac{183}{Z^{1/3}} \tag{2.13}$$

where is the energy of the incident particle.

From the previous equation we can see that the energy loss is proportional to the charged particle's energy and inversely mass squared. Thus for the electrons, which have small mass, bremsstrahlung energy loss is an important factor for this kind of particles. The average energy loss of an electron due to bremsstrahlung radiation, with energy E, in a material of thickness dx, is given by:

$$\frac{dE}{dx} = -\frac{E}{X_0} \tag{2.14}$$

where X_0 is the radiation length.

The energy loss of an electron, due to bremsstrahlung, is proportional to its energy while the ionization energy loss varies logarithmically with the electron energy. The energy value at which these two rates are equal, is called *critical energy* E_c.

2.5.3 Cherenkov Radiation

When a charged particle travels in a medium faster than the speed of light in this medium (in a medium with optical index of refraction n, the velocity of light is c/n), an emission of electromagnetic radiation occurs. This emitted light is called *Cherenkov radiation*.

When a charged particle travels in a medium, its electric field will polarize the atoms along its track making them electric dipoles. After the particle has passed the medium turns back to its initial unpolarized state. This variation of polarization in the medium with time, produces an electromagnetic perturbation that propagates in space at the speed of light. In the case where the charge particle travels at a speed lower than the speed of light in the medium, the small electromagnetic perturbations produced by the polarization and depolarization of the medium, travel faster than the particle. At any point in space far from the path of the charged particle, these perturbations arrive randomly and cancel each other.

In the other hand, when the particle's velocity is greater than the phase velocity of light in the medium, the electromagnetic perturbations propagate less rapidly than the particle, forming a single wavefront behind it. This finite perturbation represents a wave propagating in the direction fixed by the speed of the particle and the speed of light in the medium. The above two situations are illustrated in Figure 2.6.

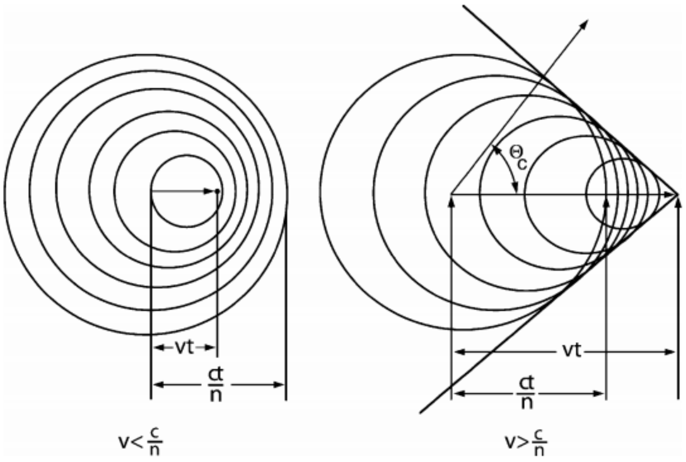

Figure 2.6: Left: The charged particle is traveling at speed larger than the velocity of light in the medium. Right: The charged particle id traveling at speed greater than the speed of light in the medium.

From the geometry depicted below, we can determine the angle between the particle and the electromagnetic wave. While the particle has traveled a distance ut ($= \beta ct$), the photon has progressed by $t \cdot c/n$. As result we have:

$$\cos\theta_c = \frac{t(c/n)}{ut} = \frac{c}{nu} = \frac{1}{n\beta} \tag{2.15}$$

2.6 Interactions of Electrons in Matter

At low energy the dominant energy loss mechanism for light particles, such as electrons, is due to inelastic collisions with the atomic electrons. The collision energy loss, which results in excitation and ionization of the material, must be modified since the mass of the incident particles is the same as the atomic electrons and in case of electrons the collision takes place between two identical particles. The electrons can undergo strong deviations from their trajectory in collisions, transferring a maximum energy of $E/2$ where E is the kinetic energy of the incident particle. Owing to the similar characteristics with the absorber's target electrons, a much larger fraction of the electron energy can be lost in a single encounter, thus it takes only few collisions to lose a significant amount of energy. Collision energy losses for electron are described by the Bethe-Bloch equation:

$$-\frac{dE}{dx} = 4\pi N_A r_e^2 m_e c^2 \frac{Z}{A} \cdot \frac{1}{\beta^2}\left[\ln\frac{\gamma m_e c^2 \beta\sqrt{\gamma-1}}{\sqrt{2}I} + \frac{1}{2}(1-\beta^2) - \frac{2\gamma-1}{2\gamma^2}\ln 2 + \frac{1}{16}\left(\frac{\gamma-1}{\gamma}\right)^2\right] \tag{2.16}$$

Unlike heavy charged particles, electrons at high energies undergo energy losses through radiation processes. As we mentioned earlier when electrons accelerate inside the Coulomb field of a nucleus, they emit electromagnetic radiation called bremsstrahlung. For heavy charged particles this contribution to energy loss can be ignored, as the probability for emitting bremsstrahlung is inversely proportional to the square of the incident particle's mass. The total energy loss of the electron is actually the sum of equation 2.13 and 2.16, namely the sum of the energy loss contributions due to collision and radiation processes.

The path of electrons in matter can be up to several centimeters and because it possess the same characteristics with the atomic electrons of the material, their energy loss rate is lower compared to heavier particles. As a result electrons follow a curled path through the medium. The distance traveled by an electron according to a straight line is usually much smaller than the actual length of the trajectory.

Now let us consider again the experimental setup described earlier in Section 2.2, but with the difference that now we have a monoernergetic beam of electrons. Now as we saw earlier electrons can undergo heavy scattering while traveling in a medium. The scattering greatly deviates the electron from its trajectory, with the possible result that the electron may travel a complex path in the material with some even scattering out of the material in the generally opposite direction from the direction of incidence.Figure 2.7 illustrates the curve that describes the number of the detected electrons as a function of the material thickness.

It is visible that the number of electrons penetrating the material starts to drop even though the thickness is much less than the range of the electrons. This is because of

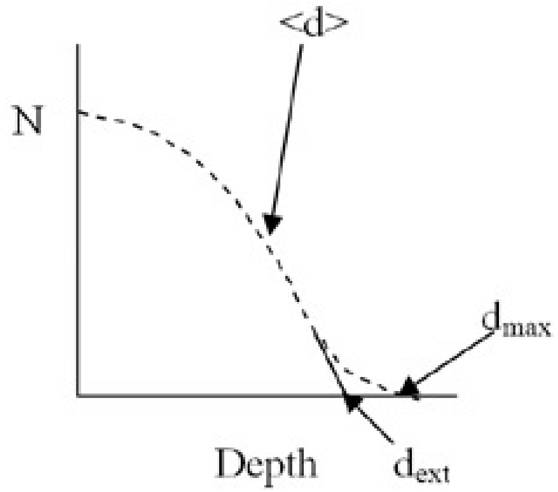

Figure 2.7: Number of electrons penetrating a medium as a function of its thickness.

the backscatter that takes place in the material, that subsequently reduces the number of electrons penetrating the material. As the thickness increases more, the number of electrons penetrating the material begins to decline more abruptly.

2.7 Interactions of Photons in Matter

2.7.1 Photoelectric Effect

During the photoelectric process, a photon is completely absorbed by an atomic electron. The energy of the photon can either excite the electron to a higher energy level in the atom, or completely remove it from the atom, making it a photoelectron. For gamma rays with enough large energy, the electron that is more likely to engage in a photoelectric process is the one belonging to K-shell, thus the most tightly bound electron. The energy of the photoelectron would be:

$$E_{kinetic} = hf - E_{binding} \tag{2.17}$$

where hf is the photon energy, $E_{binding}$ is the binding energy of the electron and $E_{kinetic}$ is the kinetic energy of the photoelectron. From the previous equation we can see that in order for the photoelectric interaction to be made, the energy of the photon must be greater than the electron binding energy.

The photoelectron, leaves behind it a vacancy in one of the atomic energy levels. This vacancy is quickly filled by an electron of a higher energy level and if the ejected electron belonged to the K-shell, an X-ray is emitted. This excess energy can be also appear as an Auger electron. In this process an electron from the outer shell fills the vacancy left by the extracted electron, and the released energy is transferred to an other electron of the outer shell, which then is ejected from the atom. The photoelectric effect is the dominant mechanism of interaction for gamma rays of energy less than 100 keV. This specific process is further enhanced for absorbers of large atomic number.

2.7.2 Compton Effect

Compton effect is the inelastic scattering of photons by quasi-free atomic electrons. During this process a fraction of the photon energy is transferred to the recoil electron. This interaction results in an ejected electron and a photon scattered at an angle θ. Figure 2.8 depicts the Compton scattering.

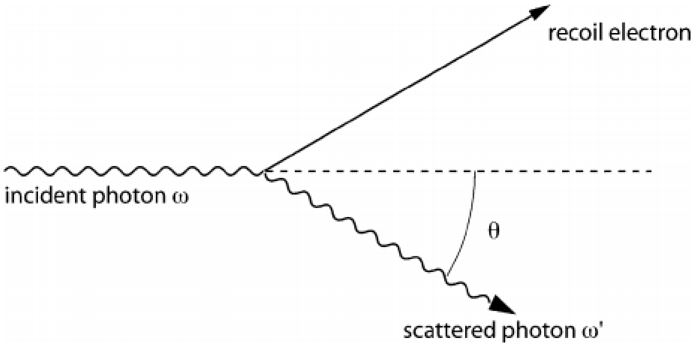

Figure 2.8: Illustration of Compton scattering. The scheme is taken from [3]

.

The relationship between the transfered energy and the scatter angle of the photon, for a Compton interaction, can be derive by using the energy and momentum conservation laws. Thus we have:

$$\hbar\omega' = \frac{\hbar\omega}{\left(1 + \frac{\hbar\omega}{m_e c^2}(1-\cos\theta)\right)} \tag{2.18}$$

where $\hbar\omega'$ is the transfered energy, $\hbar\omega$ is the photon's initial energy and $m_e c^2$ is the rest-mass energy of the electron ($\approx 0.511\ MeV$). The Compton scattering process is important for energy values of a few MeV.

For low gamma energies, there is a significant possibility that the recoil electron would not be ejected, but instead it would remain constrained in the atom after the collision. In this case the atom as a whole receives the energy transfered to the electron. This interaction is called *coherent Compton scattering* (or *Rayleigh scattering*). In the case where the Compton scattering results in an electron ejection, then we have the so called *incoherent Compton scattering.*

2.7.3 Pair Production

This interaction refers to the production of electron-positron pairs in the Coulomb field of a nucleus, which is possible only if the photon energy is greater than a specific threshold. This energy threshold is equal to the rest masses of two electrons plus the recoil energy which is transfered to the nucleus. Using energy and momentum conservation this threshold can be derived as:

$$E_\gamma \geq 2m_e c^2 + \frac{2m_e^2 c^2}{m_{nucleus}} \tag{2.19}$$

Because $m_{nucleus} \gg m_e$ the effective threshold is given by:

$$E_\gamma \geq 2m_e c^2 \tag{2.20}$$

For values larger than the 10 MeV, pair production becomes an important interaction mechanism of photons with matter.

The cross-section of the above described interactions as a function of the photon energy in carbon and lead, is illustrated in Figure 2.9.

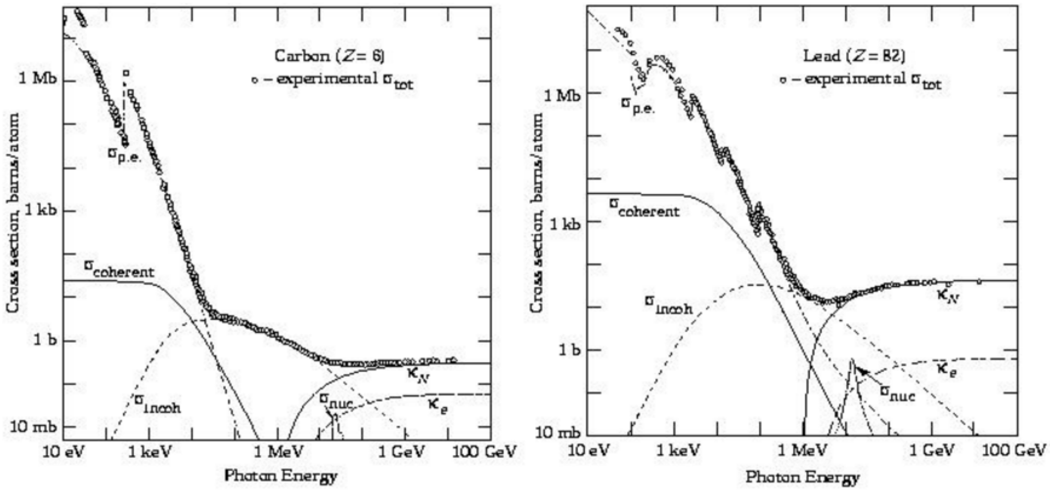

Figure 2.9: Total cross-section of photons as a function of energy in carbon and lead. p.e= atomic photoelectric effect, coherent= Rayleigh scattering, incoherent= Compton scattering, K_n and K_e is the pair production in nuclear and electric field respectively. The plots are taken from [4].

Chapter 3

Gaseous Detectors and Micromegas Technology

3.1 Drift of Electrons and Ions in Gases

When a charged particle passes through a gas-filled detector, it interacts with the gas atoms that are present and the whole process results in the production of ion-electron pairs. The localization of this ionizing products, generally after charge multiplication, is actually the main purpose of a gaseous detector. As a result the knowledge and comprehension of the phenomena concerning their motion inside the gas under the influence of the electric and magnetic field, is of great importance[1].

3.1.1 Drift of Electrons

The motion of electrons and positive charged ions id governed by electric fields $\boldsymbol{E}$ and magnetic fields $\boldsymbol{B}$. The motion of an electron of mass m can be described by the following equation which was introduced by P.Langevin:

$$m\frac{d\boldsymbol{u}}{dt} = e\boldsymbol{E} + e\left[\boldsymbol{u} \times \boldsymbol{B}\right] - K\boldsymbol{u} \tag{3.1}$$

where $\boldsymbol{u}$ is the velocity vector and K describes a frictional force proportional to $\boldsymbol{u}$ that is caused by the random collisions of the electron with the gas molecules. The ratio m/K has dimensions of time and represents the average time between these collisions. More specifically, we define:

$$\tau = \frac{m}{K} \tag{3.2}$$

where τ is the characteristic time.

Assuming a constant state where $du/dt = 0$ the drift velocity of the electron is given by [4]:

$$\boldsymbol{u_d} = \frac{e}{m} \cdot \frac{\tau}{1+\omega^2\tau^2}\left(\boldsymbol{E} + \frac{\omega\tau}{B}\left(\boldsymbol{E}\times\boldsymbol{B}\right) + \frac{\omega^2\tau^2}{B^2}\left(\boldsymbol{E}\cdot\boldsymbol{B}\right)\boldsymbol{B}\right) \tag{3.3}$$

where $\omega = eB/m$ is the *Larmor frequency.*

From Eq.(3.3) we can deduce some properties concerning the electron drift:

---

[1] For the writing of this chapter an extensive reading of the references [23], [3] and [21] was done.

- In the absence of a magnetic field ($\omega\tau = 0$) the direction of drift velocity is along the electric field lines and is given by the simple relationship:

$$\boldsymbol{u_d} = \frac{e}{m}\tau\boldsymbol{E} = \mu\boldsymbol{E}, \qquad \mu = \frac{e}{m}\tau \tag{3.4}$$

  Here μ is the scalar mobility defined as the ratio of drift velocity to applied electric field in the absence of the magnetic field. Also μ is proportional to the characteristic time τ and caries the charge sign of the particle.

- If the electric field $\boldsymbol{E}$ is perpendicular to the magnetic field $\boldsymbol{B}$ then $\boldsymbol{E} \cdot \boldsymbol{B} = 0$ and the term $\boldsymbol{E} \times \boldsymbol{B}$ defines a drift direction perpendicular to the fields where the net drift velocity vector covers the so called *Lorentz angle.*

- For large magnetic fields, where $\omega\tau \gg 1$, the drift velocity vector tends to be along the $\boldsymbol{B}$ field direction, as long as $\boldsymbol{E} \cdot \boldsymbol{B} \neq 0$.

Microscopic Picture

In the macroscopic scale the drift electrons are scattered gas molecules continuously and after each collision their motion is random. More specifically because of its small mass the electron scatters isotropically and immediately after the collision it has abandoned any preferential direction. A short time after the collision, the electron would have an instantaneous and randomly oriented velocity u_{inst} and an additional velocity u_d equal to its acceleration along the field, multiplied by the average time between two collisions. The expression that describes this additional velocity component is the same with Eq.(3.4), but with the difference that in this case τ represents the average free time between two collisions.

In the absence of an electric field an electron has a thermal energy of $(3/2)k_BT$. As a result, with an electric field present the total energy of a drifting electron can be described as:

$$\epsilon = \frac{1}{2}mu_{inst}^2 = \epsilon_E + \frac{3}{2}k_BT \tag{3.5}$$

where ϵ_E is the energy gained from the electric field.

If one considers the balance between the energy lost due to collisions and the energy acquired from the electric field, the drift and instantaneous velocity can be expressed as:

$$u_d^2 = \frac{eE}{mN\sigma}\sqrt{\frac{\lambda}{2}}, \tag{3.6}$$

$$u_{inst}^2 = \frac{eE}{mN\sigma}\sqrt{\frac{2}{\lambda}} \tag{3.7}$$

where N is the number density, λ is the fractional energy loss per collision and σ is the electron elastic scattering cross-section. Both λ and σ are functions of the electron energy ϵ. From the previous equations we can see that for small values of λ the drift velocity approaches zero.

3.2 Drift of Ions

Because of their much larger mass, the behavior of ions is different compared with that of the electrons. As we saw in the previous section, the momentum of an electron is randomized after a collision with a gas molecule and the electron energy is actually consisted of its thermal energy and the energy gained from the electric field. In the case of an ion however, a considerable portion of this additional energy component can be expended in the next collision, thus it makes only a small contribution to the randomness of the particle's motion. As a result, the random energy of the ions are mostly thermal and only a small fraction is due to the field.

For low field strength values the random drift velocity of the ion is mainly thermal and can be given by:

$$u_d = \left(\frac{1}{m} + \frac{1}{M}\right)^{1/2} \left(\frac{1}{3k_BT}\right)^{1/2} \frac{eE}{N\sigma} \tag{3.8}$$

where m is the mass of the drifting particle and M is the mass of the gas molecule. From the above equation it is observable that at the low field range the drift velocity is proportional to the field strength E.

In the case where the field strength is large the thermal component can be neglected, the drift velocity is described by:

$$u_d = \left[\frac{eE}{mN\sigma}\right]^{1/2} \left[\frac{m}{M}\left(1 + \frac{m}{M}\right)\right]^{1/2} \tag{3.9}$$

From Eq.3.9 it can be deduced that the drift velocity at high fields is proportional to the square root of the field strength. The next table contains some ion mobilities for low field measured in gases used in gaseous detectors.

Gas	Ion	Mobility $(cm^2V^{-1}s^{-1})$
He	He^+	10.40
Xe	Xe^+	0.57
Kr	Kr^+	0.96
Ar	Ar^+	1.535
Ar	$CO_2{}^+$	1.72
Ar	$CH_4{}^+$	1.87
CO_2	$CO_2{}^+$	1.09
CF_4	$C_2H_6{}^4$	1.04
CH_4	$CH_4{}^+$	2.26

Table 3.1: Experimental low-field mobilities for some gases used in gaseous detectors.

3.3 Diffusion

The electrons and ions produced due to ionization, experience strong deviations from their original trajectories because of their involvement to random collisions with the gas molecules. If we consider the simplest of cases where this deviation is the same in all directions, we could imagine a point-like cloud of electrons which begins to drift and after some time will follow a Gaussian density distribution:

$$n = \left(\frac{1}{\sqrt{4\pi Dt}}\right)^3 \cdot \exp\left(\frac{-r^2}{4Dt}\right) \tag{3.10}$$

where n is the charge corresponding to the position r after a time t and D is the *diffusion coefficient.*

Eq.(3.10) presents a standard deviation of $\sigma = 2Dt$ for a two-dimension motion and a $\sigma = 6Dt$ in the case of three-dimension motion. Under the influence of the electric field the charged particles move with an average drift velocity u_d. The diffusion coefficient is related to the particle's mobility through the *Nernst-Townsend formula* or*Einstein formula*:

$$\frac{D}{\mu} = \frac{k_B T}{e} \tag{3.11}$$

For electron and ions which have thermal energy of $(3/2)k_B T$ the variance of Eq.(3.10) becomes:

$$\sigma^2 = 2Dt = \frac{2DL}{\mu E} = \frac{4\epsilon L}{3eE} \Rightarrow \sigma = \sqrt{\frac{2k_B TL}{eE}} \tag{3.12}$$

where L is the distance traveled by the particle and T is the room temperature.

3.4 Avalanche Formation

After the creation of the ion-electron pairs, the electrons coming from the ionization processes drift under the influence of an electric field towards the anode. Once an electron is close to a region of a strong electric field, it can get sufficient energy between two collisions with the gas molecules, enabling it to produce further ionization in the gas. Electrons produced by this process could cause even further ionization. The whole process leads eventually to the so called *Townsend avalanche.* This avalanche has drop-shaped form as can be seen in Figure 3.1. The electrons move much faster than the ions, thus they distributed on the head of the drop, leaving behind a cloud of positive ions which travel slowly towards the cathode.

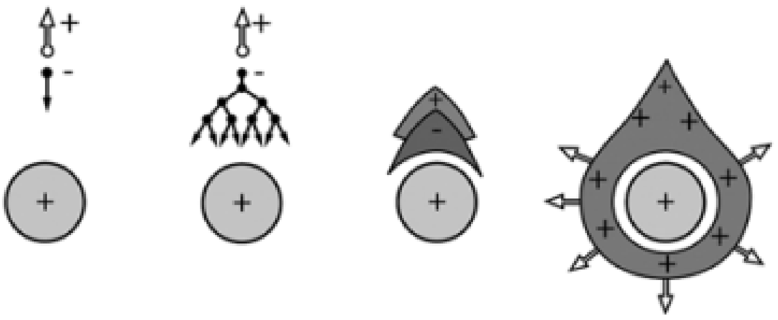

Figure 3.1: Time development of an avalanche in a proportional counter.

The probability for a primary electron, originating from the ionization processes before the avalanche formation, to produce an additional electron in an infinitesimal path length

dx is αdx where the quantity α is called the *first Townsend coefficient* and is equal to the inverse of the electron mean free path. Suppose that n is the number of charges as a function of the distance traveled by an electron in a constant electric field. After some distance a primary electron, will give rise to dn electrons. Thus we have:

$$\frac{dn(x)}{dx} = n(x)\alpha \tag{3.13}$$

For a given electron population corresponding to $x = 0$, the total number of secondary electron-ion pairs is then given by:

$$n = n_0 e^{ax} \tag{3.14}$$

where we can see that the charge increases exponentially. The ratio $G = n/n_0$ represent the so called *gain* or *multiplication factor*. In general, for a non-uniform electric field the first Townsend coefficient is a function of distance x so the previous expression becomes:

$$n(x) = n_0 e^{\int \alpha(x)dx} \tag{3.15}$$

The previous mechanism is valid only for moderate gain values. If the gain is too large it will lead to the creation of space charge formed as a cloud of charges, which will distort the electric field. This modification of the electric field will also change the first Townsend coefficient. The physical limiting value of the multiplication factor is called *Raether limit*. If the gas gain is greater than a value of about 10^8 the multiplication process stops and a discharge takes place.

In addition to the direct creation of secondary ionization from the primary electrons, there are also other effects able to provoke a multiplication process. In some gas mixtures the energy excess in a molecule's excited state, can be higher than the the ionization potential of the mixture and produce further ionization, a process which called *Penning effect*. Moreover during multiplication some electrons with sufficient amount of energy, can bring some molecules in an excited state without further ionizing them. The excited molecules are then decay to their ground state through the emission of visible or ultraviolet photons. These photons could create secondary ionization in the gas.

The above described secondary mechanisms of ionization, can lead to large values of gas gain. In order to keep the gain value below the Raether limit an additional poly-atomic gas is usually used which contains the photon-induced effects by mainly absorbing them. These type of gases are called *quench gases*.

3.5 Signal Formation

The motion of ion-electron pairs created during an avalanche, induce signals in the readout electrodes of the detector. Under the influence of a constant electric field the electrons and ions are separated and drift towards the anode and cathode respectively. Because of their much larger speed than the positive ions, electron reach the cathode in about 1 ns leaving the positive ions behind and creating very quick pulses. The positive ions in the other hand, need several hundred nanoseconds in order to reach the cathode and their motion induce charge in the electrodes. Actually it is this motion of positive ions that contribute the most to the total signal. [2]

---

[2] The total induced signal consists of a fast part corresponding to the electrons while the slow positive ions actually determine the evolution of the signal which has a long tail of several hundreds of nanoseconds.

In order to calculate the current induced to one particular electrode the *Shockley-Ramo theorem* is used. According to this theorem, in the case of a charge q moving with a drift velocity u_d the instantaneous current induced at a given electron will be:

$$I_n(t) = -\frac{q}{V_n}\boldsymbol{E_w u_d} \tag{3.16}$$

where $I_n(t)$ is the current induced in electrode n, bmu_d is the drift velocity of the charged particle while bmE_w is the electric field when the charge q is removed, electrode n is set to V_n and all the other electrodes are grounded.

3.6 Proportional Counters

Gas detectors are able to operate in different modes related to the size of the applied voltage. Figure 3.2 illustrates the signal amplitude as a function of the external applied voltage where the different operation regimes for a gas detector can also be seen.

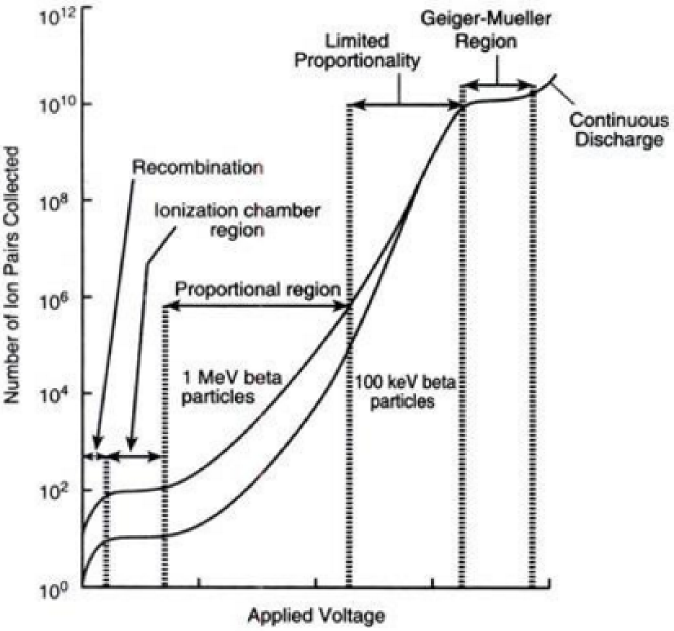

Figure 3.2: The different operation regimes of gaseous detectors with respect to the external applied voltage.

At the very low voltage region, the so called *recombination region,* the electric field lacks the power to effectively separate the ions and electrons produced from the ionization processes, allowing them to drift slowly towards their respective electrodes and eventually recombine back to neutral molecules before they can be collected. By increasing the applied voltage the recombination effect is suppressed and most of the ionization products can be collected. This is the *ionization region* and is the the normal operation mode of ionization chambers. In the *proportional region* that follows, the further increase in voltage triggers the appearance of multiplication processes. The electrons produced in ionization gain sufficient energy enabling them to produce secondary ionizations resulting to charge multiplication. As we can see in the previous picture the collected charge increases almost linearly with respect to the applied voltage. As the applied voltage increases more, this linear relationship starts to dissolve leading to a non-linear proportionality that indicates the *limited proportionality region.* In this region the very fast collection of the electrons compared to that of the positive ions, allows the creation of space charges which distort the electric field. By increasing even further the applied voltage this space charge effect becomes dominant and no further multiplication takes place resulting in a constant number of collected electron-ion pairs. This is the so called *Geiger-Müller region.* Further increase in the field results to the dominance of discharges.

3.6.1 Multi-Wire Proportional Chamber

The *Multi-Wire Proportional Chamber (MWPC)* was invented by Georges Charpak in 1962 and revolutionized the concept of gaseous detectors. This invention gave Charpak the Nobel Prize in Physics in 1992. The detector, illustrated in Figure 3.3 consists of two conductive cathodes planes which have in the middle of the distance between them, a set of parallel, evenly spaced wires.

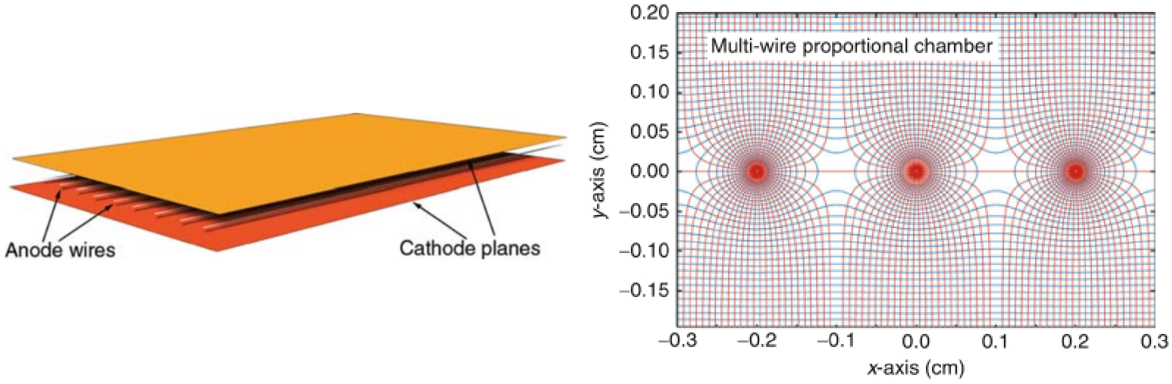

Figure 3.3: Left: Schematic view of a MWPC chamber. Right: Electric field lines and equipotential lines in a multiwire proportional chamber.

An almost uniform electric field is created throughout the detector by applying a potential difference between the anode wires and the cathodes. Close to the wires the field is intense thus able to produce charge multiplication. A charged particle traversing the chamber will generate electron-ion pairs through ionization processes. The liberated electrons drift under the influence of the electric field towards the anode electrodes where close to them is the high field region. As a result when the electrons approach the vicinity of the electrodes an avalanche multiplication takes place. When an avalanche occurs near a wire a negative signal will be induced in this particular wire and a positive signal in the neighboring wires. This positive signal will counterbalance the negative signal induced in the same wires by capacitance coupling between them. As a result a strong signal is induced on the wire where the avalanche is formed.

Each wire equipped with its own readout electronics, serves as a separate counter providing position information in one direction. The positive signals induced to the cathode plane, can be used to obtain a two-coordinate track information with a single chamber. This is achieved by using a printed circuit board with a strip pattern orientated perpendicularly to the anode wires. By exploiting the multiple ionization and implementing a charge interpolation (center of gravity (COG) or centroid method) a sub-millimeter spatial resolution can be obtained (~50 μm for tracks perpendicular to the wire plane).

Despite their good performance MWPC is characterized by a number of significant deficiencies concerning mechanical deformations due to strong electrostatic forces, space charge effects that affect the gain and the performance of the detector, due to the slow drift of positive ions which generates an intense distortion of the external electric field, and ageing effects which also harm the overall efficiency and performance of the detector. These issues triggered the development of a new technology of gaseous detectors, the so-called *Micro-Pattern Gaseous Detectors (MPGD).*

3.7 Micro-Pattern Gaseous Detectors (MPGD)

The implementation of microelectronics techniques for the manufacturing of gaseous detectors, suggested by A.Oed, has made their development and manufacturing much easier triggering the invention of a number of gaseous detectors like GEM and MICROMEGAS. These detector technologies are called *micro-pattern gaseous detectors*. They are high granularity gaseous detectors with sub-millimeter distances between the anode and the cathode electrodes.

The radical changes in size limitations that the modern lithographic technology brought, provide these detectors excellent detecting abilities. More specifically the use of very small pitch size of a few hundreds of microns, greatly enhances the detector's granularity thus leading to excellent spatial and time resolution as well as great counting rate capabilities.

3.7.1 Micro-Strip Gas Chamber (MSGC)

The first important step towards a micro-structure gas chamber was made with the introduction of *Micro-Strip Gas Chamber* (MSGC) in 1985. The detector consisted of a set of parallel metal strips alternative connected as anodes and cathodes, deposited by a lithographic method on a dielectric supporting structure. Figure 3.4 illustrates a schematic of the MSGC as well as the equipotential and field lines for the same detector.

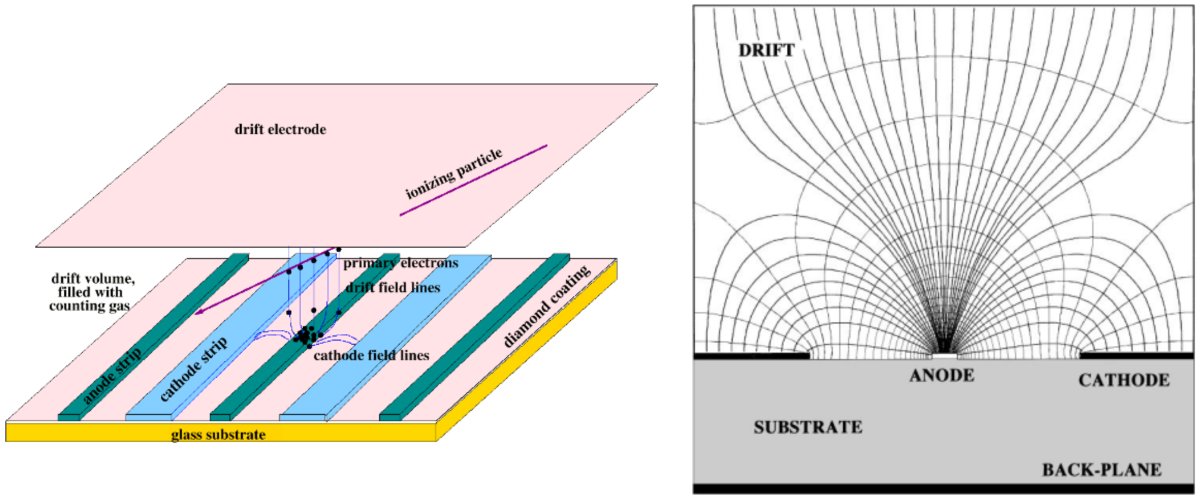

Figure 3.4: Left: Schematic view of a MSGC chamber. Right: Equipotential and field lines in the MSGC.

The typical pitch for the anode and cathode strips is about 200-400 μm while the small thickness of the anode stripes, approximately 7-20 μm, guarantees the development of a strong electric field in the proximity of the electrode. The most crucial part of the detector is the so-called *substrate* which carries the electrodes (or strips) on top of it. The most widely preferable material for the substrate is glass while the glass plates have a typical thickness of 300 µm.

The primary electrons produced due to ionization processes in the volume between the drift electrode and the anode-plane, drift toward the anode strips and near them a Townsend avalanche takes place. The small cathode-to-anode distance, which is about 100 µm, enables the fast evacuation of the positive ions, thus suppressing space charge effects.

The great sensitivity of MSGCs to sparks produced by heavy ionizing particles, due to their fragile electrode structure, made them unstable and ineffective despite their initial promising performance. Thus a need for more effective technologies emerged, setting up the development of detectors like GEM and MICROMEGAS.

3.7.2 Gas Electron Multiplier (GEM)

In order to overcome the issues confronted in the MSGCs, due to the exposition of their fragile electrode structure to high electric fields, Fabio Sauli in 1997 introduced the *Gas Electron Multiplier* a schematic view of which is illustrated in Figure 3.5.

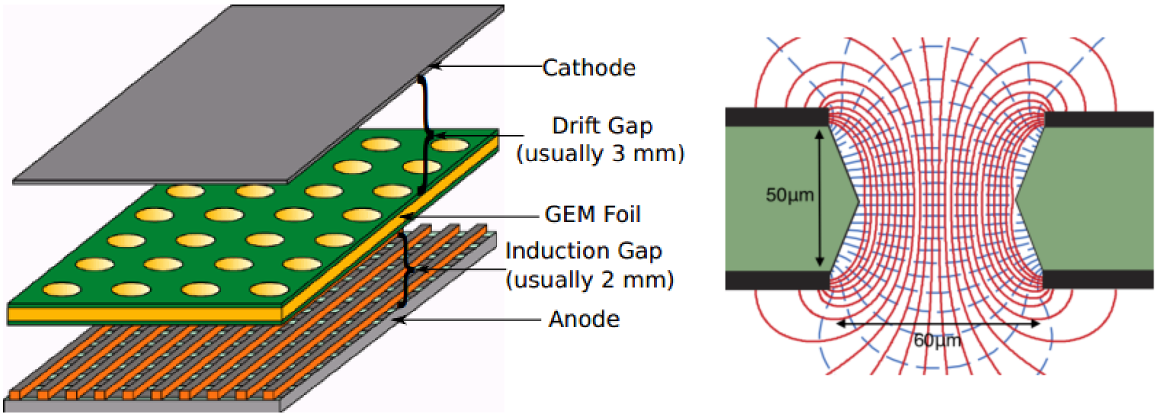

Figure 3.5: Left: Schematic view of a GEM chamber. Right: Equipotential and field lines in the GEM's holes.

A GEM chamber [24] consists of a thin polymer foil (thickness of about 50 μm) which is copper-coated on both sides and punctured by a high density of holes with a diameter typically 25-100 μm and the distance between them varying from 50 μm to 200 μm. The GEM foil is placed between a drift and a charge collection electrode.

With the application of a large potential difference between the two sides of the GEM foil, a high electric field is developed in the holes, as shown in the right part of Figure 3.5, making them amplification regions. Under the influence of this field the primary electrons created in the drift gap (the gap between the cathode and the GEM electrode) drift towards the holes and due to the intensity of the field, acquire sufficient energy to trigger charge multiplication. A significant amount of the electrons created during the avalanches, are then leave the multiplication area and travel into the lower part of the chamber inducing pulses on the readout elements of the anode electrode.

The placing of a sequence of GEM sheets leads to the the creation of a multi-layer GEM detector. In this set-up the pre-amplification and transfer process enables high proportional gains without the occurrence of discharges. GEM detectors will be part of the first endcap station of the CMS muon system as they have been identified as a technology capable to operate in the high radiation environment presentment in that region.

3.8 MICROMEsh GAseous Structure

The concept of Micromegas detector was first introduced in the middle of nineties by I. Giomatris and G. Charpak [25]. It is a MPGD the main feature of which is its two very asymmetric regions. The detector consists of a planar (drift) electrode, a gas gap of a few millimeters thickness representing a drift and conversion region, and a thin metallic mess at typically 100-150 μm distance from the readout electrode, forming an area which acts as an amplification region [26]. The mesh is supported by a number of cylindrical spacers (pillars), made of insulating material with a pitch of a few mm, which determine the thickness of the amplification region. Figure 3.6 illustrates the geometry and the operating principle of a Micromegas chamber.

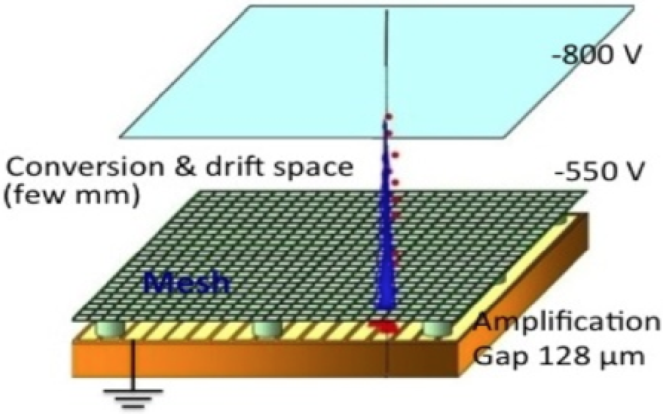

Figure 3.6: Schematic view of the typical Micromegas detector components.

The initial design of the detector has both the drift and mesh electrode at negative high potential (HV) while the readout electrode is at ground potential. The configuration of the applied voltages leads to an electric field of a few hundred V/cm in the drift region while the electric field in the amplification region is about $40 - 50$ kV attaining gain values of the order of 10^4.

The operation of the MM detector is based on the ionizations produced by a charged particle traversing the drift region. The electrons produced by ionization processes, drift under the influence of the applied electric field towards the mesh which is transparent to more than 95% of the electrons as long as the electric field in the amplification gap is 50-100 times stronger than the drift field. An electron multiplication takes place in the thin amplification region and the electron cloud is finally collected by the anode electrode within 1 ns resulting in a fast pulse on the readout strip. The positive charged ions in the other hand, drift slowly towards the mesh with drift velocities approximately 200 times lower than the electrons, thus they need a much larger amount of time, about 100 ns, to reach the mesh. This fast evacuation of the positive charged ions is a very important feature of the MM detector, enabling it to operate at very high particle fluxes.

3.8.1 Bulk Micromegas

The need of large-area robust detector technologies with low-cost construction requirements, led to the improvement and simplification of the manufacturing techniques concerning the MM detector. A novel technique to manufacture the MM structure called *bulk* has introduced in 2006 [5]. The technique makes use of the Printed Circuit Board technology to produce the entire sensitive detector from the anode plane up to the mesh.

The first important step is the replacement of the usual electroformed micromesh with a woven wire mesh. Their existence in large rolls, the low cost, their production by several countries around the world as well as the endurance they demonstrate in stretching and handling, are some of the advantages that these kind of meshes present.

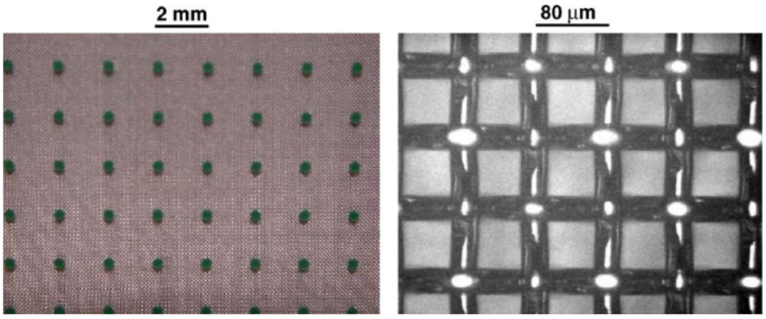

Figure 3.7: Left: The cylindrical pillars with diameter of 300 μm and pitch of 2 mm [5].

At the the fabrication process a photoresistive film (Vacrel) is laminated on top of a PCB and pre-streched mesh made of stainless steel is deposited on it. An additional photoresistive layer is then laminated on the top of the mesh. The photoresistive material is subsequently etched by a photolithographic method, producing the pillars. The pillars have a cylindrical shape of 300 μm diameter as illustrated in Figure 3.7

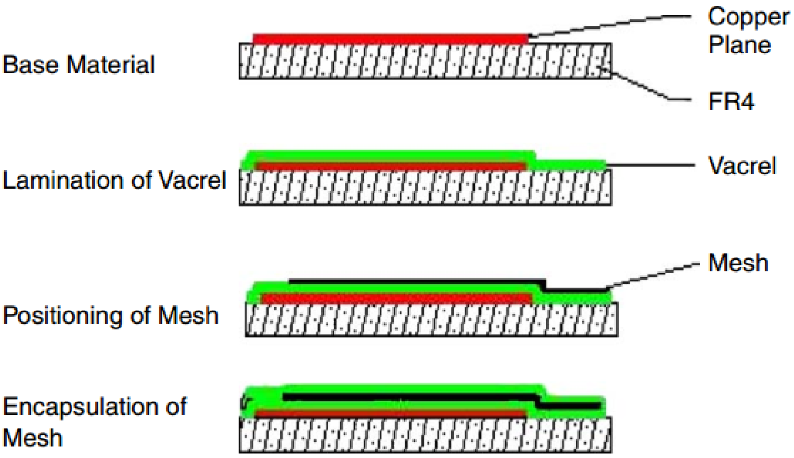

Figure 3.8: Fabrication steps of the bulk MM [5].

3.8.2 Resistive Micromegas

The quick evacuation of the ions due to the small amplification region suppresses space charge effects enabling the MM detectors to deal with high particle fluxes. However, the specific properties of MM chambers, with a very thin amplification region, make them particularly vulnerable to sparking. Sparks occur when the number of electrons in the avalanche reaches the Raether limit (10^7-10^8 electrons per avalanche). Since the detection of minimum ionizing muons demands gas amplification factors of the order of 10^4, ionization processes producing more than 1000 electrons per mm imply the risk of sparking. Sparks cause discharges corresponding to breakdowns of the applied voltage with long recovery times, thus disturbing the detector's operation. Heavy ionizations produced by α-particles or other slow-moving particles can cause catastrophic damages to the detector's elements and readout electronics.

For the solution of this important issue the concept of *resistive micromegas* [27] has been developed illustrated in Figure 3.9. The basic idea was to enhance the bulk micromegas with an additional layer (50-70 μm thick) of insulator (photoimageable coverlay or Kapton) on top of which strips of resistive paste (with a resistivity of a few MΩ/cm) are deposited. The innovative step lies in the fact that instead of using a continuous resistive layer, a resistive strips layout was chosen where the resistive strips match the pattern of the readout strips. This choice was made to avoid charge sharing across several readout strips and to keep the area affected by a discharge as small as possible. The signals from the ion-electron movement are induced first on the resistive strips and then to the readout strip through capacitive coupling.

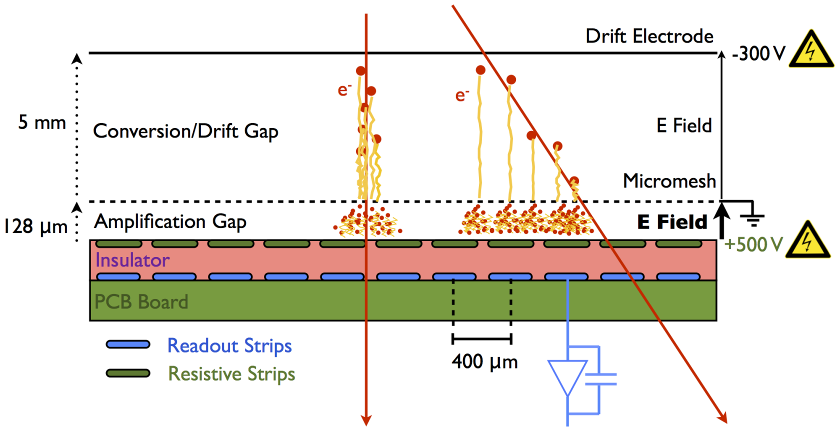

Figure 3.9: Schematic representation of a resistive micromegas detector.

Figure 3.10 illustrates the performance of a spark resistance micromegas compared with that of a standard micromegas detector, with both detectors exposed to a beam of 5.5 MeV neutro with a flux of 10^6 Hz/cm^2 [3]. Both chambers were operated with the same readout electronics and gas mixture (Ar+CO$_2$). The difference in the measured current amplitudes and voltage drop highlights the tolerability of the resistive micromegas to sparks.

---

[3] The discussion and detailed results concerning this work are presented in [6]

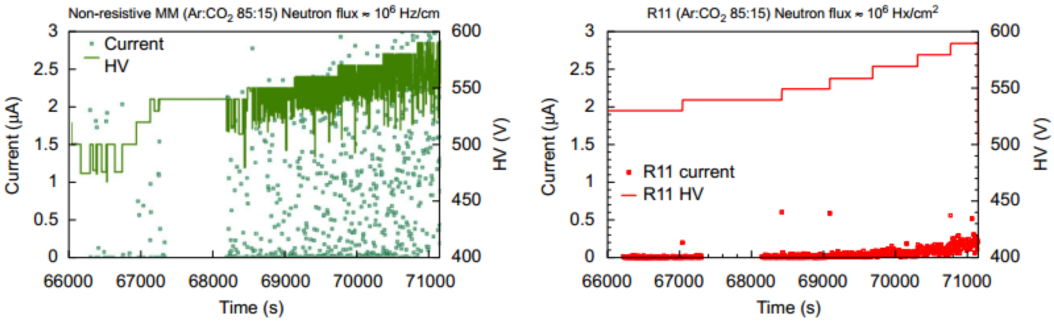

Figure 3.10: Supplied voltage drop in case of sparks for a non-resistive (left) and a resistive micromegas detector (right). The plots are taken from [6].

3.8.3 Resistive Micromegas with Two-Dimensional Readout

It is possible to implement the resistive stips idea to micromegas detectors with two-dimensional (or in generall multi-dimensional) readout structure as can be seen in Figure 3.11. In contrast to conventional micromegas detectors this layout features two independent readout electrodes oriented perpendicularly with each other and printed on the same PCB.

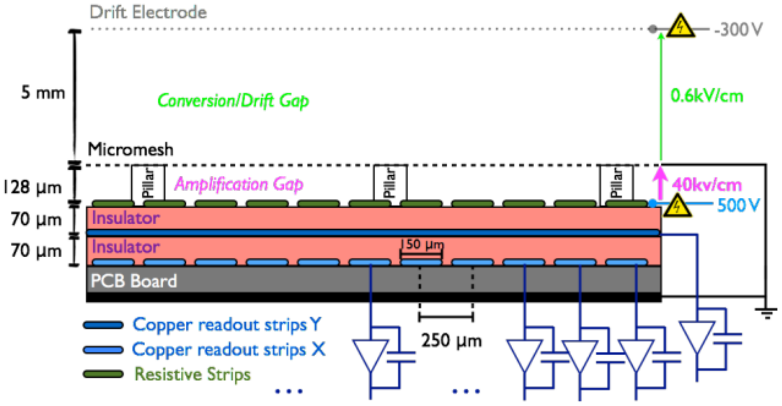

Figure 3.11: Schematic cut-view of a resistive micromegas with a two-dimensional readout structure.

More specifically the second layer of readout strips, the so-called Y-layer, consists of copper strips 80 μm wide and printed with a pitch of 250 μm. The strips of the X-layer in the other hand, demonstrate the same pitch but their width is 150 μm. The larger width of the X-layer strips compensates for the weak capacitance coupling to the strips of the X-layer due to their larger distance to the resistive strips. The two layers are separated by a 70 μm layer of insulating FR4 material.

A study concerning the signal characteristics for the two separate readout layers can be found in [28]. Furthermore a multidimensional resistive MM concept featuring more than two readout layers is presented in [29]. The multidimensional readout concept introduced significant difficulties in the construction procedure and eventually was rejected in favor of a layout with separate detection layers slightly rotated by a small stereo angle.

The resistive Micromegas with two-dimensional readouts structure (Tmm-type) is the main subject of the present work. The data analysis and results discussed in the next chapter are entirely related to this kind of bulk resistive MM detectors, with the aim to highlight some of their intrinsic operation characteristics and limitations.

3.9 The Micromegas Modules for the ATLAS NSW

The Micromegas is one of the detector technologies that has been chosen for tracking and trigger purposes for the upgrade of the forward muon detectors of the ATLAS experiment derived from the LHC luminosity increase. Their ability to cope with high rate conditions while preserving their performance characteristics, made the resistive-stip type Micromegas a clear choice for the purposes of the NSW upgrade [4].

The layout of the Micromegas detectors is arranged in small and large sectors as shown in Figure 3.12 where the different dimensions of the different MM modules is also illustrated. The dimensions of the sectors are chosen that approximately the same azimuthal overlap of the active areas is achieved. Each sector comprises eight MM detection layers, grouped into two multiplets of four layers (quadruplets) each separated by some distance. For the two wheels, one on each end-cap side of the Muon Spectrometer, the total number of Micromegas quadruples to build is 128, for a total active area of 1200 m^2 detector planes. The detectors will be operated at a gain of 10^4.

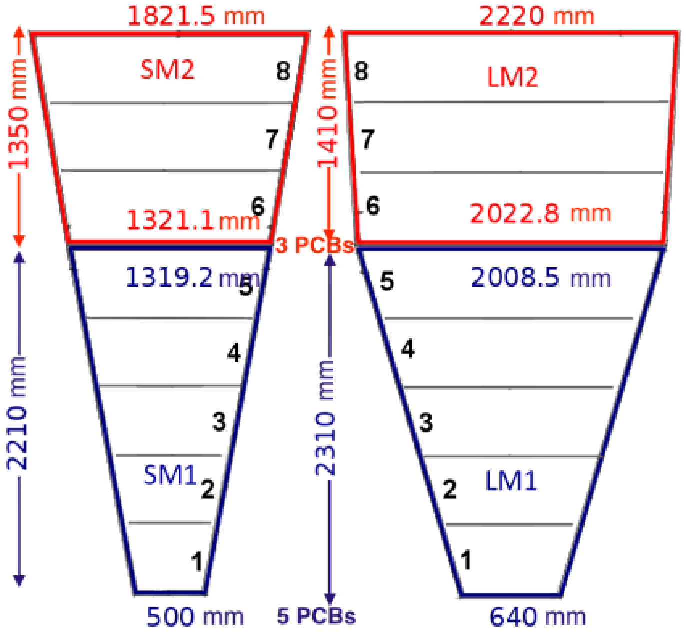

Figure 3.12: Dimensions of the small and large NSW Micromegas sectors.

The strip width will be 300 ± 20 µm for all the modules with a pitch of 425 ± 20 µm for small an large sectors respectively. This configuration will lead in a system of 2.1 M channels. Strips on the four out of eight layers will be under an angle of ±1.5° providing a second coordinate measurement while the contribute to the precision coordinate measurement with the other four at the same time.

---

[4] The New Small Wheel (NSW) will replace the current Small Wheel of the ATLAS Muon Spectrometer in the LHC Long Shutdown in 2018/2019

3.9.1 Large Area Resistive Micromegas Detectors

Despite its great efficiency the bulk manufacturing technique of MM chambers demonstrates inefficiencies when applied in large scales. The main reason is the risk of enclosing some impurities under the mesh, which eventually will harm the normal operation of the detector.

In order to avoid this kind o issues a new construction scheme was developed for the NSW MM detectors. The mesh in this case is no longer merged with the anode PCB, but instead is embodied to the drift panel as shown in Figure 3.13. The mesh is glued to 5 mm high frame, fixed in the drift electrode. When the the chamber is finally closed the mesh is in a distance of 128 μm from the readout plane while the the electrostatic force between the mesh and the resistive strips due to the applied voltage to the resistive strips, ensure the good contact between the mesh and the pillars. This assembly technique, often called as *mechanically floating mesh*, has the important advantage of enabling the safe removal of the mesh, in order for the underneath region to be cleaned.

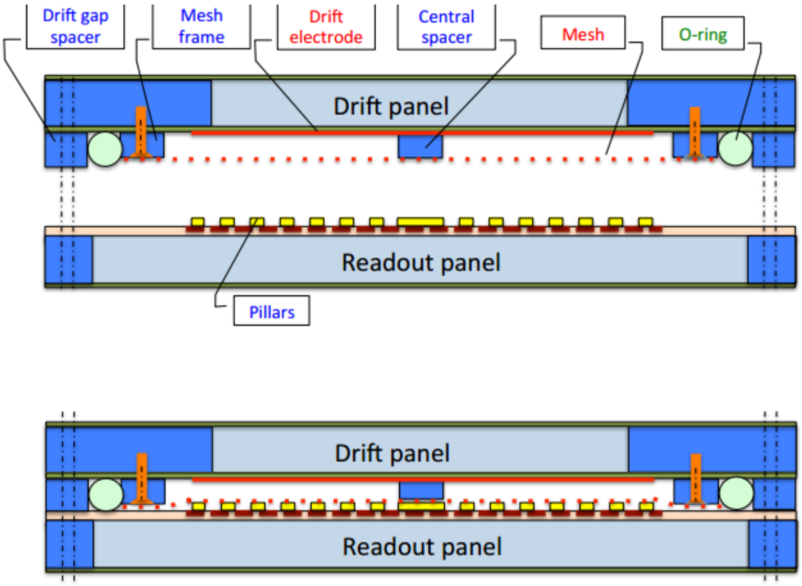

Figure 3.13: The *mechanically floating mesh* assembly process. The picture is taken from [7].

Chapter 4

Data Analysis and Results

4.1 Introduction

The main purpose of this thesis is the estimation of the spatial resolution concerning resistive MM chambers with a two-dimensional readout system[1], by using the measured time information from the readout Y-strips. This result is compared to the spatial resolution extracted by using the charge centroid method in order to better understand the performance limitations and operating characteristics of these type of MM detectors. In the following sections we describe the development of a hit reconstruction method which is implemented specifically to the time distribution for a cluster of Y-strips. Furthermore, a few results derived from this specific method are also presented[2].

4.2 Strip Time Information

The intrinsic performance of any gaseous detector type is determined by the gas mixture and the gap size that are used for the detection of the charged particles. The timing measurement of a MM detector (and more generally of a MPGD) is governed by statistical fluctuations of the induced signal and depends on the arrival time of the earliest primary cluster in readout channel. Furthermore the gain value poses a significant factor as a certain level of amplification is needed in order for the detector to be able to measure a single primary cluster.

In addition to these statistical phenomena the front-end electronics play a key role in the time measurement, as their technical characteristics, such as the shaping time of the amplifier and the timing resolution of the chip, define the accuracy with which the measurement is made. The Tmm chambers, the data of which were used for our calculations, were operated with Ar+7%CO_2 gas mixture and readout using APV25 [31] front-end hybrid card via the SRS [32] system.

A typical APV25 raw signal on one electronic channel, sampled per time slice over the full sampling phase of the APV25, is illustrated in Figure 4.1. The duration of each sample corresponds to 25 ns. By reading out 18 consecutive charge values (the APV25 provides

---

[1] From this point on we will refer to this type of resistive MM detector as Tmm.

[2] The data used for the acquisition of our results originate from the experimental work carried out during the test beam at the H6 beam line of the CERN SPS/H6 area on November 2015. A full description of the ATLAS Micromegas apparatus along with the specifications of the MM chambers that were used in the beam tests, can be found in Appendix B of [30]

only charge measurements) with a temporal spacing of 25 ns, the signal evolution can be investigated.

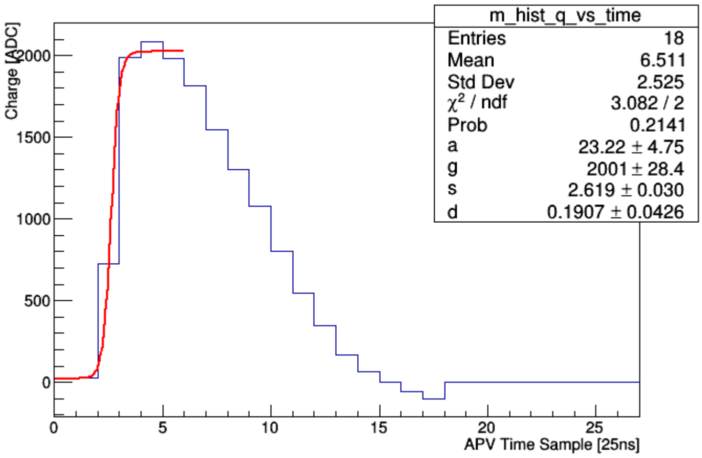

Figure 4.1: Charge measurement for one APV25 channel. The APV25 is configured to run with 18 samples. The pulse is fitted in its rising part with a Fermi-Dirac function for the extraction of the strip time measurement.

In order to extract the drift time information, the rising part of the strip pulse is fitted with a Fermi-Dirac function:

$$FD(x) = p_0 + \frac{p_1}{1 + e^{-(x-p_2)/p_3}} \tag{4.1}$$

where p_0 represents the barely fluctuating baseline before the signal, p_1 is the maximum pulse height, p_2 is the point of inflection of the rising edge (Fermi-Dirac time or t_{FD}) while p_3 is a parameter describing the signal rising time. The Fermi-Dirac inflection point is defined as the drift time measured by this readout channel. The measured time is actually the sum of the drift time and the time it takes for an avalanche to be formed. For a MM chamber with an amplification gap of 128 μm, the avalanche formation happens within approximately 1 ns, resulting in a quick pulse of electrons on the readout strip, while the drift of the primary electrons in the conversion gap is a relatively slow process with a duration of tens of ns. This is the reason why this fitting method focuses on the rising part of the strip's integrated charge distribution[3].

Alternatively the time bin where the maximum height of the pulse is encountered, can be used as strip time information. This measurement however is imprecise because of the 25 ns time window with which the APV25 hybrid measures the pulse. In the following section we make use of both of these strip time informations. The time bins were used in our initial analysis steps in order to have a first look at some of the characteristics regarding the Tmm chambers. The majority of our calculations however employ the Fermi-Dirac times as they constitute the experimental value of strip time.

---

[3] An enlightening presentation along with some refinement processes concerning this method can be found in the fourth chapter of [30]. In the same chapter an extensive study of the MM timing performance is also presented.

4.3 Spatial Resolution Studies

For the spatial resolution studies presented in this section, the data from a pair of Tmm chambers (Tmm2 and Tmm6) mounted back-to-back were used. The chambers were illuminated by a 120 GeV/c beam of pions and were positioned with their readout planes vertical with respect to the beam.

4.3.1 The Centroid Method

In the case of tracks perpendicular to the detector plane, the *centroid method* has been proven to provide a very accurate hit reconstruction in the absence of a magnetic field. This is because the incident particle induces signal to only few strips per event. According to this method the cluster position P (or hit) is estimated by weighting the position of each strip with its signal amplitude and taking the average. Hence we have:

$$P = \frac{\sum_{i=1}^{n} x_i q_i}{\sum_{i=1}^{n} q_i} \tag{4.2}$$

where the x_i and q_i denotes the position and the pulse-height of the ith strip. The centroid method looses precision for increasing incident angles where the cluster size is also increased since the charge spreads out over more strips, and the cluster position is less localized.

However, in the event where the tracks are inclined, there is an increased possibility that the signal of each strip originates from the drifting of a single primary cluster permitting a precise measurement of its drift time. This accurate drift time information along with the strip address and drift velocity allows for a two-dimensional reconstruction of incident particle's track in the chamber which is called *μTPC track*.

4.3.2 Spatial Resolution with Charge Centroids

For the estimation of the spatial resolution events measured simultaneously by both Tmm chambers were selected. The spatial resolution achieved with the Y-strip layer, is estimated by comparing the hit positions, calculated with the centroid method, in the two chambers. Assuming that both chambers demonstrate the same spatial resolution since they have the same technical characteristics, the combined spatial resolution will given by:

$$\sigma(X) = \frac{\sigma(X_6 - X_2)}{\sqrt{2}}, \tag{4.3}$$

where $\sigma(X_6 - X_2)$ is the convolution of the spatial resolution of the two chambers, while X_6 and X_2 represent the hit positions for Tmm6 and Tmm2 chamber respectively. The distribution of the hit position difference divided by $\sqrt{2}$ is illustrated in Figure 4.2. It is fitted with a double Gaussian function to take into account also the tails. A single plane spatial resolution (σ of the core Gaussian) of 64 µm is measured for the Y readout strips. The result is obtained selecting single cluster events and applying cuts on cluster width ($>$ 3 strips) and strip charge (>60 ADC) ranges. The above measured value demonstrate the excellent spatial resolution capabilities of a resistive MM detector.

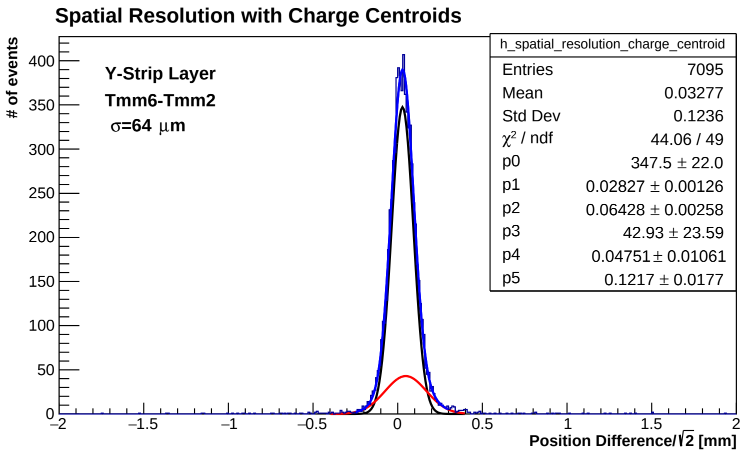

Figure 4.2: Distribution of the hit position difference divided by $\sqrt{2}$ between two Tmm chambers.

4.3.3 Spatial Resolution with Strip Time Information

During our first attempt for the extraction of a spatial resolution value originating from the measured strip time, the time-bin information where the maximum pulse height occurs was used. In Figure 4.3 the charge and time shape for a cluster of strips reconstructed in a single Tmm chamber can be seen.

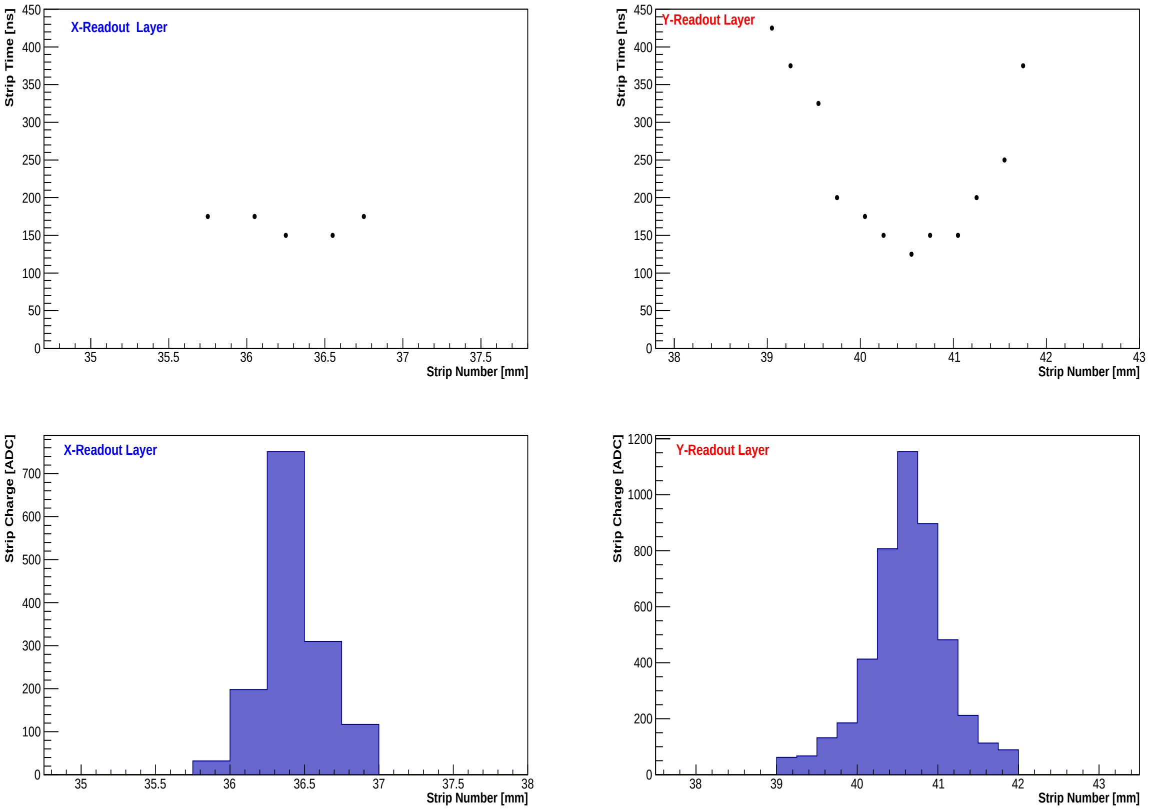

Figure 4.3: Example of an event measured by a Tmm chamber. Top row: Strip time (time-bin×25 ns) as a function of the strip number converted in mm (strip number×0.25 mm) on X and Y readout strips. Bottom Row: Corresponding maximum strip charge distribution.

In the top row of Figure 4.3 the drift time (time-bin ×25 ns) measurement per strip(the strips are converted in mm by multiplying the strip address with the value of strip-pitch which for a Tmm is 0.25 mm) is illustrated. In the bottom row the maximum charge per strip as a function of the strips address (in mm) for the same event can be seen.

From the previous plots it is evident that the X and Y signals differ significantly in both cluster size and time distribution. As we can see the Y readout layer presents a larger number of strips per cluster compared to the X. This phenomenon has its roots in the relative orientation between the resistive strips and the readout strips. In a Tmm chamber the resistive strips are oriented perpendicularly to the Y readout strips while they are oriented parallel to the X readout strips. As a result the charge propagation in one resistive strip induces signals in several Y readout strips through capacitively coupling.

In the case of X-strips all strips measure approximately the same drift time. This is because in case of perpendicular tracks the signals on the resistive strips are coming from the overlapping of different primary clusters spread along a few strips. In the other hand, the time distribution of the Y strips extends for more than 300 ns forming a V-like shape on both sides of the strip with the earliest signal. As the signal propagates along the resistive strip the perpendicularly oriented Y strips measure the peak amplitude at different times that are proportional to the propagation speed of the signal on the resistive strip. This results to a V-shaped distribution shown in the top right of Figure 4.3

From the right column of Figure 4.3 we can see that the charge and time distribution for a cluster of Y readout strips have an equivalent shape. More specifically the strip with the maximum charge is also characterized by the earliest drift time measured in the cluster. In the previous paragraph in order to extract the cluster position, we applied the centroid method to the charge distribution for a cluster of Y readout strips. Based on the same mindset, we intend to estimate the cluster positions but this time using the V-shaped strip time distributions of Y readout layer. The centroid method however would not be an appropriate approach because the most farthest strips will contribute more as they are characterized by larger time values. In order to bypass this issue a method is proposed for the efficient estimation of the cluster position corresponding to the minimum of the V-shaped strip time distribution for a cluster of Y readout strips.

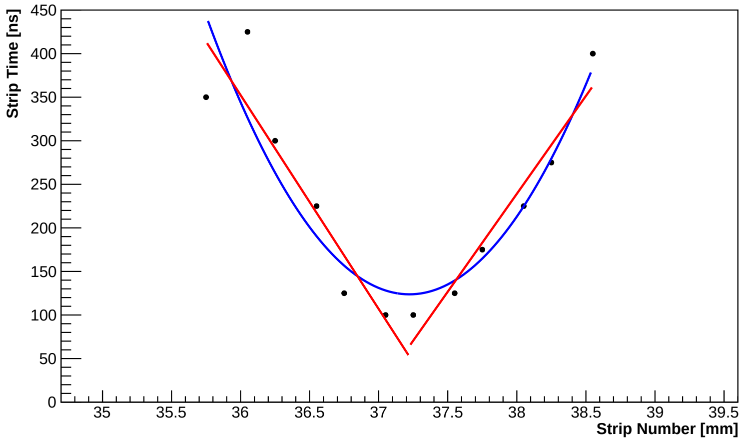

Figure 4.4: A typical second coordinate cluster of Ta Tmm chamber. A fit with a parabola and two straight lines is performed to extract the cluster position, which is defined as the intersection point between the two straight lines.

In the first step the two strips with the largest time values, corresponding to the two edges of the strip time distribution, are identified. By using the position of these strips we then define an area between them in which we apply a fit with a second-degree polynomial function (parabola). Then we extract the position of the parabola minimum (taking into account the spread of charge between adjacent channels) and use it to define two new regions, one for each side of the minimum, extending from the parabola minimum to the previous calculated edge positions of the scatter plot. Finally by using the coordinates of the points for each specific region, we apply a least squares fitting. This processes is implemented in each event and it is illustrated in Figure 4.4. The extracted intersection point between the two straight lines of the fit is defined as the cluster position. Alternatively the parabola minimum could also be used.

Figure 4.5 shows the correlation between the centroids estimated from the maximum strip charge distributions and intersection points from the strip time distributions concerning the Y readout layer of the two Tmm chambers under study. As expected the two quantities show a linear relationship between them.

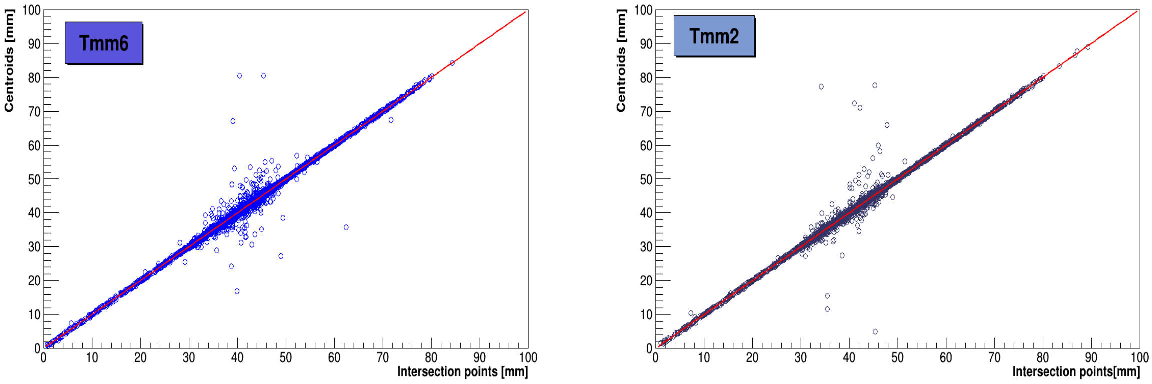

Figure 4.5: Correlation between the centroids and the intersection points estimated respectively from the maximum strip charge and strip time distribution for the Y readout layer of two Tmm type MM chambers (namely Tmm6 and Tmm2).

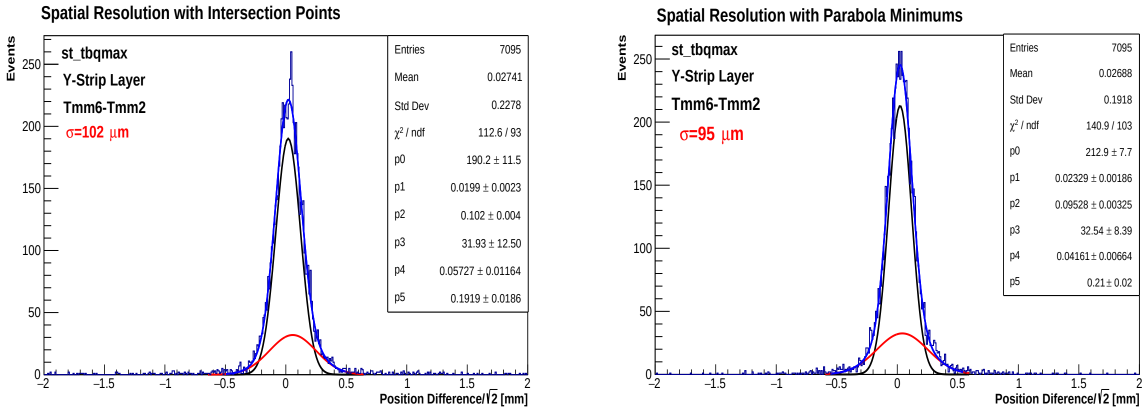

Figure 4.6: Comparison of the hit position difference distributions, calculated using two different cluster position definitions: the intersection point (left) of the straight lines and the minimum of the parabola (right) both extracted from the fitting method applied in V-shaped strip time distribution as shown in Figure 4.4.

The distributions of the hit position difference divided by $\sqrt{2}$, using as cluster position the intersection point and the parabola minimum extracted from the above described precess, are illustrated in Figure 4.6. A fit with a double Gaussian function is performed with the σ of the core Gaussian providing an estimate of the single plane spatial resolution. As we can see, for the case where the time-bin information is used, the two methods result in a spatial resolution of $\approx$100 μm.

In Figure 4.7 the hit position difference divided by $\sqrt{2}$ distributions using the concept of intersection point and parabola minimum is shown. Here however the Fermi-Dirac strip time information is used. The calculations was made for two different data sets (each row corresponds to a different data set with both concerning tracks perpendicular to the detectors plane) in order to examine how the fitting method behaves. Again here a fit with a double-Gaussian was performed. The σ of the core Gaussian provides in each case with an estimation of single detector spatial resolution. The two cluster position definitions used in the two data sets, leads to similar results with the obtained single-plane spatial resolution above 100 μm.

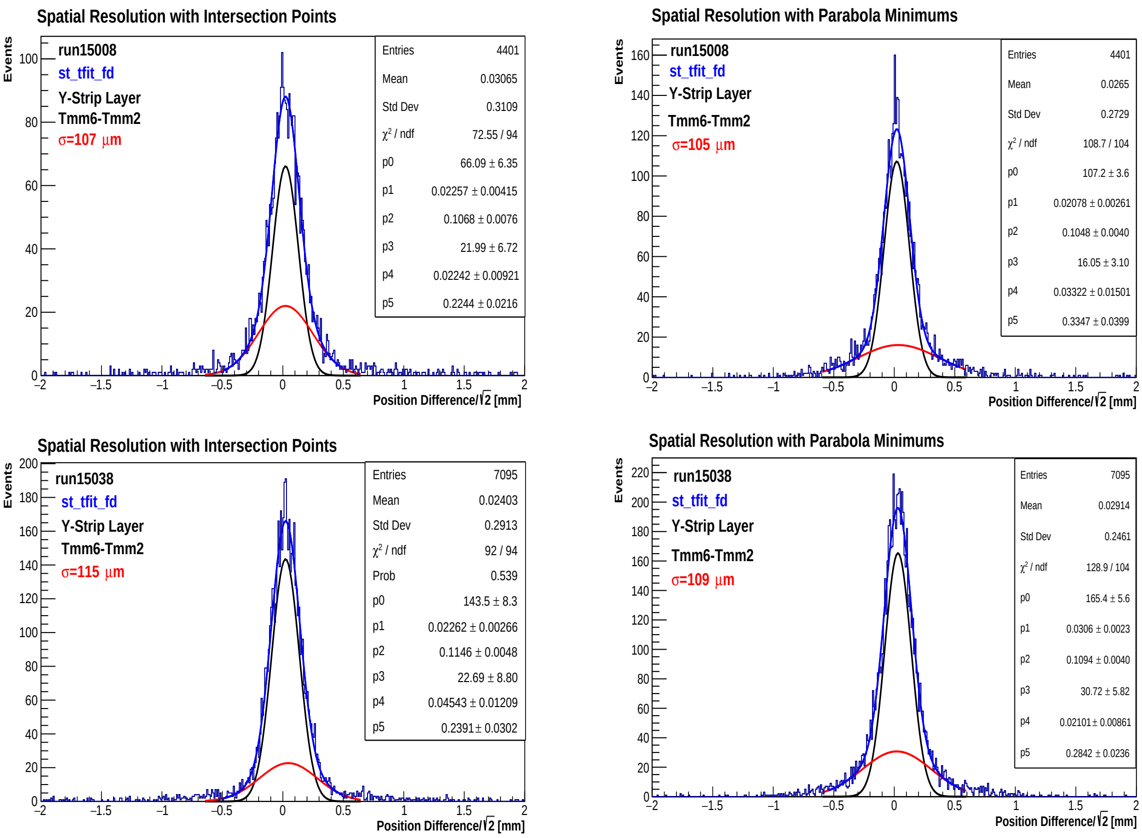

Figure 4.7: Distributions of cluster position differences using the intersection points and parabola minimums, for two different data sets. The Fermi-Dirac strip time information is used.

From the above results it is evident that the charge centroid method estimates a far better single plane spatial resolution value than the corresponding method using the measured strip time. This fact underlines an intrinsic limitation of the Tmm-type MM detector which lies on the fact that in high rates, if several particles pass the detector simultaneously it is impossible to distinguish which x-coordinate is associated with which y-coordinate as different clusters of resistive strips could involve a similar cluster of Y readout strips. This is the main reason why we used perpendicular tracks which are characterized by a small footprint size thus triggering a relatively small number of readout strips. Furthermore the random nature of the ionization processes with an intermediate time between consecutive primary clusters of approximately 6 ns [30] in combination with the 25 ns sabling of the APV25 also affects the detector's time response.

4.4 Estimation of Signal Propagation Speed on the Resistive Strips

As mentioned in the previous section, in the case of the Y readout strips due to the propagation of the signal along the resistive strip, the peak amplitude is measured at different times that are proportional to the propagation speed of the signal on the resistive strip. Thus the slope of the straight lines of the fit illustrated in Figure 4.4 could be used for the extraction of the signal propagation speed on the resistive strips. In Figure 4.8 the signal propagation speed on the resistive strips using the time-bin information, estimated from the slope of the two straight lines laying on the left and right of the parabola minimum in Figure 4.4, in the two Tmm type MM chambers under study is illustrated.

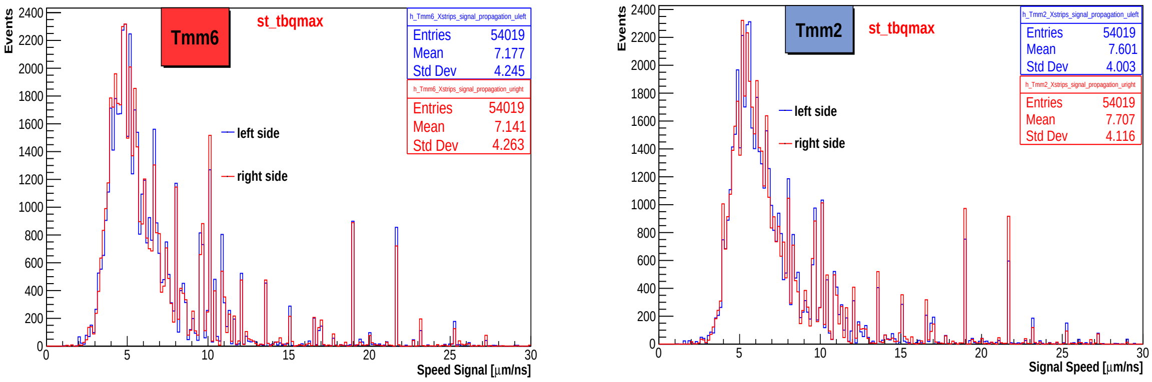

Figure 4.8: The signal speed distributions on the resistive strips of both Tmm type MM chambers under study. The peaks are coming from the inaccuracy of the time-bin information that is used.

The above distributions are both characterized by intense peaks, exposing the limited accuracy of the time-bin information. More particularly the time-bin for the occurrence of the maximum pulse-height results to a discrete time distribution for a cluster of strips which in turn can lead to many events with exactly the same value of signal propagation speed calculated from the least squares fitting.

For the Fermi-Dirac strip time information the situation is different as can be seen in Figure 4.9. The precision of the t_{FD}s leads to a continuous strip time spectrum which is reflected by the smoothness of the signal propagation speed distributions. Each distribution is fitted with a Landau function with signal speed estimated by the most probable value or MPV. The signal propagation speed o the the resistive strips of Tmm6 is found to be a little less than 8 $\mu m/ns$ while in the case of Tmm2 the signal speed is a little above that value. These values are much smaller then the drift velocity of 46 $\mu m/ns$ [30] corresponding to the primary electrons produced during ionization processes.

The small difference in signal speed between the two Tmm type MM chambers originates from the different resistivity values that characterize their corresponding resistive strips. This phenomenon is shown in Figure 4.10 where the strip cluster multiplicity for both the Tmm type MM chambers under study is illustrated. It is evident that in the case of the Tmm2 chamber the mean size of the strip cluster is greater than that of the Tmm6 owning to the smaller resistivity in Tmm2. A lower resistivity value allows the signal to travel faster and easier through the resistive strips resulting to greater signal propagation speed and strip cluster size values.

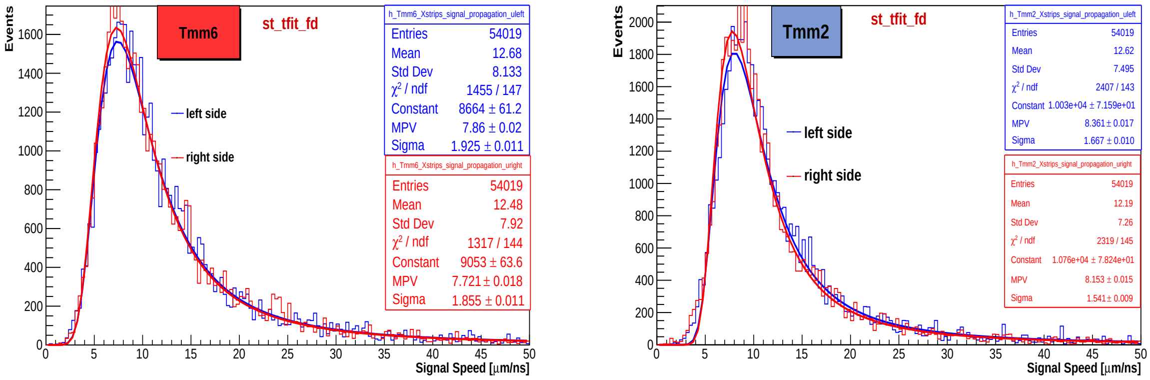

Figure 4.9: The signal speed distributions on the resistive strips of both Tmm type MM chambers under study using the t_{FD} information.

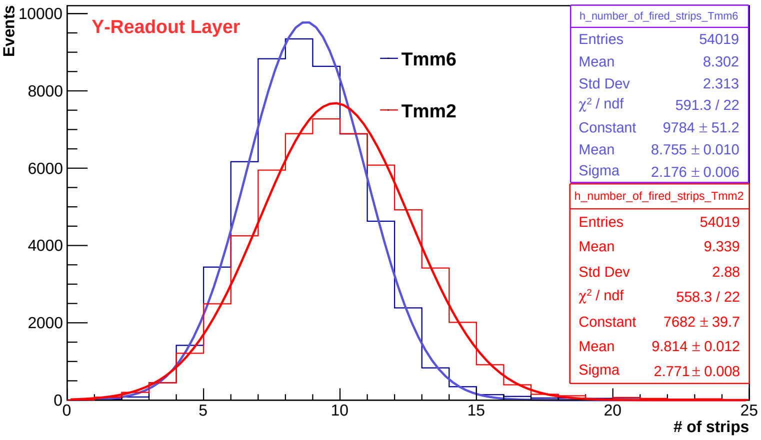

Figure 4.10: The cluster multiplicity for the Y readout layer of two Tmm type MM chambers (namely Tmm6 and Tmm2) in the case of perpendicular tracks.

In the fitting method described in the previous section the incorporated straight lines, from the least squares fitting performed in each side defined by the parabola minimum, do not necessarily share the same slope value. Already from the plots shown in Figure 4.9 it is apparent that there is no proffered direction in which the signal propagates faster than the other. In Figure 4.11 the distribution of the difference between the signal propagation speed on the resistive strips of both Tmm chambers under study extracted from the slopes of the two different straight lines (as depicted in Figure 4.4) can be seen. Both distributions are centered around zero with a systematic uncertainty, independent from the different resistivity that characterizes each detector, estimated at 3 μm/ns.

Under the same framework of examining the uniformity of the signal transmitted through the strips, two additional features of the recorded signal distribution for the the Y-readout layer, were examined. In the left plot of figure 4.12 the number of of fired strips on either side of the parabola vertex is illustrated. No difference between the two distributions was observed with an estimated mean number of four fired strips for each side.

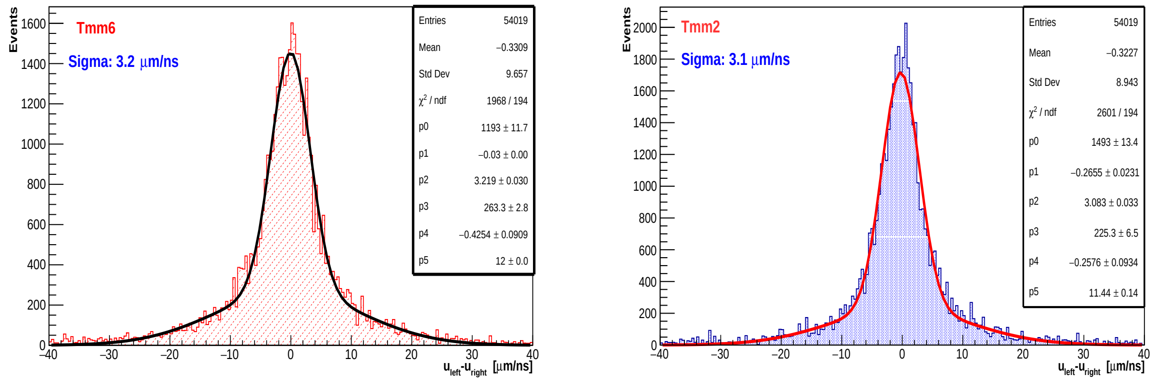

Figure 4.11: Distributions of the difference between the signal propagation speed in resistive strips of the two Tmm MM chambers under study, for the two transmission directions as defined by the parabola vertex illustrated in Figure 4.4.

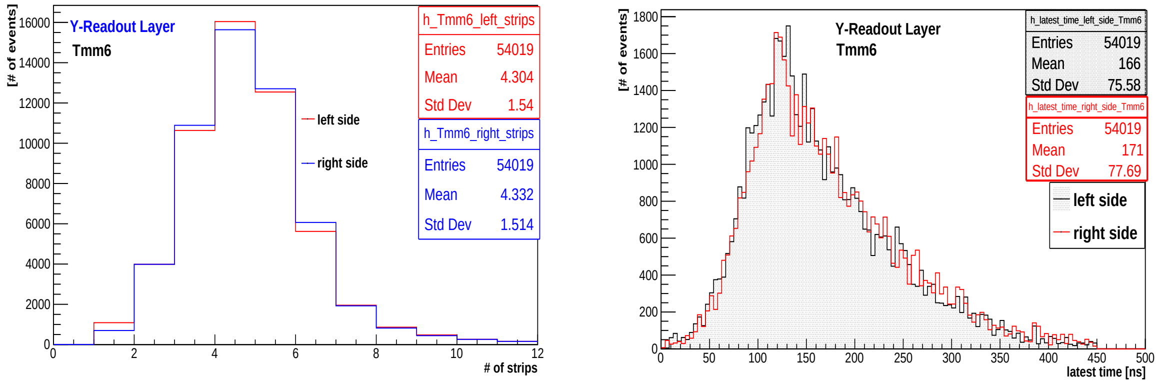

Figure 4.12: Left: Number of fired strips for both sides defined of the parabola vertex in Figure 4.4. Right: Timing distribution of the strips with the latest time within a cluster of Y-strips an incident track angle of 0°.

The right plot of the same figure presents the distributions of the time (t_{FD}) as measured by the two strips farthest from the center, corresponding to the edge points of the scatter plot of Figure 4.4. Yet again here the distributions are in great agreement with each other on their most part with no particular differences between them. The above results confirm that the readout electronics which are installed on the one side of the MM detector, do not affect in any way the propagation of the signal on the detector's strips.

4.5 Timing Resolution Study

For the estimation of the timing resolution (with the combination of the Tmm-type MM chambers and APV25 front-end electronics) a single time measurement in one chamber needs to be compared to a reference time in an event per event basis. The single MM timing resolution was estimated by comparing the measured timing performance in the two Tmm chambers. The timing resolution was extracted using both readout layers where in the case of the Y layer the time measurement per chamber is defined as the time value corresponding to the calculated intersection point between the two fit straight lines (Figure 4.4), while for the X layer the earliest time within a cluster of strips for each Tmm chamber per event was used.

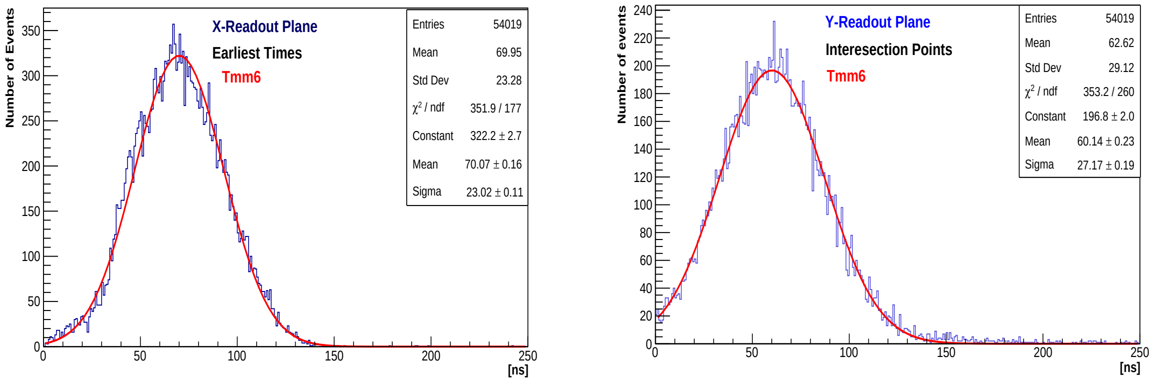

Figure 4.13: Distributions of time measurement corresponding to the two readout layers of a single Tmm-type MM chamber. In the Y readout layer situation the time measurement of each event is defined as the y-coordinate of the intersection point extracted from the two straight lines from the fitting process illustrated in Figure 4.4, while for the X readout layer the earliest time within a cluster of strips was used.

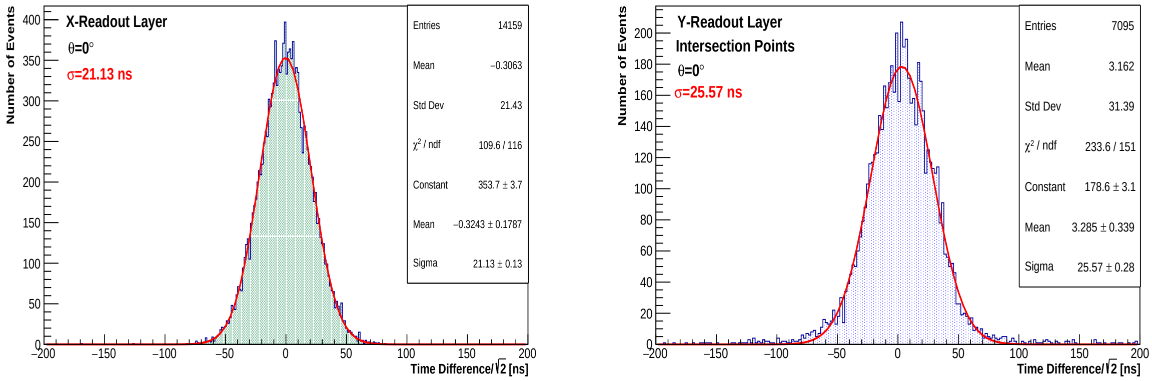

Figure 4.14: Distribution of the earliest difference between two Tmm type MM chambers divided by $\sqrt{2}$ for perpendicular to the detectors plane tracks, for both X (left) and Y (right) readout layer.

The time distributions, for the above mentioned definitions of time measurement, for both readout layers of a single Tmm chamber are illustrated in Figure 4.13. For perpendicular to the detector plane tracks multiple ionization has a high probability to occur in the vicinity of a single readout strip. As a result the readout electronics integrate the charge induced by several clusters and the signal is a sum of signals originating from all these clusters. This effect introduces a large uncertainty to time measurement, justifying the large width that characterizes both distributions while the tail the tails on the right of the distribution are due to the fluctuations of the first ionization positions. In Figure 4.14 the time measurement difference between the two Tmm chambers under study (Tmm2 and Tmm6) divided by $\sqrt{2}$ for perpendicular tracks can be seen. The distributions are fitted with a Gaussian function. The timing resolution, extracted from the σ, is estimated above 20 ns for both readout layers indicating the large uncertainty that governs the time measurement in the case of 0° track angle.

4.6 Monte Carlo Simulation

In order to further study the previous results a Monte Carlo simulation was applied. The MC algorithm was developed within the ROOT framework and its main purpose is to simulate the V-shaped events as seen in Figure 4.4. Then by using the simulated events we apply the fitting method described in section 4.3.3 and examine how the extracted spatial resolution reacts with the inserted values of time uncertainty.

4.6.1 Simulation Steps

For the event reconstruction a random sampling is applied to the fit curves that were implemented on the data. More specifically by using the methods provided by the built-in random generator of the ROOT framework we were able to generate random numbers according to our fit distributions with which a set of 40000 events were constructed. The logical steps that were used are described as follows:

Number of fired strips

The first obvious step is to define the number of fired strips in each event. This is achieved by simply generate two sets of random numbers, each corresponding to one of the two Tmm chambers under study, from the two Gaussian distributions of Figure 4.10.

Construction of the minimum point

For the definition of the minimum point of our simulated V-shaped event, the distributions of the two coordinates of the calculated intersection point were used. The x-coordinate of the intersection point is defined as the cluster position in each event and its overall distribution for both Tmm chambers under study is shown in Figure 4.15. Both distributions are fitted with a Gaussian function, the parameters of which is used to generate a random value per entry, corresponding to the x-coordinate of the minimum point for our simulated event. In our simulation, we have explicitly defined the position of the minimum strip to be exactly the same for both detectors. In the same way the y-coordinates are estimated by using the extracted parameters from the Gaussian fitting applied on the distribution of time values corresponding to the intersection points (right part of Figure 4.13).

Generation of simulated data points

After the minimum point is determined, the simulated data points are created separately on each side of it. The number of points (strips) on each side is decided depending whether the total number of fired strips for the specific simulated event is even or odd. Let us assume N fired strips. If N is an odd number, then the number of data points for both sides of the minimum would simply given by $(N-1)/2$. In the case of an even number of fired strips however the situation is slightly different with one side hosting $N/2$ strips and the other having $(N-1)/2$ strips. The side containing the most points is selected randomly each time in order to maintain a random event pattern. The strip along with their corresponding time values on each side of the minimum are then simply given by:

$$\begin{aligned} s_i &= s_0 \pm i, && i = 1, 2, ..., n \\ t_i &= t_0 + \frac{\text{st\_pitch} \times i}{u_{right(left)}}, && i = 1, 2, ..., n \end{aligned} \tag{4.4}$$

where n is the number of strips located in the one of the two sides of the minimum, $u_{right}(u_{left})$ is a random value of the signal speed on the resistive strips on the right (left) side of te minimum, generated from the Landau fit functions of Figure 4.9, s_0 is the strip number corresponding to the lowest time value t_0 while st_pitch represents the strip pitch of the Tmm chamber which is equal to 250 mm. By summing the two sets of data points, with each of them produced in the one of the two sides of the minimum, the unified variables of strip number and time are obtained.

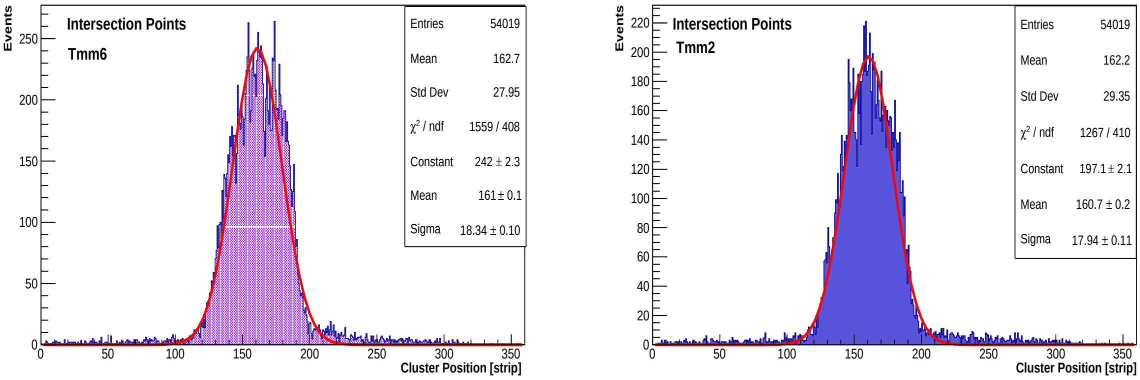

Figure 4.15: Cluster position for both Tmm6 (left) and Tmm2 (right) chambers, defined as the x-coordinate of the estimated intersection point between the two straight lines of Figure 4.4

4.6.2 Simulation Results

A generated event corresponding to one of the two Tmm chambers, is shown in the left part of Figure 4.16. In the absence of any time uncertainty the data points are perfectly aligned with each other, with the two straight lines of the fit passing through all points of the scatter plot on each side of the minimum. As a result, the distribution of the difference between the calculated intersection points of each chamber is localized precisely to zero (resembling a Dirac delta function) corresponding to maximum positioning accuracy.

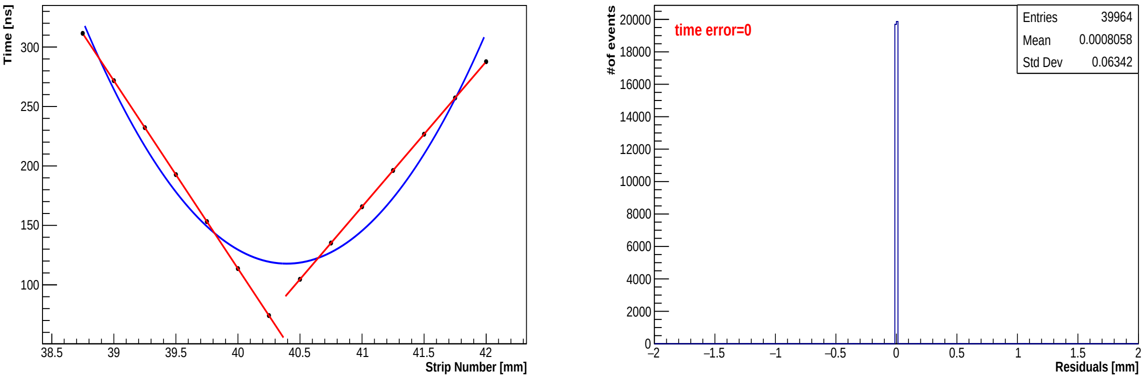

Figure 4.16: A generated event characterized by a zero time uncertainty (left) and the distribution of the hit position difference, for the same value of time uncertainty (right).

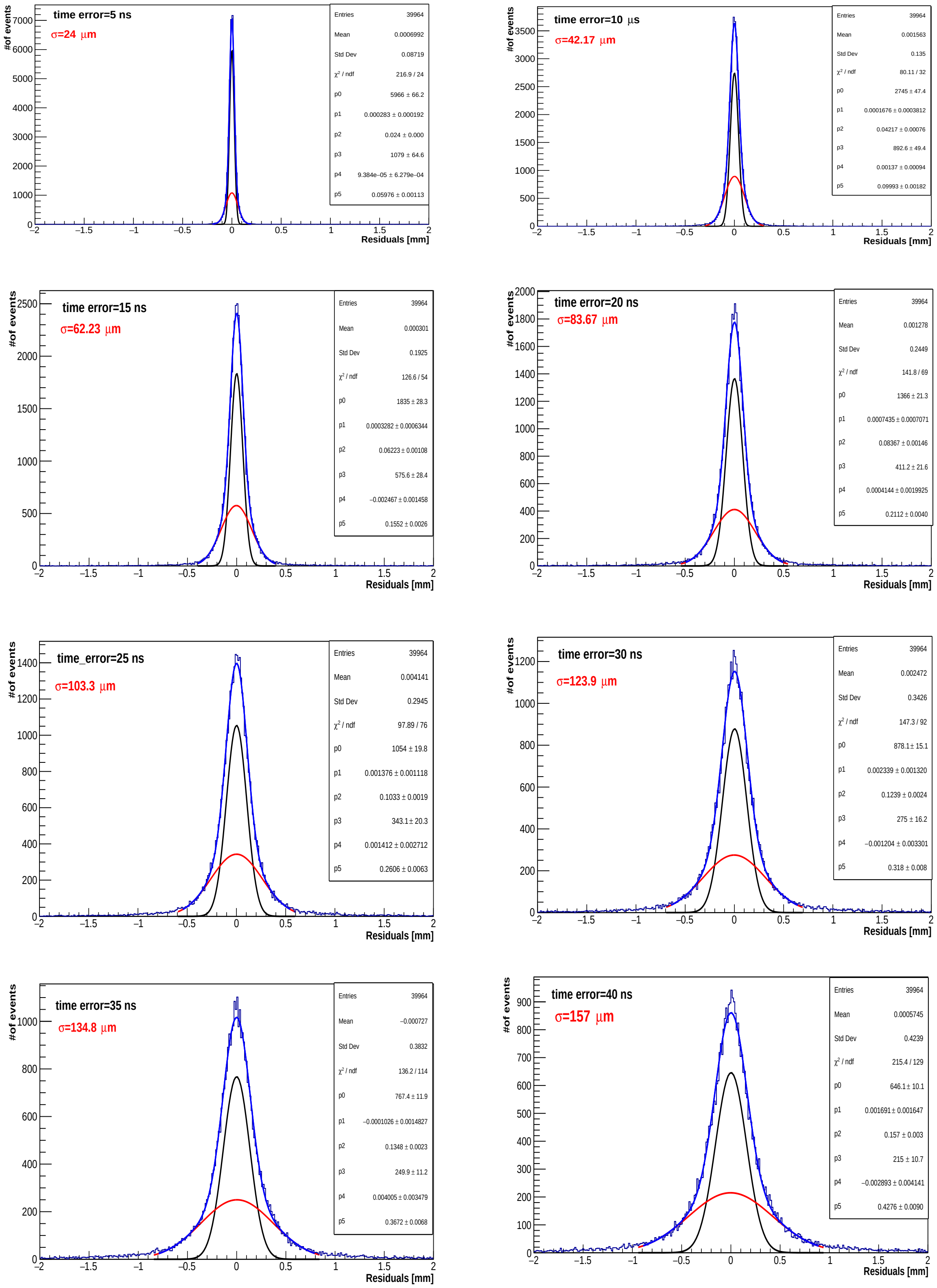

Figure 4.17: Distributions of the generated cluster position (intersection point) difference divided by $\sqrt{2}$ for different values of time uncertainty.

Starting from this non-realistic situation, we then move by inserting uncertainty to the generated time values. This was achieved by replacing each time value with a random one which follows a Gaussian distribution with mean equal to the initial time value t_i and a standard deviation σ. The spatial resolution, calculated by using the intersection points as cluster positions, is observed by varying the time uncertainty from 5 ns to 40 ns in steps of 5 ns. In Figure 4.17 the various distributions of the generated cluster position difference divided by $\sqrt{2}$, for different values of time uncertainty are illustrated. Each distribution is fitted with a double Gaussian and the intrinsic spatial resolution is extracted from the σ of the core Gaussian. As expected the measured resolution deteriorates with the increase of time uncertainty.

In Figure 4.18 the overall result of the the MC simulation is illustrated. It is shown that the generated σ grows almost linearly with the time uncertainty. The actual point of interest is at the time uncertainty of 25 ns, where as can be seen the corresponding spatial resolution could exceed the value of 100 μm. This result is in good agreement with the values of the spatial and time resolution extracted from the data and pinpoints the inability of strip time measurement characterized by high uncertainty to estimate a precise cluster position thus leading to a worse spatial resolution.

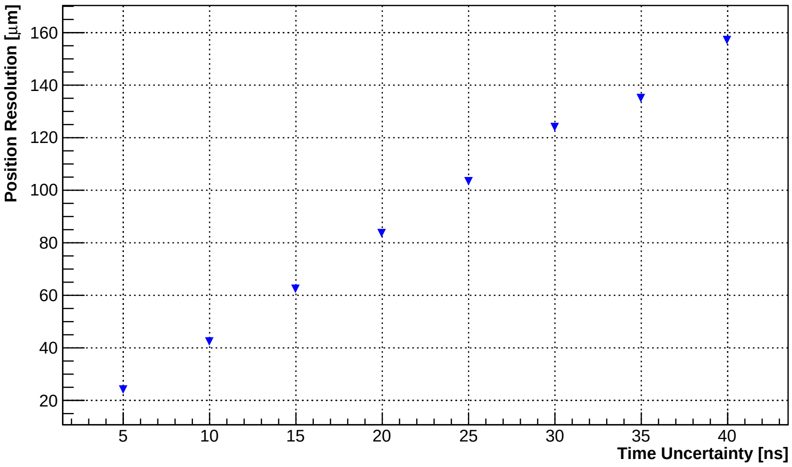

Figure 4.18: Simulation of the spatial resolution of a Tmm chamber using the strip time information of the Y readout layer versus the time uncertainty.

4.7 Study of Tmm-type MM Chambers with Cosmic Muons

Additional analysis concerning the Tmm-type MM chambers was carried out, by performing measurements with cosmic muons. Three Tmm chambers are studied here while a set of three scintillators were used to provide the triggered signal.

4.7.1 Experimental Setup

The cosmic muon test setup in the Laboratory of Experimental High Energy Physics of the National and Technical University of Athens (NTUA) (see Figure 4.19) operates three Tmm-type MM placed in parallel one on top of the other. The Tmm chambers we used to obtain our results have an active area of 10 × 10 cm^2 with a strip pitch of 250 μm for both Y and X readout strips[4]. The X readout strips demonstrate a width of 150 μm, while a width of 80 μm corresponds to the Y readout strips. The amplification region has a height of 128 μm which is separated by a micromesh from the drift and the

---

[4] The characteristics of the Tmm-type MM chambers are described in Chapter 3.

conversion region with a height of 5 mm. The cylindrical spacers (pillars) that keep the mesh above the readout strips, have a diameter of 300 µm and a pitch of 2.5 mm. The gap between the two electrodes was filled with a Ar+7%CO_2 gas mixture provided from pre-mixed bottles. In terms of the high voltage scheme used, a voltage of -300 V and 520 V was supplied to the drift electrode and the resistive strips respectively, while the mesh was kept grounded. This scheme corresponds to an field of 600 V/cm in the drift region and in a 41 kV/cm field in the amplification region. A trigger was used for the setup, provided by a coincidence of three scintillators.

Figure 4.19: Photos of the cosmic muon experimental setup. At the bottom right of the figure, three out of the six APV25 hybrid cards mounted in a Tmm-type MM chamber can be seen.

The readout of the Tmm-type MM chambers was performed by APV25 [31] hybrid cards (bottom-right in Figure 4.19) via the so called Scalable Readout System [32] (SRS). A schematic representation of the SRS system in its simplest configuration can be seen in Figure 4.20. It consists of two APV25 front-end boards, a digitizer card (ADC), a Front-end Concentrator Card (FEC) and the Data Acquisition PC. One APV25 hybrid contains 128 channels, which each are AC coupled to one readout strip of the MM detector. All channels have a spark protection system. The APV25 hybrid is by design either a master or a slave. The master board is connected to the ADC through a commercial HDMI cable, while the slave board does not host a micro-HDMI connector and it is connected to the master board via a flat cable. The master and slave boards are read in parallel delivering a analog CR-RC shaped signals. The hybrid records the value of the shaped signal every 25 ns and stores it in a 192 column deep analogue memory. The adapter board contains the ADC (digital-to-analog converter) and links to the band-end of the system. One SRS ADC board can read up to 16 APV25 hybrid boards, 8 master and 8 slave. The trigger signal (NIM pulse) is received by the FPGA-based FEC board, containing most of the complex circuits of the DAQ, which in turn sends the data to a computer via a copper-based Gigabit Ethernet. The ADC and FEC boards are installed in a standard 6U eurocrate containing also a power supply.

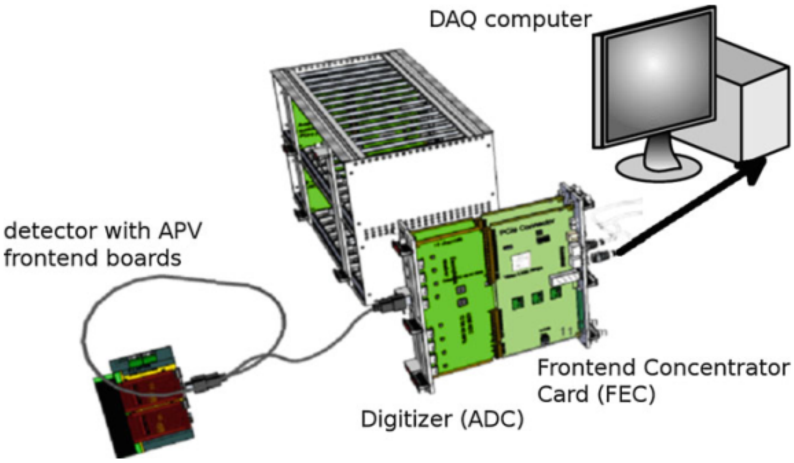

Figure 4.20: The basic elements of the SRS and the intermediate connectivity.

4.8 Measurements & Results

A typical signal distribution for the Y-readout layer measured in two different Tmm chambers can be seen in Figure 4.21. The fitting method described in section 4.3 is applied to the distributions for the extraction of the signal speed information on the resistive strips for each event.

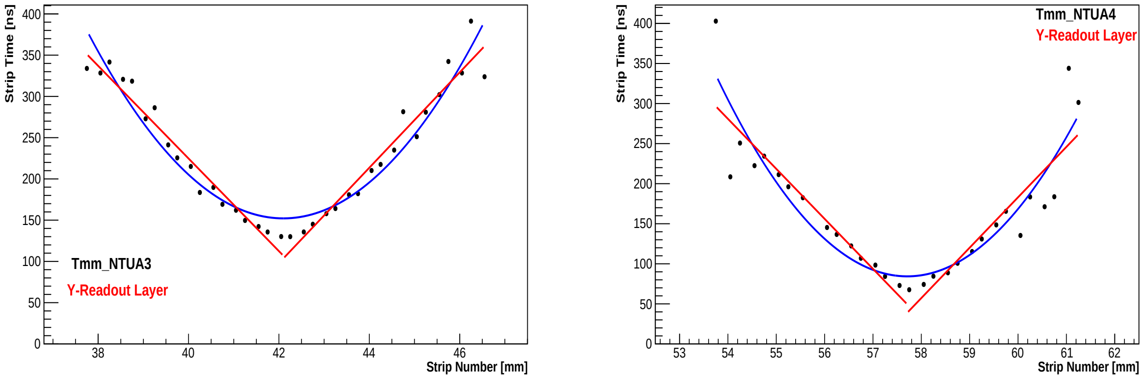

Figure 4.21: Recorded signal distribution of an incident cosmic muon for the Y-readout layer of Tmm_NTUA3 (left) and Tmm_NTUA4 (right).

In the above plots we can clearly see that the number of fired strips consisting the cluster, is quite large for both detector cases. This is strongly correlated with the small resistivity values that characterize these specific detectors. As we discussed in paragraph 4.4, a small resistivity allow the signal to propagate more freely through the resistive strips, thus leading to larger cluster sizes. This is evident in Figure 4.22 where the distributions of the propagation speed of the signal on the resistive strips of two Tmm chambers (namely Tmm_NTUA3 and Tmm_NTUA4) from our experimental setup, are illustrated. Both distributions are well fitted with a Landau function with the signal speed value extracted from the MPV. The obtained signal speed for the two chambers is close to 15 µm/ns, a value approximately twice the magnitude of that extracted from the distributions illustrated in Figure 4.9 (≈8 µm/ns), indicating the big difference in resistivity between the two sets of Tmm chambers.

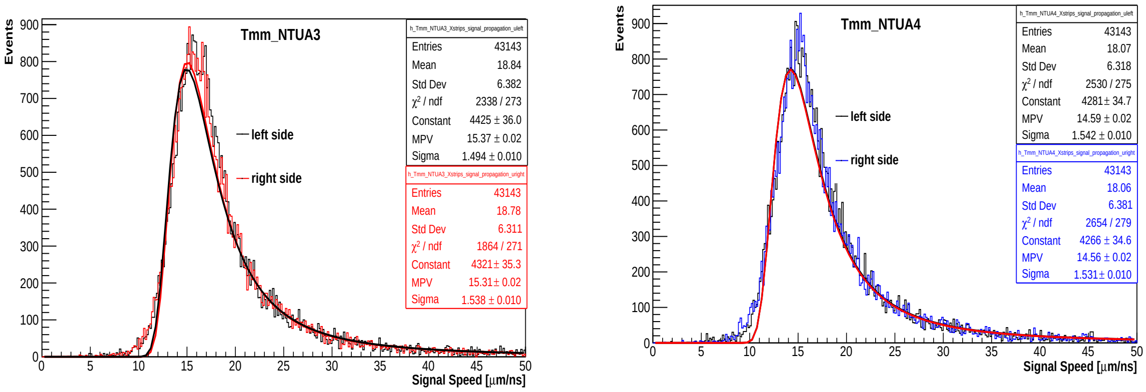

Figure 4.22: The propagation speed of the signal on the resistive strips of Tmm_NTUA3 (left) and Tmm_NTUA4 (right).

In the top row of Figure 4.23 the distributions of the number of clusters for the X-readout layer of the three Tmm chambers under study are shown. As can be seen, the multiple track events concern only a very small fraction of the total events. In the bottom row of the same figure, the integrated cluster charge distributions for single-cluster events (collected by the X-strips) measured by the three Tmm chambers, are illustrated. A Landau fit is imposed to all distributions. The MPV gives an estimation of the mean cluster charge in each detector.

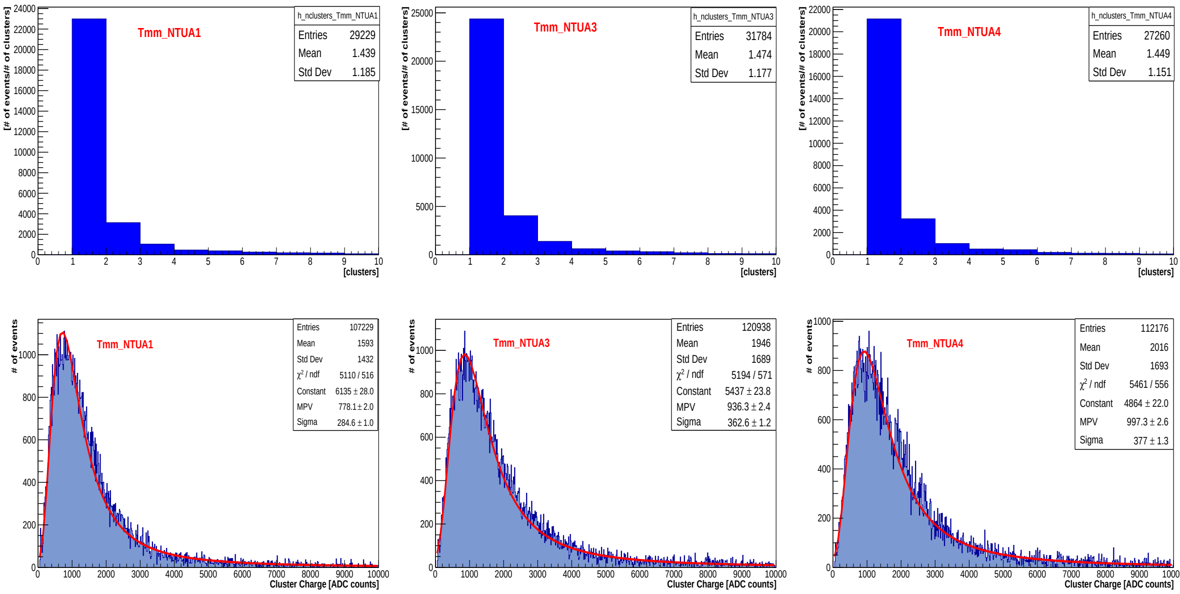

Figure 4.23: Top row: Distributions of the number of clusters for the three Tmm-type MM chambers. Bottom row: Corresponding cluster charge distributions for the same detectors.

4.8.1 Alignment and Angle Reconstruction

In order to perform a precise analysis, it is of great importance for the three Tmm-type MM chambers under study to be aligned offline. To achieve this we use the middle chamber (Tmm_NTUA3) as reference and calculate the hit position differences (the centroid method was implemented on the X-readout strips of each detector for the hit position estimation) of Tmm_NTUA1−Tmm_NTUA3 and Tmm_NTUA4−Tmm_NTUA3. The residual distributions are fitted with a Gaussian (see top row of Figure 4.24) and the mean value extracted gives an estimate of the systematic misalignment that the outer chambers have in terms with the reference chamber. Then the corrected hit positions, defined as X_1^*, X_2^* and $X_3{}^*$, are simply given by:

$$\begin{aligned} X_1^* &= X_1 - \alpha \\ X_3^* &= X_3 \\ X_4^* &= X_4 - \beta \end{aligned} \tag{4.5}$$

where X_1, X_3 and X_4 are the initial hit positions in Tmm_NTUA1, Tmm_NTUA3 and Tmm_NTUA4 before the correction, while α and β are the extracted mean values from the Tmm_NTUA1−Tmm_NTUA3 and Tmm_NTUA4−Tmm_NTUA3 distributions respectively. In the bottom row of Figure 4.24 the residuals of the corrected hit positions are illustrated. As can be seen, after the correction the initial mean values of the residual distributions are shifted into zero.

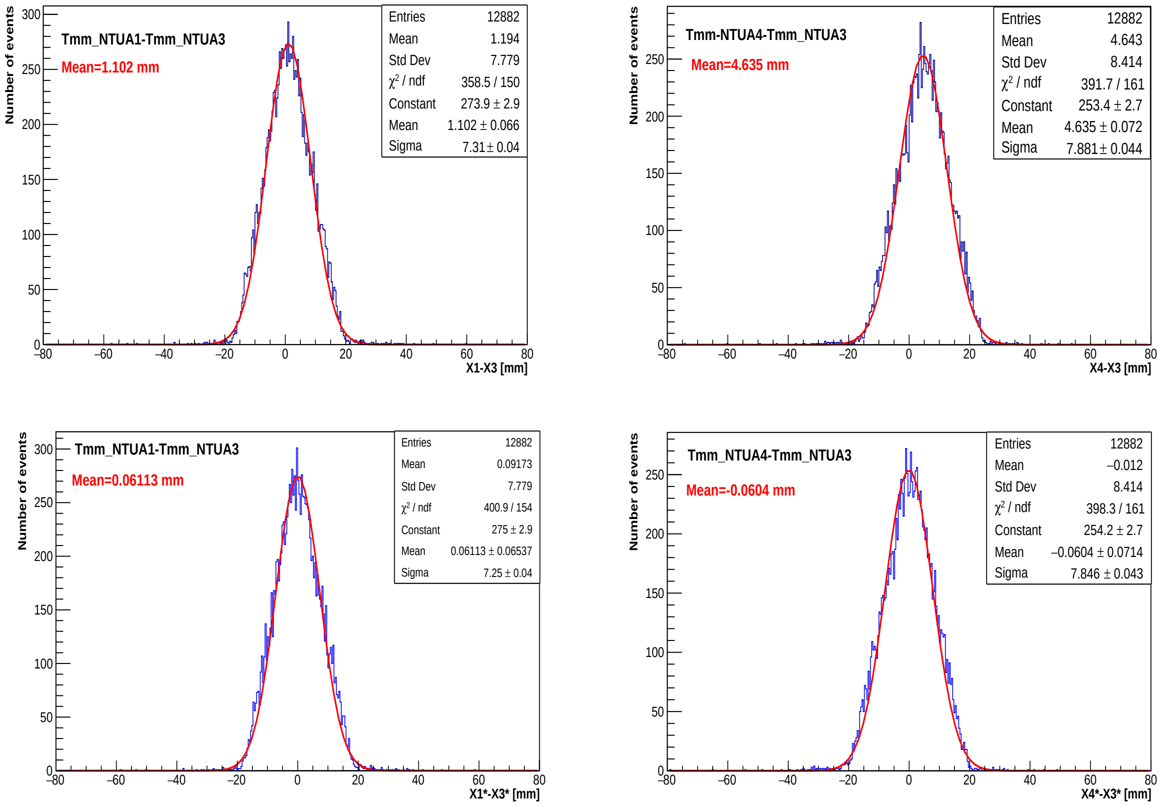

Figure 4.24: Residual distributions for the MM detectors under study, before (top row) and after (bottom) the offline alignment process.

The corrected hit positions can now be used for reconstruction of the incident angle of the cosmic muons. In figure 4.25 a schematic view of the experimental setup used along with an example of a muon track formation using hits reconstructed on all chambers, is shown. The corresponding distances between the different detecting layers can also be seen.

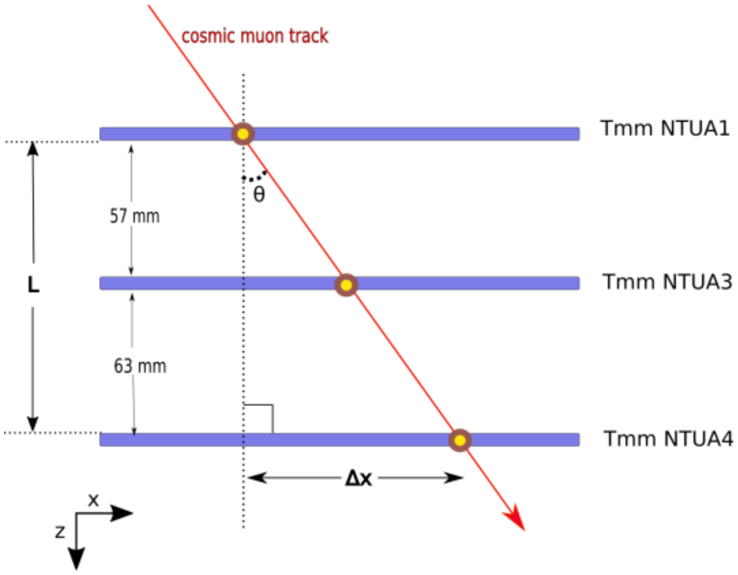

Figure 4.25: Schematic representation of the detecting layers consisting the experimental array with their intermediate spacings. An example of a cosmic muon passing through all the Tmm chambers is also depicted.

In the left part of Figure 4.26 a typical event with the reconstructed hits (with the use of the centroid method and the application of the previously described correction process) on all Tmm chamber is shown. The hit positions, represented by the blue points in the graph, are fitted with a straight line using the the least squares fitting method. The slope of the line allows for the estimation of the track inclination. More specifically, the tangent of the muon incident angle can simply derived by:

$$\tan(\theta) = \frac{\Delta x}{L} = \frac{1}{p_1} \tag{4.6}$$

where Δx and L(=120 mm) is the hit position difference and the distance between the two outer chambers (Tmm_NTUA1 and Tmm_NTUA4 as can be seen in Figure 4.25) respectively, while p_1 is the parameter corresponding to the slope of the fit line.

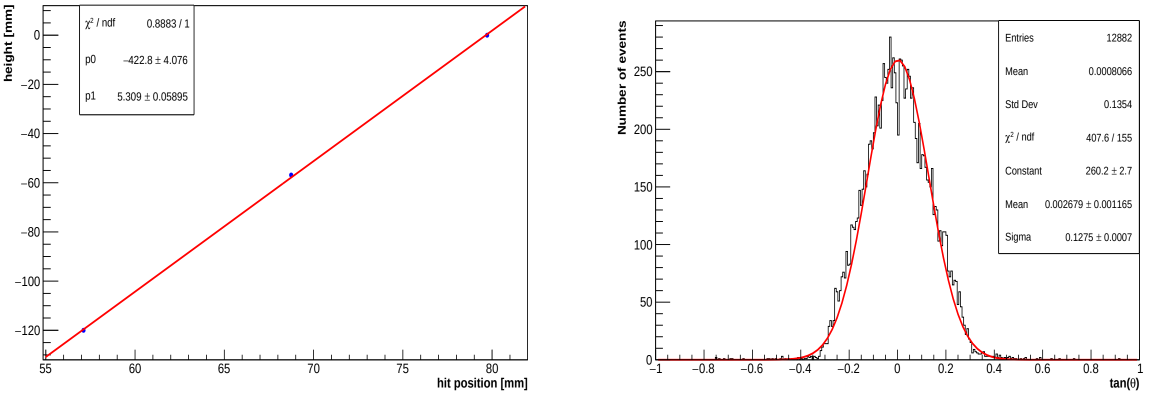

Figure 4.26: Left: An event showing the reconstructed muon path. Right: Tangent of the cosmic muons incident angle.

The right part of Figure 4.26 illustrates the distribution of the tangent of the cosmic muons incident angle ($\tan(\vartheta)$). The mean value of the distribution is around zero, in good agreement with the typical $\cos^2$ distribution that characterize the cosmic ray muon flux at sea level. In Figure 4.27 the hit position difference between two Tmm chambers as a function of $\tan(\vartheta)$ is illustrated. As expected, the residual values increase linearly with the muon incident angle.

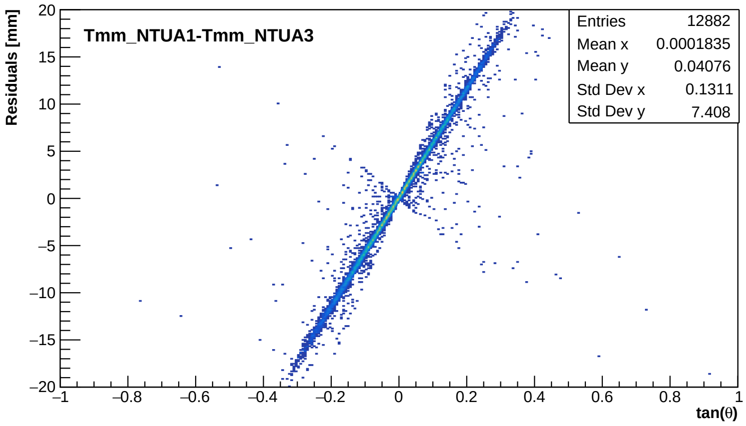

Figure 4.27: Hit position difference between two Tmm-type MM chambers versus the tangent of the cosmic muons incident angle.

4.8.2 Estimation of the Single Plane Spatial Resolution using the Geometric Mean Method

For the estimation of the single plane spatial resolution the geometric mean method was used. This method, proposed by Carnegie et al. [33] is described as follows: Let us assume a system of three MM chambers that measure straight tracks of charged particles. The reconstructed hit positions on all three MM chambers are fitted with a straight line (see left part of Figure 4.26) and the extracted track parameters are used for the determination of the predicted hit position. Then the residual between the measured and the predicted hit position is calculated. The distribution of residuals is fitted with a Gaussian function, yielding a resolution σ_{in}. Since the detector under study is included in the track fit, the result is biased in favor of smaller resolution values.

In the other hand, if the detector under study is specifically excluded from the track fit, the resolution σ_{in}, originating from the corresponding residual distribution, will be larger than the spatial resolution of the detector.

According to Carnegie et al. [33] the true spatial resolution σ of the test detector can be approximated by the geometric mean of these two measurements:

$$\sigma = \sqrt{\sigma_{in}\sigma_{ex}} \tag{4.7}$$

The single plane hit positions in our case concern the X readout layer of the Tmm chambers and were reconstructed using the Centroid method. The geometric mean method was implemented for the following angular ranges: $|\tan(\theta)| \leq 0.02$, $0.02 \leq |\tan(\theta)| \leq 0.05$, $0.05 \leq |\tan(\theta)| \leq 0.1$,$0.1 \leq |\tan(\theta)| \leq 0.15$, $0.15 \leq |\tan(\theta)| \leq 0.2$, $0.2 \leq |\tan(\theta)| \leq 0.25$ and $0.25 \leq |\tan(\theta)| \leq 0.3$. The results of this procedure are illustrated in Figure 4.28. As expected the single plane spatial resolution degrades almost exponentially with the increase of the incident angle owing to the lack of precision that the Centroid method presents with increasing cluster size. For almost perpendicular tracks the spatial resolution is estimated above 100 μm due to the small number of reference chambers.

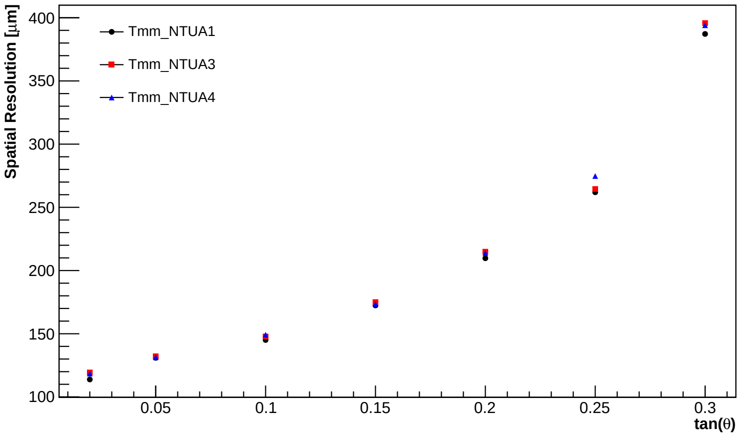

Figure 4.28: Single plane spatial resolution estimated for different angular ranges.

4.9 Strip Cluster Multiplicity

The strip cluster multiplicity concerning the X-readout layers of the three Tmm chambers under study, was estimated. Owing to the incident angle or diffusion there is high probability for the ionization electrons to be selected from more than one strip. As a result a number of strips will receive charge from a single ionizing particle, forming a cluster of strips. In Figure 4.29 the mean values of the cluster multiplicity distributions for the angular ranges defined in the previous section are illustrated. As can be seen, the cluster multiplicity shifts towards larger values as the incident track angle increases.

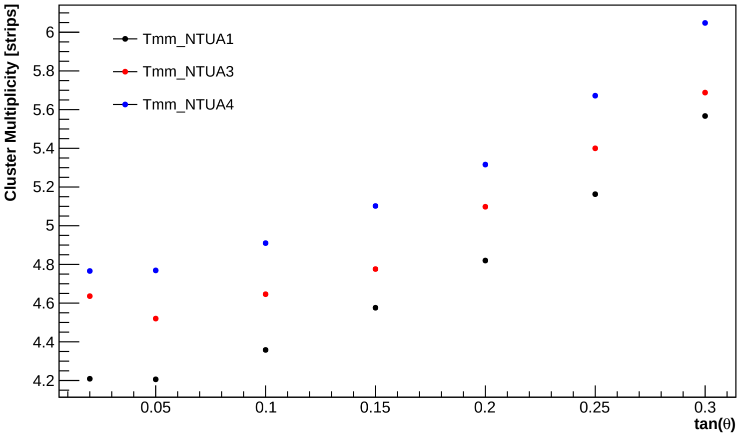

Figure 4.29: Cluster multiplicity as a function of the incident track angle for the three Tmm-type MM chambers under study.

Conclusion

In this thesis the 2D resistive Micromegas (Tmm-type MM) detectors were studied, using data from the test-beam of November 2015 that took place in SPS/CERN. The main goal was the examination of whether the strip time information could provide an accurate hit position reconstruction. For this purpose a fitting method was developed allowing for the estimation of the position of minimum time for a cluster of strips in the Y-readout layer. The spatial resolution calculated by using this cluster positions was found to be above 100 µm, a value far worse than that estimated with the charge centroid method ($\approx$ 64 µm). This result indicates that time information governed by large time uncertainty, are not able to provide a precise hit position reconstruction, thus leading into a bad spatial resolution. This uncertainty, in the case of perpendicular tracks with which we are dealing here, was calculated above 20 ns in both readout layers (X and Y). Using the previous fitting method we estimated the propagation speed of the signal on the resistive strips acquiring also a first look at the resistance that characterizes the resistive strips of different Tmm chambers. A number of studies that followed showed that the signal propagates uniformly in the resistive strip having the same speed in all directions (right and left of the cluster position). A Monte Carlo algorithm was also developed verifying the previous results. Finally, an analysis was performed concerning an experimental setup installed in NTUA, consisting of three Tmm-type MM chambers, which performed cosmic ray measurements.

Bibliography

[1] HL-LHC: High Luminosity Large Hadron Collider. DOI: `http://hilumilhc.web.cern.ch/about/hl-lhc-project`.

[2] ATLAS Collaboration. New Small Wheel Technical Design Report. Technical Report CERN-LHCC-2013-006. ATLAS-TDR-020, Jun 2013. DOI: `https://cds.cern.ch/record/1552862`.

[3] Stefaan Taverier. *Experimental Techniques in Nuclear and Particle Physics*. Springer, 2010.

[4] J Beringer and Others. Review of Particle Physics (RPP). *Phys. Rev.*, D86(9):10001, 2012. DOI: `http://inspirehep.net/record/1126428`.

[5] I. Giomataris, R. De Oliveira, S. Andriamonje, S. Aune, G. Charpak, P. Colas, G. Fanourakis, E. Ferrer, A. Giganon, Ph Rebourgeard, and P. Salin. Micromegas in a bulk. *Nuclear Instruments and Methods in Physics Research, Section A: Accelerators, Spectrometers, Detectors and Associated Equipment*, 560(2):405–408, 2006.

[6] Georgios Iakovidis, Theodoros Alexopoulos, and Georgios Tsipolitis. Study of Resistive Micromegas in a Mixed Neutron and Photon Radiation Field. 2011. DOI:`http://arxiv.org/abs/1111.3185{%}0Ahttp://dx.doi.org/10.1088/1748-0221/7/05/C05001`.

[7] Michele Bianco, Hans Danielsson, Jordan Degrange, Rui De Oliveira, Andreas Düdder, Edoardo Farina, Fabian Kuger, Paolo Iengo, Francisco Perez Gomez, Tai-Hua Lin, Matthias Schott, Givi Sekhniaidze, Federico Sforza, Ourania Sidiropoulou, Chrysostomos Valderanis, Maurice Vergain, and Jörg Wotschack. Construction of two large-size four-plane micromegas detectors. 2015. DOI:`http://arxiv.org/abs/1511.03884{%}0Ahttp://dx.doi.org/10.1016/j.nima.2016.01.049`.

[8] Oliver Sim Brüning, Paul Collier, P Lebrun, Stephen Myers, Ranko Ostojic, John Poole, and Paul Proudlock. *LHC Design Report*. CERN, Geneva, 2004. DOI: `https://cds.cern.ch/record/782076`.

[9] Carlo Wyss. *LEP design report, v.3: LEP2*. CERN, Geneva, 1996. DOI: `Vol.1-2publ.in1983-84`.

[10] ATLAS Collaboration. The ATLAS Experiment at the CERN Large Hadron Collider. *Journal of Instrumentation*, 3(08):S08003–S08003, 2008. DOI: `http://stacks.iop.org/1748-0221/3/i=08/a=S08003`.

[11] CMS Collaboration. *CMS Physics: Technical Design Report Volume 1: Detector Performance and Software*. Technical Design Report CMS. CERN, Geneva, 2006. DOI: `https://cds.cern.ch/record/922757`.

[12] LHCb Collaboration. *LHCb : Technical Proposal.* Tech. Proposal. CERN, Geneva, 1998. DOI: `https://cds.cern.ch/record/622031`.

[13] TOTEM Collaboration. TOTEM, Total Cross Section, Elastic Scattering and Diffraction Dissociation at the LHC: Technical Proposal. Technical Report CERN-LHCC-99-007. LHCC-P-5, CERN, Geneva, Mar 1999. DOI: `https://cds.cern.ch/record/385483`.

[14] ALICE Collaboration. *ALICE physics performance: Technical Design Report.* CERN, Geneva, 2005. DOI: `https://cds.cern.ch/record/879894`.

[15] ATLAS Collaboration. *ATLAS inner detector: Technical Design Report, 1.* Technical Design Report ATLAS. CERN, Geneva, 1997. DOI: `https://cds.cern.ch/record/331063`.

[16] ATLAS Collaboration. *ATLAS liquid-argon calorimeter: Technical Design Report.* Technical Design Report ATLAS. CERN, Geneva, 1996. DOI: `https://cds.cern.ch/record/331061`.

[17] Atlas Collaboration. *ATLAS magnet system: Technical Design Report, 1.* Technical Design Report ATLAS. CERN, Geneva, 1997. DOI: `http://cds.cern.ch/record/338080`.

[18] ATLAS Collaboration. *ATLAS muon spectrometer: Technical Design Report.* Technical Design Report ATLAS. CERN, Geneva, 1997. DOI:`https://cds.cern.ch/record/331068`.

[19] Bernd Stelzer. The New Small Wheel Upgrade Project of the ATLAS Experiment. *Nuclear and Particle Physics Proceedings*, 273-275:1160–1165, 2016. DOI: `http://dx.doi.org/10.1016/j.nuclphysbps.2015.09.182`.

[20] K Ntekas, T Alexopoulos, and S Zimmermann. The ATLAS New Small Wheel Upgrade Project. Technical Report ATL-MUON-PROC-2014-004, CERN, Geneva, Jun 2014. DOI: `https://cds.cern.ch/record/1711717`.

[21] Claus Grupen, Boris Shwartz. *Particle Detectors*, volume 26 of *Cambridge Monographs on Particle Physics, Nuclear Physics and Cosmology.* Cambridge University Press, 2008.

[22] B. Rossi. *High Energy Particles.* Prentice Hall, Englewood Cliffs, (1952).

[23] Walter Blum, Werner Riegler, and Luigi Rolandi. *Particle Detection with Drift Chambers.* 2008.

[24] Fabio Sauli. The gas electron multiplier (gem): Operating principles and applications. *Nuclear Instruments and Methods in Physics Research Section A: Accelerators, Spectrometers, Detectors and Associated Equipment*, 805:2 – 24, 2016. Special Issue in memory of Glenn F. Knoll.

[25] Y. Giomataris, Ph Rebourgeard, J. P. Robert, and G. Charpak. MICROMEGAS: A high-granularity position-sensitive gaseous detector for high particle-flux environments. *Nuclear Instruments and Methods in Physics Research, Section A: Accelerators, Spectrometers, Detectors and Associated Equipment*, 376(1):29–35, 1996.

[26] Theodoros Alexopoulos. The micromegas project for the ATLAS upgrade. *IEEE Nuclear Science Symposium Conference Record*, 2013. DOI:http://www.physics.ntua.gr/hep/aristeia_figures/paradotea22_paper_IEEE2013_atlas_mm_TheoAlex.pdf.

[27] T. Alexopoulos, J. Burnens, R. De Oliveira, G. Glonti, O. Pizzirusso, V. Polychronakos, G. Sekhniaidze, G. Tsipolitis, and J. Wotschack. A spark-resistant bulk-micromegas chamber for high-rate applications. *Nuclear Instruments and Methods in Physics Research, Section A: Accelerators, Spectrometers, Detectors and Associated Equipment*, 640(1):110–118, 2011. DOI:http://dx.doi.org/10.1016/j.nima.2011.03.025.

[28] Tai Hua Lin, Andreas Düdder, Matthias Schott, Chrysostomos Valderanis, Laura Wehner, and Robert Westenberger. Signal characteristics of a resistive-strip micromegas detector with an integrated two-dimensional readout. *Nuclear Instruments and Methods in Physics Research, Section A: Accelerators, Spectrometers, Detectors and Associated Equipment*, 767:281–288, 2014.

[29] M Byszewski and J Wotschack. Resistive-strips micromegas detectors with two-dimensional readout. *Journal of Instrumentation*, 7(02):C02060–C02060, 2012. DOI:http://stacks.iop.org/1748-0221/7/i=02/a=C02060?key=crossref.4e1bce2bd03b6691e6747e980186a780.

[30] Konstantinos Ntekas. *Performance characterization of the Micromegas detector for the New Small Wheel upgrade and Development and improvement of the Muon Spectrometer Detector Control System in the ATLAS experiment.* PhD thesis, Natl. Tech. U., Athens, 2016. DOI:http://inspirehep.net/record/1503893/files/CERN-THESIS-2016-019.pdf.

[31] M.J. French, L.L. Jones, Q. Morrissey, A. Neviani, R. Turchetta, J. Fulcher, G. Hall, E. Noah, M. Raymond, G. Cervelli, P. Moreira, and G. Marseguerra. Design and results from the apv25, a deep sub-micron {CMOS} front-end chip for the {CMS} tracker. *Nuclear Instruments and Methods in Physics Research Section A: Accelerators, Spectrometers, Detectors and Associated Equipment*, 466(2):359 – 365, 2001. 4th Int. Symp. on Development and Application of Semiconductor Tracking Detectors.

[32] S Martoiu, H Muller, A Tarazona, and J Toledo. Development of the scalable readout system for micro-pattern gas detectors and other applications. *Journal of Instrumentation*, 8(03):C03015, 2013. DOI:http://stacks.iop.org/1748-0221/8/i=03/a=C03015.

[33] R.K. Carnegie, M.S. Dixit, J. Dubeau, D. Karlen, J.-P. Martin, H. Mes, and K. Sachs. Resolution studies of cosmic-ray tracks in a {TPC} with {GEM} readout. *Nuclear Instruments and Methods in Physics Research Section A: Accelerators, Spectrometers, Detectors and Associated Equipment*, 538(1–3):372 – 383, 2005.

[34] Georgios Iakovidis. *Research and Development in Micromegas Detector for the ATLAS Upgrade.* PhD thesis, Natl. Tech. U., Athens, 2014-10-13. DOI:https://inspirehep.net/record/1339824/files/CERN-THESIS-2014-148.pdf, reportNumber = ”CERN-THESIS-2014-148”, SLACcitation = ”CERN-THESIS-2014-148;